

DISSERTATION

RYDBERG SPECTROSCOPY OF Fr-LIKE THORIUM AND URANIUM IONS

Submitted by

Mark Earl Hanni

Department of Physics

In partial fulfillment of the requirements

For the Degree of Doctor of Philosophy

Colorado State University

Fort Collins, Colorado

Fall 2010

Doctoral Committee:

Department Chair: John Harton

Advisor: Stephen R. Lundeen

R. Mark Bradley
Jacob L. Roberts
Azer P. Yalin

Copyright by Mark Hanni 2010

All Rights Reserved

ABSTRACT

RYDBERG SPECTROSCOPY OF Fr-LIKE THORIUM AND URANIUM IONS

The binding energies of high L Rydberg levels of Th^{3+} were measured using the resonant excitation Stark ionization spectroscopy (RESIS) technique. When analyzed using the long range polarization model the measured energies determine the dipole and quadrupole polarizability of the Th^{4+} ion: $\alpha_d = 7.61(6)$ a.u. and $\alpha_Q = 45(4)$ a.u. The RESIS technique and apparatus constructed for this study are discussed in this work. Modifications to the original design of the detector are presented. The modifications to the detector increased the energy resolution of the beams in the detector. It was determined that a significant source of background present in the observations of the U^{5+} Rydberg fine structure is due to the presence of auto-ionizing Rydberg states attached to metastable excited ion cores. These auto-ionizing states severely limit the fine structure observations, preventing the successful observation of any U^{5+} Rydberg fine structure. Also discussed are future directions that could lead to an increase in the signal to noise in the Th^{3+} fine structure observations and to a successful measurement of the dipole polarizability of U^{6+} .

Acknowledgements

First and foremost I would like to sincerely thank and acknowledge my advisor Steve Lundeen for his advice, support, and humor throughout my graduate career.

Without his guidance and patience with me this work would not have been possible. I would also like to thank Steve for his support of in his students' personal lives and advice in life beyond graduate school. I would also like to thank the support staff at the J. R. Macdonald Laboratory at Kansas State University. In particular, I would like to acknowledge the advice and friendship Charles Fehrenbach. His in-depth knowledge of a broad range of topics proved to be invaluable to my research and aided in the development of the modifications to the apparatus. Gregg Sturris is also deserving of thanks for his help during the early portion of my work and for the loan of the power supply used to accelerate the ion beams.

I would like to thank Julie Keele for her friendship and discussions about topics other than physics during the long hours of data acquisition and drives to and from KSU. I would also like to thank Tony Gorges for being one of my best friends in graduate school, with whom I could talk about nearly everything.

Turning to the more personal side of things; I would like to thank my parents and grandparents. Without their love, support, and constant reminder to finish everything I start I would not be the person I am today.

And finally, I would like to thank my wife Jessica for always being supportive of my goals and ambitions as well as tolerating the graduate student lifestyle.

Table of Contents

Chapter 1: Introduction	1
1.1 Motivation.....	1
1.2 Theoretical model	2
1.3 Overview of the RESIS technique	12
1.4 History and Direction.....	16
Chapter 2: Experimental Apparatus	21
2.1 Introduction and Overview of the apparatus.....	21
2.2 Ion beam generation and selection.....	23
2.3 Rydberg state population creation	37
2.4 Laser Interaction Region.....	49
2.5 RESIS detector.....	57
Chapter 3: Apparatus Evaluation Data.....	63
3.1 RESIS transition enhancement	64
3.2 Reduction of the Electric field in the LIR.....	75
3.3 Calibration of the stage angle	92
3.4 Detector modifications and sources of background.....	97
Chapter 4: Rydberg spectroscopy of Th IV	126
4.1 Th ³⁺ Rydberg Fine Structure observations	126
4.2 Dipole and Quadrupole Polarizabilities of Th ⁴⁺	136
4.3 Th ³⁺ Conclusions	146
Chapter 5: Rydberg Spectroscopy of U VI.....	149
5.1 Spectroscopy of High- <i>L</i> Rydberg states of U VI.....	149
5.2 Comparison of different beam configurations	155
5.3 Comparison of observations with CTMC predictions	159
5.4 CTMC predictions of Signal size compared to observations	162
5.5 Future directions	167
References	169

List of Tables

Table 2.1: Measurements of the Fluke hand-held high voltage probe at various dial settings.....	34
Table 2.2: Rb final state transition frequencies used in this work	40
Table 3.1: Measured ratios of the (37, 9) – (73, 10) transition in Th^{3+} to the high-L transition.....	74
Table 3.2: Compensator settings used to minimize the line widths of the $n = 20 - 83$ and $20 - 84$ transitions in Pb^+ and the $37 - 73$ and $38 - 79$ transitions in Th^{3+}	90
Table 3.3: Components of the electric field in the LIR	90
Table 3.4: Si^{2+} properties determined using the microwave RESIS technique and the long range polarization model.....	93
Table 3.5: Fitted centers of the resolved Si^+ fine structure transitions observed using the optical RESIS technique	94
Table 3.6: Calculated fine structure energies of Si^+ transitions.....	96
Table 3.7: θ_{\perp} determinations.....	97
Table 3.8: Comparison of estimated and actual horizontal deflection steering potentials	109
Table 3.9: Comparison of the DC to High-L ratio with excellent and not so excellent detector pressures	114
Table 3.10: Average estimated auto-ionization rates for U^{6+} and Th^{4+}	120
Table 3.11: Auto-ionization model comparison to observations	124
Table 3.12: Comparison of different predicted values for BG/CXRT and RP/CXRT after adjusting the Auto-ionization rate.....	124
Table 4.1: List of the transitions, CO_2 laser lines, and beam velocities used in the observation of the Th IV Rydberg fine structure	127

Table 4.2: Individual fit results for 37 – 76 transition in Th^{3+}	133
Table 4.3: Individual fit results for 37 – 73 transitions in Th^{3+}	133
Table 4.4: Individual fit results for 38 – 79 transitions in Th^{3+}	134
Table 4.5: Average fitted centers of Th^{3+} resolved fine structure transitions	134
Table 4.6: Average width of the resolved RESIS transitions	139
Table 4.7: Observed zero field Rydberg fine structure transition energies in Th^{3+}	141
Table 4.8: List of the small corrections applied to determine the $E^{(1)}$	141
Table 4.9: First order energies and matrix elements used in determining the polarizability of the Th^{4+} ion	142
Table 4.10: Theoretical estimates of β_d	144
Table 4.11: Summary of the dynamic properties of the Th^{4+} ion	148
Table 5.1: Summary of the various U^{5+} transitions studied.....	149
Table 5.2: Measured characteristics of the different U^{5+} and Th^{4+} transitions studied...	157
Table 5.3: Predictions of the $n_l, L = 11$ signal to noise	158
Table 5.4: Estimation of the time required, per point, to achieve similar signal to noise on the $n_l, L = 11$ signal that was achieved in the study of Th IV	159
Table 5.7: Measured count rates for the charge transfer beam and $n_l, L = 11$ signal.....	161
Table 5.8: Ratios of the observed count rates	162
Table 5.9: CTMC predicted capture cross sections for the different beam configurations studied	164
Table 5.10: CTMC predicted capture into $n_l, L = 9, 10, \text{ or } 11$, corrected for radiative decay	165
Table 5.11: Comparison of the observed ratio of $R_{S(L=11)}$ to R_{CXRT} to the same ratio predicted by CTMC.....	166

List of Figures

Figure 1.1: Estimated fine structure energies of Th^{3+} Rydberg states with $n = 37$	11
Figure 1.2: The four transition branches accessible to the CO_2 laser used.....	14
Figure 1.3: Typical scan of the 55 – 109 Rydberg fine structure of Kr VI.....	19
Figure 2.1: Schematic of the RESIS apparatus.....	22
Figure 2.2: ECR Plasma chamber.....	24
Figure 2.3: ECR sputter target	24
Figure 2.4: ECR ion source completely assembled	25
Figure 2.5: Quadrupole doublet lenses, extracted from the housings.....	27
Figure 2.6: Spectrum of ion beams produced by the ECR	29
Figure 2.7: Spectrum of the beams produced by the ECR.....	30
Figure 2.8: Calibration curve for the Glassman High Voltage supply	32
Figure 2.9: ^{85}Rb excitation scheme.....	39
Figure 2.10: Capture cross section as a function of n for various target states for 100 keV Th^{4+}	41
Figure 2.11: Schematic of the lower target region.....	43
Figure 2.12: Optical layout used to excite the thermal plume of Rb	44
Figure 2.13: CAD schematic cutaway of the Pre-ionizing and Re-mixing lens.....	46
Figure 2.14: SIMION simulation of the fields present in the Pre-ionizing and Re-mixer lens	48
Figure 2.15: Schematic of the Laser Interaction Region	52

Figure 2.16: Th^{3+} (37, 8) – (73, 9) resolved transition.....	54
Figure 2.17: CAD schematic of the original detector region.....	58
Figure 2.18: Detailed picture of the Stark Ionizer electrodes	59
Figure 2.19: Schematic of the potential and electric field in the Stark Ionizer	62
Figure 3.1: Graphical depiction of the $n = 4$, L Stark levels in Hydrogen.....	68
Figure 3.2: SIMION simulation of the longitudinal electric field through the center of the re-mixer	69
Figure 3.3: SIMION simulation of the transverse electric field in the re-mixer lens as a function of the radial distance	70
Figure 3.4: Calculated minimum electric field in the remixer as a function of the radial distance.....	71
Figure 3.5: Th^{3+} (37, 9) – (73, 10) transition	73
Figure 3.6: CAD drawings of the electrode rings of the electric field compensation device.	76
Figure 3.7: Completed electrode ring assembly of the compensator device	77
Figure 3.8: Graphical depiction of the arrangement of the axes of the compensator	78
Figure 3.9: Compensator control electrical circuit	79
Figure 3.10: Plot of the x, y, and z components of the electric field when ± 1 V is applied to the x-axis electrodes of the compensator	81
Figure 3.11: Plot of the x, y, and z components of the electric field when ± 1 V is applied to the y-axis electrodes of the compensator	82
Figure 3.12: Plot of the x, y, and z components of the electric field when ± 1 V is applied to the z-axis electrodes of the compensator	83
Figure 3.13: Plot of the x, y, and z components of the electric field when 1 V is applied to the mirror assembly inside the LIR.....	84
Figure 3.14: Comparison of the resolution of RESIS transitions in $20 - 83 \text{ Pb}^+$ with the compensator off (a) and then tuned to minimize the field (b).....	87

Figure 3.15: Comparison of the resolution of RESIS transitions in $20 - 84 \text{ Pb}^+$ with the compensator off (a) and then tuned to minimize the field (b).....	89
Figure 3.16: Plot of the electric field vectors determined from SIMION simulations of the LIR and compensator assembly	91
Figure 3.17: Observed Si^+ (a) $19 - 51$ and (b) $19 - 52$ fine structure transitions	95
Figure 3.18: Profile of 90 keV U^{5+} and U^{6+} beams entering the CEM in the RESIS detector	99
Figure 3.19: Noise level as a function of the CEM DC.....	102
Figure 3.20: Revised detector design.....	103
Figure 3.21: Profile of the 90 keV U^{6+} and U^{5+} beams entering the CEM after installation of the $\sim 8^\circ$ vertical tilt in the detector	104
Figure 3.22: Profile of the 150 keV U^{6+} and U^{5+} beams entering the detector using the new potential arrangement	105
Figure 3.23: Horizontal bend before the detector entrance aperture	107
Figure 3.24: Horizontal deflector assembly.....	108
Figure 3.25: Regenerated 150 keV U^{6+} and Stark ionized U^{6+} beam profiles in the detector with a 4° bend in the beam line just before the detector.....	110
Figure 3.26: Schematic diagrams of CEM DC profiles resulting from different sources of background.....	112
Figure 3.27: Estimated energy level diagram of U^{6+}	116
Figure 3.28: $6p^5 5f$ levels in U^{6+} and estimated auto-ionization lifetimes for Rydberg states with $n = 56$ and $L = 15$	118
Figure 3.29: Probability of contributing to the background as a function of the auto-ionization rate.....	121
Figure 3.30: Probability curve of an auto-ionizing Rydberg state contributing to the regenerated primary beam as a function of the auto-ionization rate	123
Figure 4.1: Observed $(37, 7) - (76, 8)$ transition in 100 keV Th^{3+}	128
Figure 4.2: RESIS excitation spectrum of the $n = 37 - n' = 73$ transition in 100 keV Th^{3+}	129

Figure 4.3: RESIS excitation spectrum of the 38 – 79 transition in 100 keV Th^{3+}	130
Figure 4.4: Example of the four parameter Gaussian fit to the (37, 8) – (73, 9) transition in Th^{3+}	132
Figure 4.5: Parametric study of the simulated width of the RESIS transitions as a function of stray electric field.....	140
Figure 4.6: Scaled polarizability plot for Th^{4+}	143
Figure 4.7: Scaled energy plot with various choices of L for the resolved transitions ..	145
Figure 5.1: RESIS excitation spectrum of U^{5+} 53 – 93 Rydberg fine structure using the 10F Rydberg target.....	151
Figure 5.2: RESIS excitation spectrum of 150 keV U^{5+} 53 – 93 Rydberg fine structure using the 8F Rydberg target	152
Figure 5.3: RESIS excitation spectrum of 93 keV U^{5+} 55 – 109 Rydberg fine structure using the 8F Rydberg target	153
Figure 5.4: CTMC predicted n_l distributions for the (a) U-A, (b) U-B, (c) U-C, and (d) Th-A configurations	163

Chapter 1: Introduction

1.1 Motivation

Improved understanding of the chemistry of actinide elements is important to many areas of high priority, such as the cleanup and proper handling of radioactive waste, nuclear power [1], and national defense. Research on the actinide elements provides the basic knowledge and understanding that can be used to develop new technologies and processes in dealing with these radioactive materials [1]. The chemistry of the actinide elements remains the subject of an ongoing research initiative of the Department of Energy [1]. The chemistry involves forming compounds with other elements (e.g. carbon, oxygen, and fluorine) that are quite well understood [2]. The Rn-like Th^{4+} and U^{6+} ions are the most common charge states that occur in many of the chemical compounds of these two actinide elements [2]. The theoretical models that are used for *a-priori* computation of the properties of the actinide compounds begin with the description of the properties of the free actinide ion. The most significant dynamic properties of the free actinide ion are the dipole and quadrupole polarizability. However, there are no first hand measurements of these properties and optical spectroscopy of the excited levels of these charge states is nonexistent [3]. Although theoretical models do exist to calculate these properties it is difficult to know how reliable the theoretical models are. The models are complicated because these systems are highly relativistic and even the isolated ions are difficult to describe theoretically with confidence.

It is the objective of this work to make the first determinations of the dipole and quadrupole polarizability of these highly charged Rn-like Th^{4+} and U^{6+} ions by studying the Rydberg fine structure patterns of the Th^{3+} and U^{5+} ions. Hopefully the experimentally determined values of these dynamic properties can be applied as benchmarks to test the existing theoretical models describing the free actinide ion.

This chapter will present an introduction to the theoretical model and the experimental technique used to observe the high- L Rydberg states of highly charged actinide ions. Chapter 2 is a detailed description of the experimental apparatus. Chapter 3 discusses data regarding the critical aspects of the apparatus performance. Chapter 4 presents the Rydberg spectroscopy of Th^{3+} leading to determination of the dipole and quadrupole polarizability of Th^{4+} . Chapter 5 describes the experimental observations of the U^{5+} Rydberg fine structure and corresponding difficulties in extracting the dipole polarizability for U^{6+} from the observations.

1.2 Theoretical model

The long range interaction between a Rydberg electron and the positively charged core ion result in a breakdown of the degeneracy of the hydrogenic energy levels. The resulting fine structure energies can be described by what is called the “long range polarization model”. In order to carry out the derivation of the long range polarization model and examine how the long range interactions break the L degeneracy of the Rydberg states, two simplifying assumptions about the Rydberg electron are made. These assumptions are:

- (1) The Rydberg electron is distinguishable from all other electrons of the positive ion core

and

(2) The Rydberg electron does not penetrate the space of the ion core.

The centrifugal barrier prevents the Rydberg electron from penetrating the space of the positive ion core. The inner turning point of the radial coordinate of the Rydberg electron can be obtained from examination of the radial portion of the Schrödinger equation for a hydrogenic system. The radial portion of the Schrödinger equation for an electron orbiting a small charge $+Q$, in atomic units, is

$$\frac{d^2 P_{n,L}(r)}{dr^2} + \left[2E(n,L) + \frac{Q}{r} - \frac{L(L+1)}{2r^2} \right] P_{n,L}(r) = 0. \quad (1.1)$$

where $P_{n,L}(r) = R_{n,L}(r) \cdot r$. The potential that the electron experiences is

$V(r) = \frac{-Q}{r} + \frac{L(L+1)}{2r^2}$. The inner turning point of the radial motion of the electron is

determined when

$$E(n,L) = \frac{-Q^2}{2n^2} = \frac{-Q}{r} + \frac{L(L+1)}{2r^2}. \quad (1.2)$$

The classical inner turning point of the electron orbit, r_- , is found directly from Eq. (1.2)

by solving for r :

$$r_- = \left[\frac{n^2}{Q} - \frac{n^2}{Q} \sqrt{1 - \frac{L(L+1)}{n^2}} \right] a_0 \cong \left\{ \frac{n^2}{Q} - \frac{n^2}{Q} \left[1 - \frac{L(L+1)}{2n^2} + \dots \right] \right\} a_0, \quad (1.3)$$

when $L^2 \ll n^2$. The classical inner turning point of the orbit of the Rydberg electron

when $L^2 \ll n^2$ is then

$$r_- \geq \frac{L(L+1)}{2Q} a_0. \quad (1.4)$$

The ions studied in this work have electrons in states with $L \geq 7$. The inner turning point for the motion of the Rydberg states of Th^{3+} studied, where $Q = 4$, is $r_- \geq 7.0a_0$. For the

Rydberg states of U^{5+} , where $Q = 6$ in Eq. (1.4), the inner turning point is $r. \geq 4.7a_0$. The atomic radius for Thorium is $3.4a_0$ [4], the atomic radius of Th^{4+} will be smaller. The atomic radius for Uranium is $2.6a_0$ [5], the atomic radius will be smaller for U^{6+} . Thus, the assumption that the Rydberg electron does not penetrate the ion core is valid, even for the lowest L states studied in this work.

The long range polarization model which describes the resulting fine structure pattern for non-penetrating high L Rydberg states for ions with S-state cores has been used for many years [6]. This model has been given a firm theoretical background by Drachman [7]. Recently, this model has been used to describe the observed Rydberg fine structure pattern of highly charged ions [8].

The long range polarization model for highly charged ions can be derived following the formalisms developed by Drachman [7] to describe He Rydberg states. Starting with the non-relativistic Hamiltonian for the full system, ignoring spin, the Hamiltonian for the full system is given by

$$\begin{aligned}
 H &= \left[\sum_{i=1}^{N-1} \left(\frac{|\vec{p}_i|^2}{2m} - \frac{Z}{r_i} \right) + \sum_{i>j}^{N-1} \frac{1}{r_{ij}} \right] + \left[\frac{|\vec{p}_N|^2}{2m} - \frac{Q}{r_N} \right] + \left[\sum_{i=1}^{N-1} \frac{1}{r_{iN}} - \frac{(N-1)}{r_N} \right]. \quad (1.5) \\
 &= H_{Core} + H_{Ryd}^0 + V
 \end{aligned}$$

where Z is the total nuclear charge, N is the total number of electrons (including the Rydberg electron), r_i is the radial coordinate of the i^{th} core electron, r_N is the radial coordinate of the Rydberg electron, and $Q = Z - N + 1$ is the net charge of the ion core. In this model the Rydberg electron, the N^{th} electron, is considered to be distinguishable from the other electrons surrounding the ion core. The first two terms describe the energy of the ion core and the hydrogenic Rydberg electron. The last grouped term, V , is

the small perturbation of the Rydberg electron energy due to the interactions with the ion core in addition to the fully screened Coulomb interaction contained in H_{Ryd}^0 .

If V is neglected above, then the Hamiltonian reduces to a sum of two terms. Thus the zeroth order wavefunction for the system is

$$\Psi^0 = \Psi_{Core}^0 \otimes \Psi_{Ryd}^0, \quad (1.6)$$

and the zeroth order energy is

$$E^{[0]} = E_{Core}(\lambda, J_c) - \frac{Q^2}{2n^2}, \quad (1.7)$$

where λ is a quantum number describing core state and J_c is the total angular momentum of the core. The zeroth order energy and the energies that follow are expressed in atomic units.

The small perturbation V in Eq. (1.5) can be expressed in a more convenient form as

$$V = \sum_{i=1}^{N-1} \frac{1}{r_{iN}} - \frac{(N-1)}{r_N} = \sum_{\kappa=1}^{\infty} \sum_{i=1}^{N-1} \left(\frac{r_i^{\kappa}}{r_N^{\kappa+1}} \right) C^{[\kappa]}(\Omega_i) \bullet C^{[\kappa]}(\Omega_N), \quad (1.8)$$

using the multipole expansion. In the above expansion of V : Ω_i is the angular coordinates of the i^{th} core electron, Ω_N is the angular coordinates of the Rydberg electron, and $C^{[\kappa]}$ is a spherical tensor of rank κ [9]. The monopole term is absent in the expansion of V in Eq. (1.5) because of assumption 2) above.

The effects of V on the energy of the Rydberg electron in a given (n, L) state can be examined in more detail by applying Rayleigh-Schrödinger perturbation theory. Using perturbation theory the energy for the full system can then be expressed as the sum of the terms in the perturbation expansion:

$$\begin{aligned}
E &= E^{[0]} + E^{[1]} + E^{[2]} + \dots \\
E^{[1]} &= \langle \Psi^0 | V | \Psi^0 \rangle \\
E^{[2]} &= \sum_{\Psi'^0 \neq \Psi^0} \frac{|\langle \Psi^0 | V | \Psi'^0 \rangle|^2}{E(\Psi^0) - E(\Psi'^0)} \cdot \\
&\vdots
\end{aligned} \tag{1.9}$$

The terms in the perturbation expansion higher than $E^{[2]}$ are ignored in this work because their effects were found to be negligible.

The first order energy, $E^{[1]}$, is zero for ions with S-state ground states because the integral over the core electrons' angular coordinates vanishes. The evaluation of $E^{[2]}$ is complicated by the inclusion of the energy denominator. The energy denominator can be expressed as a sum of the energy of the ion core and the Rydberg electron, allowing the second order energy contribution to be re-written as

$$E^{[2]} = - \sum_{\Psi'^0 \neq \Psi^0} \frac{|\langle \Psi^0 | V | \Psi'^0 \rangle|^2}{\Delta E_{Core} + \Delta E_{Ryd}}, \tag{1.10}$$

where $\Delta E_{Core} = E(\lambda_c, J'_c) - E(g, J_c)$ and $\Delta E_{Ryd} = E(n', L') - E(n, L)$. In Eq. (1.10) $E(g, J_c)$ is the ground state energy of the positively charged ion core and $E(\lambda_c, J'_c)$ is the energy of an excited state of the positive ion core. The evaluation of $E^{[2]}$ can then be carried out by applying one further simplifying assumption that $\Delta E_{Ryd} \ll \Delta E_{Core}$. For the ions studied in this work, Th^{4+} and U^{6+} , the energy difference between the ground state of the core and the nearest excited state is estimated to be ~ 20 eV [10]. The energy difference between the different Rydberg states studied is typically on the order of ~ 0.1 eV. In the limit that $\Delta E_{Ryd} \ll \Delta E_{Core}$ the energy denominator can be expanded in a power series in what is known as the ‘‘adiabatic expansion’’ as

$$\frac{1}{\Delta E_{Core} + \Delta E_{Ryd}} \approx \frac{1}{\Delta E_{Core}} - \frac{\Delta E_{Ryd}}{(\Delta E_{Core})^2} + \dots \quad (1.11)$$

$E^{[2]}$ can be written now using the expansion above as

$$\begin{aligned} E^{[2]} &\approx - \sum_{\Psi'^0 \neq \Psi^0} \frac{|\langle \Psi^0 | V | \Psi'^0 \rangle|^2}{\Delta E_{Core}} + \sum_{\Psi'^0 \neq \Psi^0} \frac{|\langle \Psi^0 | V | \Psi'^0 \rangle|^2}{(\Delta E_{Core})^2} \Delta E_{Ryd} + \dots \\ &\approx E_{Ad}^{[2]} + E_{NAAd}^{[2]} + \dots \end{aligned} \quad (1.12)$$

The first term in the expression above gives rise to energy contributions from the adiabatic dipole and quadrupole polarizability of the ion core and the second term in the expression above gives rise to the first in a series of non-adiabatic corrections to the dipole and quadrupole polarizability of the ion core. The evaluation of $E_{Ad}^{[2]}$ and $E_{NAAd}^{[2]}$ becomes straight forward at this point. In this work only terms proportional to the adiabatic dipole and quadrupole polarizability and the first non-adiabatic correction to the dipole polarizability were found to significantly contribute to the energy deviations from hydrogenic of the Rydberg fine structure levels. The derivation of these terms is carried out explicitly here and all higher order terms are neglected, amounting to evaluating Eq. (1.12) with $\kappa=1$ and 2 for $E_{Ad}^{[2]}$ and only $\kappa=1$ for $E_{NAAd}^{[2]}$ in the multipole expansion for V given by Eq. (1.6). The resulting approximate expressions for the energy contributions to $E^{[2]}$ are:

$$E_{Ad}^{[2]} \approx - \sum_{\Psi'^0 \neq \Psi^0} \frac{\left| \langle \Psi^0 | \vec{D} \cdot \frac{C^{[1]}(\Omega_N)}{r_N^2} | \Psi'^0 \rangle \right|^2}{\Delta E_{Core}} - \sum_{\Psi'^0 \neq \Psi^0} \frac{\left| \langle \Psi^0 | \vec{Q} \cdot \frac{C^{[2]}(\Omega_N)}{r_N^3} | \Psi'^0 \rangle \right|^2}{\Delta E_{Core}} \quad (1.13)$$

$$E_{NAAd}^{[2]} \approx \sum_{\Psi' \neq \Psi} \frac{\left| \langle \Psi | \vec{D} \cdot \frac{C^{[1]}(\Omega_{Ryd})}{r_{Ryd}^2} | \Psi' \rangle \right|^2}{(\Delta E_{Core})^2} \Delta E_{Ryd} \quad (1.14)$$

The dipole and quadrupole operators are defined in this work as:

$$\begin{aligned}\bar{D} &= \sum_{i=1}^{N-1} r_i C^{[1]}(\Omega_i) \\ \bar{Q} &= \sum_{i=1}^{N-1} r_i^2 C^{[2]}(\Omega_i)\end{aligned}\quad (1.15)$$

The energy contributions to $E^{[2]}$ from Eq. (1.13) and (1.14) can be evaluated using methods described in Edmonds [9]. The following discussion will be limited to the special case when $J_c = 0$, appropriate for describing the Th^{4+} and U^{6+} ions studied in this work. The first term in Eq. (1.13) can be expanded using Eq. (7.1.6) in Edmonds [9] as

$$E_{Ad, \kappa=1}^{[2]} = \sum_{\lambda_c, J'_c, n', L'} \left\{ \begin{matrix} L & L & 0 \\ 1 & 1 & L' \end{matrix} \right\}^2 \frac{\left| \langle g, J_c = 0 \| \bar{D} \| \lambda_c, J'_c = 1 \rangle \right|^2 \left| \langle n, L \| \frac{C^{[1]}(\Omega_N)}{r_N^2} \| n', L' \rangle \right|^2}{\Delta E_{Core}}. \quad (1.16)$$

The subscript c has been applied to the quantum numbers describing the free ion core state and subscripts are omitted to the quantum numbers describing the Rydberg electron. The sum over all L' vanishes except for when $L' = L \pm 1$ and the 6-J symbol in Eq. (1.16) can be readily evaluated and leaving

$$E_{Ad, \kappa=1}^{[2]} = \sum_{\lambda, n', L'} \frac{(2L'+1)}{3} \begin{pmatrix} L' & 1 & L \\ 0 & 0 & 0 \end{pmatrix} \left| \langle g, J_c \| \bar{D} \| \lambda_c, J'_c \rangle \right|^2 \left| \langle n, L \| r_N^{-2} \| n', L' \rangle \right|^2. \quad (1.17)$$

Because of the completeness of the Rydberg radial wavefunctions, for a fixed L' the sum over all possible n' is reduced to a simple expectation value:

$$\sum_{n'} \left| \langle n, L \| r_N^{-2} \| n', L' \rangle \right|^2 = \langle r^{-4} \rangle_{n, L}. \quad (1.19)$$

Defining the dipole polarizability of the ion core in terms of the dipole operator as

$$\alpha_d = \frac{2}{3} \sum_{\lambda_c} \frac{|\langle g, J_c = 0 | \bar{D} | \lambda_c, J_1 = 1 \rangle|^2}{\Delta E_{Core}}, \quad (1.20)$$

and carrying out the sum over L' , Eq. (1.16) can be rewritten as

$$E_{Ad, \kappa=1}^{[2]} = \frac{-\alpha_d}{2} \langle r^{-4} \rangle_{nL} \quad (1.21)$$

The remaining term in Eq. (1.13) can be simplified using similar methods. Simplifying

Eq. (1.14) requires the additional identity:

$$\sum_n |\langle n, L | r^{-2} | n', L' \rangle|^2 (E(n') - E(n)) = \frac{1}{2} (4 - L(L+1) + L'(L'+1)) \langle r^{-6} \rangle_{nL} \quad [11]. \quad (1.22)$$

The resulting energy contributions are given as

$$\begin{aligned} E_{Ad}^{[2]} &= -\frac{\alpha_d}{2} \langle r^{-4} \rangle_{nL} - \frac{\alpha_Q}{2} \langle r^{-6} \rangle_{nL} \\ E_{NAAd}^{[2]} &= 3\beta_d \langle r^{-6} \rangle_{nL} \end{aligned} \quad (1.23)$$

where the quadrupole polarizability of the ion core, α_Q , and first non-adiabatic

contribution to the dipole polarizability of the ion core, β_d , are defined as

$$\alpha_Q = \frac{2}{5} \sum_{\lambda_c} \frac{|\langle g, J_c = 0 | \bar{Q} | \lambda_c, J_c = 2 \rangle|^2}{\Delta E_{Core}} \quad \beta_d = \frac{1}{3} \sum_{\lambda_c} \frac{|\langle g, J_c = 0 | \bar{D} | \lambda_c, J_c = 1 \rangle|^2}{(\Delta E_{Core})^2}. \quad (1.24)$$

The radial expectation values of the Rydberg electron in Eq. (1.23) are taken to be the hydrogenic radial expectation values corrected for the finite mass of the an ion core with charge Q ; the subscript N has been dropped for clarity.

Returning to the expansion in Eq. (1.9), the energy for the full system, up to terms proportional to $\langle r^{-6} \rangle_{nL}$ in V , is approximately:

$$E(\lambda_c, J_c, n, L) \approx E(\lambda_c, J_c) - \frac{Q^2}{2(1 + \frac{m}{M})n^2} - \frac{\alpha_d}{2} \langle r^{-4} \rangle_{nL} - \frac{(\alpha_Q - 6\beta_d)}{2} \langle r^{-6} \rangle_{nL} + \dots \quad (1.25)$$

where

$$\langle r^{-4} \rangle_{nL} = \left(\frac{Q}{1 + \frac{m}{M}} \right)^4 \frac{3n^2 - L(L+1)}{2n^5 (L-0.5)L(L+0.5)(L+1)(L+1.5)}, \quad (L > 0) \quad [12] \quad (1.26)$$

and

$$\langle r^{-6} \rangle_{nL} = \left(\frac{Q}{1 + \frac{m}{M}} \right)^6 \frac{35n^4 - 5n^2 [6L(L+1) - 5] + 3(L-1)L(L+1)(L+2)}{8n^7 (L-1.5)(L-1)(L-0.5)L(L+0.5)(L+1)(L+1.5)(L+2)(L+2.5)}, \quad (L > 1) \quad [12]. \quad (1.27)$$

In Eqs. (1.25), (1.26), and (1.27) m is the mass of the electron and M is the mass of the positive ion core. In principle, higher order terms can be computed in the long range polarization model following a similar procedure, but the additional terms are proportional to higher inverse powers of r_N . The small deviations in the energy of the Rydberg electron due to the long range interactions in Eq. (1.24) can be summarized into an expectation value of an effective potential of the form

$$V_{eff} = \frac{\alpha_d}{2r^4} + \frac{(\alpha_Q - 6\beta_d)}{2r^6} + \dots \quad (1.28)$$

The ion core is assumed to be in the ground state for the Rydberg levels of the studied in this work and as a result $E_{Core}(g, J_c = 0)$ is defined to be zero. Dropping $E(\lambda_c, J_c)$ from Eq. (1.25) results in an approximate expression for the energy of a Rydberg election in a state with a given (n, L) . Figure 1.1 below is an example of the expected energy deviations from hydrogenic between the $n = 37$ Rydberg fine structure transitions in Th^{3+} assuming $\alpha_d = 7.75$ a.u. and $\alpha_Q = \beta_d = 0$.

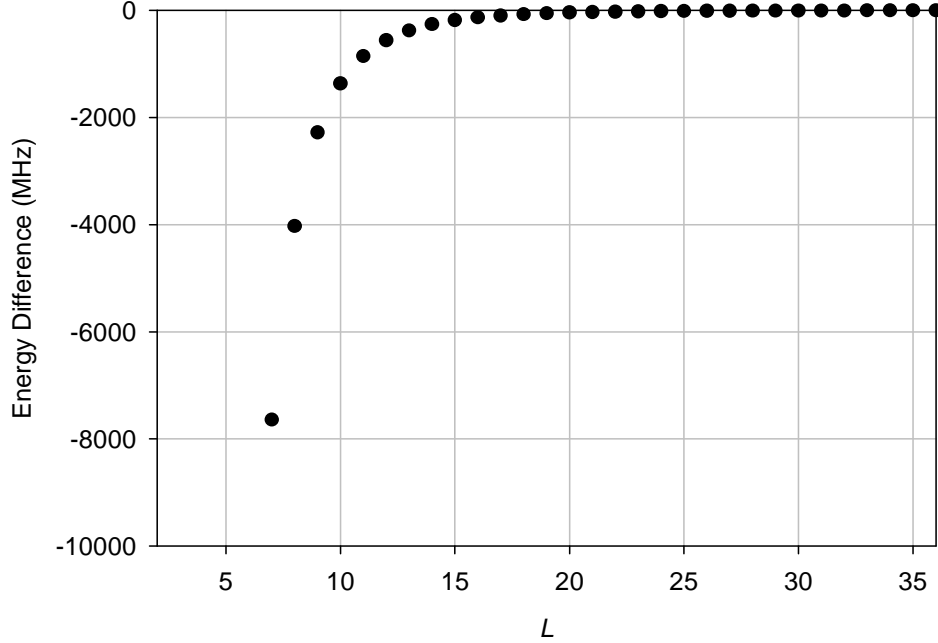


Figure 1.1: Estimated fine structure energies of Th^{3+} Rydberg states with $n = 37$ demonstrating the effects of the long range interaction of the positive ion core with the Rydberg electron on the energy of the Rydberg states. The parameters $\alpha_d = 7.75$ a.u. and $\alpha_Q = \beta_d = 0$ control the scale of these energies with respect to the hydrogenic energy of the $n = 37$ level. The y-axis of the plot is the energy deviation from the hydrogenic $n = 37$ energy (approximately -0.16 eV) of Th^{3+} in MHz. The x-axis is the L value of the level. It is expected that at very high values of L the resulting deviation from the hydrogenic energy is very small as the radial matrix elements with increasing L become smaller. At very low L the deviation from hydrogenic becomes very large and the terms proportional to higher inverse powers of r greater than 4 become increasingly important.

The derivation of Eq. (1.25) neglects two additional small contributions to the energy of a Rydberg level. The first is relativistic contributions arising from the “ p^4 ” contributions to the kinetic energy of the electron. These contributions are given by

$$E^{\text{Rel}}(n, L) = \frac{\alpha^2 Z^4}{2n^4} \left(\frac{3}{4} - \frac{n}{L + \frac{1}{2}} \right). \quad (1.29)$$

The second is contributions arising from the application of V_{eff} in second order. This energy describes the mixing of different Rydberg series and the resulting contribution is referred to as the second order energy and is denoted as $E^{[2]}$ throughout this work. The

value of $E^{[2]}$ is computed in this work using the analytical formula developed by Drake and Swainson [13]. The analytical formula, if only the leading terms proportional to $(\alpha_d)^2$ are included, is given below in Eq. (1.27), which is reproduced for reference from Ref. [13].

$$\begin{aligned}
E^{[2]}(Q, n, L) = & -2Q^6 \alpha_d^2 \left(\frac{(2L-3)!!}{(2L+3)!!} \right)^2 \left\{ \frac{(2L-5)!!}{(2L+5)!!} \frac{1}{n^7} \left[\left(\frac{9n^4}{[L(L+1)]^3} - \frac{6n^2}{[L(L+1)]^2} \right) \right. \right. \\
& \times \{45 + 7[89f_1(L) + 520f_2(L) + 80f_3(L)]\} \\
& \left. \left. + \{3 + 40[f_1(L) + 6f_2(L)]\} \right] \right. \\
& \left. + \frac{1}{n^8} \left(\frac{27n^4}{[L(L+1)]^2} - \frac{30n^2}{L(L+1)} + 7 \right) \right\} \\
f_1(L) = & L(L+1) \\
f_2(L) = & (L-1)L(L+1)(L+2) \\
f_3(L) = & (L-2)(L-1)L(L+1)(L+2)(L+3)
\end{aligned} \tag{1.30}$$

1.3 Overview of the RESIS technique

The Resonant Excitation Stark Ionization Spectroscopy technique has been used to observe the high- L fine structure patterns of many Rydberg atoms and ions including multiply charged ions such as Kr^{6+} [8] and Si^{2+} [14]. The technique begins by first creating a monochromatic beam of ions. These ions will play the role of the core ions in the Rydberg system. These ions should have a velocity $v/c \sim 0.001$ to allow sufficient Doppler tuning of the CO_2 laser. The ion beam then intersects with a Rydberg target. The Rydberg target is formed by a thermal plume of Rb atoms excited to a higher nF state from the ground state using three CW lasers. Approximately 1% of the ions in the

fast ion beam capture a highly excited electron from the Rydberg target forming a beam of Rydberg states in a small range of energies bound by approximately 0.1 eV.

The Rydberg ion beam then passes through a region of intense electric field to “pre-ionize” any extremely weakly bound Rydberg states. The Rydberg ion beam then passes into a laser interaction region where a CO₂ laser resonantly excites a specific transition between a Rydberg state with a given n to a much higher Rydberg that whose population was previously pre-ionized. The frequency of the CO₂ laser as viewed from the rest frame of the ion can be Doppler-tuned approximately $\pm 0.5 \text{ cm}^{-1}$ by varying the intersection angle of the laser with the fast Rydberg ion beam. The CO₂ laser is used because the large number of selectable lasing frequencies that can be chosen to closely correspond with any number of hydrogenic transition frequencies, as depicted in Fig. 1.2. From Fig. 1.2 it can be seen that there exist CO₂ frequencies that correspond closely with only one hydrogenic transition, making the identification of the transition straight forward. CO₂ frequencies that could potentially correspond with more than one hydrogenic transition frequency are not used to prevent confusion in identifying the spectral features.

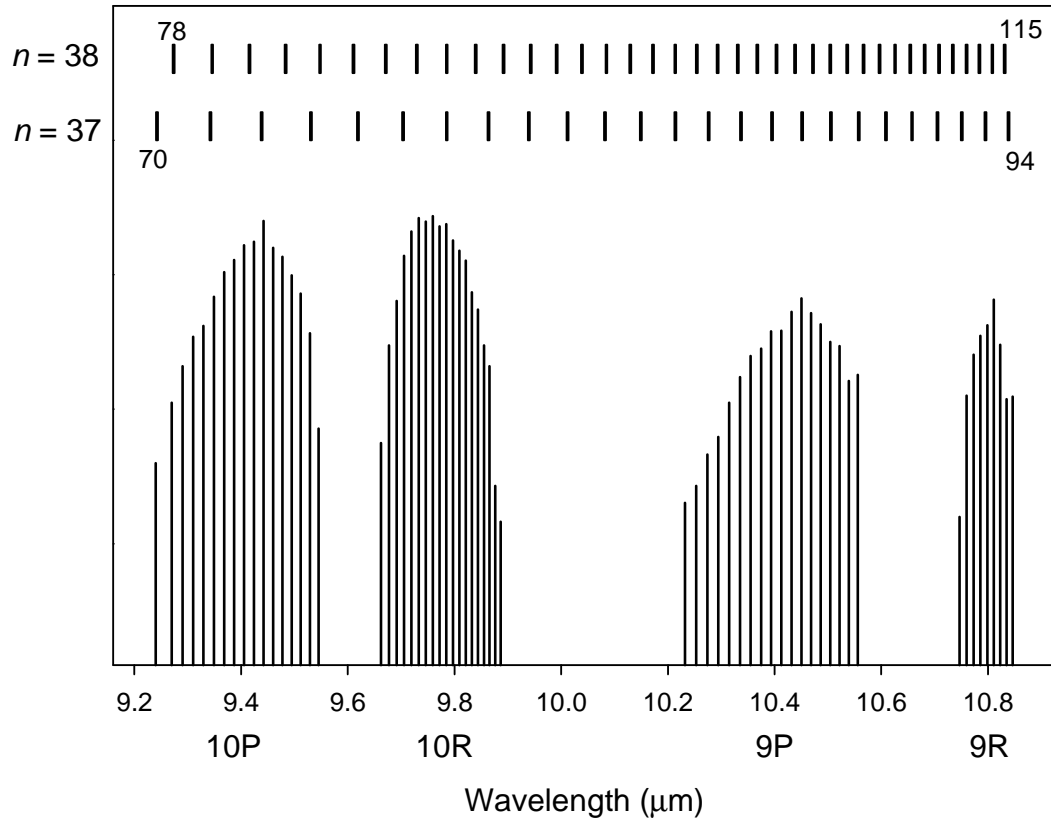


Figure 1.2: The four transition branches accessible to the CO₂ laser used. The amplitudes of the lines correspond with the output power of the laser. Along the top are lines corresponding to the frequency of transitions between the $n = 37$ and 38 to much higher n' Rydberg levels of the Th⁴⁺ ion. As the n of the upper state increases the density of transitions that correspond with a given CO₂ laser frequency increases. CO₂ laser lines corresponding with multiple transitions are not used to avoid confusion.

The Rydberg ion beam then enters into a Stark ionization region. The electric field in this region is adjusted to ionize the states that were resonantly excited using the CO₂ laser. When these ions are Stark ionized they experience a change in their kinetic energy that is proportional to the potential at the point of ionization. The change in the kinetic energy of the ions formed by Stark ionization "energy tags" the ions formed in the Stark ionizer region. The beams are then deflected into a channel electron multiplier (CEM) where the current synchronous with the chopping of the CO₂ laser is monitored with a lock-in amplifier. The vertical deflection separates the ions in the beam by charge and

energy. The energy tagging results in a separation of the ions formed in the Stark ionizer from the background ions of similar charge that are formed by other processes.

The RESIS technique is ideally a background free technique. Possible background is eliminated by pre-ionization of the weakly bound Rydberg states formed in charge transfer that could ionize in the Stark ionizer even when nothing is excited by the CO₂ laser. Energy tagging separates the Stark ionized Rydberg ions from any ions of the same charge resulting from other processes.

Experimental studies of the charge capture into Rydberg states by multiply charged ions indicate that the average binding energy of the captured electrons is given approximately by

$$E_p \approx \sqrt{Q} E_T, \quad (1.31)$$

where E_p is the binding energy of the final state after capture, Q is the ion charge, and E_T is the target binding energy [15]. The range of final state binding energies is approximately

$$\Delta E_p \approx 1.5 \text{ eV} \cdot v, \quad (1.32)$$

independent of Q , where v is the ion velocity in atomic units (1 a.u. = αc) [15]. For a given flux of ions that capture a Rydberg electron the signal size from a single (n, L) level is proportional to $f(n)/n$, where n is the lower state of the Rydberg transition being studied as well as the number of L values in the n state and $f(n)$ is the fraction of capture from the Rydberg target that results in population in the n state. As the charge of the ion, Q , increases the spacing between adjacent n levels at a fixed energy E_p decreases like $1/n$, implying that $f(n) \propto 1/n$. When the charge of the ion increases n increases

proportionally to Q , thus $f(n)/n \propto 1/Q^2$. When $Q = 6$ then the resolved signals will be 36 times smaller than the analogous signals for $Q = 1$. Since the RESIS technique is ideally background free the reduction by a factor of ~ 36 in the resolved signal size should not be a limiting factor in observing the resolved fine structure of the U^{6+} and Th^{4+} ions.

1.4 History and Direction

To put the goals of the research presented in this work into perspective, a brief overview of the historical developments of the RESIS technique leading to this study is useful. The work using the RESIS technique began around 1983 with Stephen Palfrey's investigation of Rydberg levels in He [16]. In his work he was able to successfully excite transitions between the G-H, H-I, and I-K levels in $n = 10$ He using microwave spectroscopy and the RESIS technique. In his experiment he started with a beam of He^+ ions that were created using a commercially available duo-plasmatron ion source [16]. The Rydberg states were formed by collisional neutralization of the He^+ beam with a gas charge exchange cell. This type of Rydberg state creation is useful for creating a large population of Rydberg states. However, only a small fraction of Rydberg states are formed in any particular desired state. The resonant excitation with a CO_2 laser and detection of very high n Rydberg levels used in this work are exactly the same as the methods developed in Palfrey's work.

Work was continued on the development of a method to produce Rydberg states in a more tightly controlled range of states. The production of Rydberg states by resonant charge exchange between a fast ion beam and an excited plume of Rb atoms was developed by E. A. Hessels and F. J. Deck [17]. In Deck's work a three laser excitation

scheme to excite a thermal plume of Rb atoms from the 5S ground state to the 8F or 10F excited state was developed. The Rb based Rydberg target has the advantage that the product Rydberg states are formed at roughly the same binding energy as the target level. A 10F Rb Rydberg target will produce a majority of Rydberg states in the $n \sim 10$ level of a singly charged ion. The Rb based Rydberg target was found to produce a much higher Rydberg state flux than the gas charge exchange cell [17] increasing the range of possible studies.

In early 2000 Daniel Fisher mapped out the effects of the resonant charge exchange from a Rb Rydberg target on multiply charged ion beams with different target states, using the RESIS technique to selectively detect individual product states [15]. Fisher's work also saw further development in the Rb excitation scheme using a tunable Ti:Sapphire laser to excite the final transition from the 4D excited state in Rb to an arbitrary nF level. Fisher's work documented the distribution of Rydberg states formed by capture in the Rydberg target by ions of charge Q and velocity v . The results showed fair agreement with calculations made with Classical Trajectory Monte Carlo methods (CTMC). This work made it clear that the RESIS technique would allow for the exploration of the fine structures of multiply charged ions [15]. However, the low beam intensities produced by the CryEBIS ion source at the J. R. Macdonald laboratory for Atomic Physics made these studies difficult and resolved fine structure transitions were unobservable in Fisher's study.

In preparation for this work to investigate the properties of highly charged actinide ions, an intermediate step of studying the fine structure energies of Kr^{5+} Rydberg states was conducted [8]. The ion source used in this study was a 5 GHz electromagnet ECR.

The ECR ion source produced more intense beams of Kr^{6+} ions than the CryEBIS. These beams were intense enough to allow for the observation of the transitions between different Rydberg levels, as shown in Fig. 1.3. However, this ECR was incapable of sputtering solid materials due to the lack of a sputter cathode. The study of the Kr^{5+} Rydberg levels showed that the RESIS technique and long range polarization model could be applied to successfully observe and describe the resulting fine structure energies of ions with $Q \leq 6$. This work paved the way for the purchase of a permanent magnet 14 GHz ECR ion source with a sputter cathode. This ECR can produce beams of highly ionized actinides with significant intensities.

In the Kr^{6+} study there was a large background present. It was believed that this large background was the result of incomplete separation of the primary Kr^{6+} ions that did not capture an electron in the Rydberg target from the Kr^{6+} signal ions, ions formed by Stark ionization of Rydberg Kr^{5+} . For a typical scan, illustrated in Fig. 1.3, the CEM DC value was 13.2 mV and the high- L signal amplitude was ~ 3.3 mV. This gives a high- L signal to background ratio of ~ 4 . The Kr^{6+} study suggested that preventing the primary beam from entering the detector would reduce the background and increase the signal to noise. Also, there was a large stray electric field on the order of 100 mV/cm [8] present for the Kr^{6+} study that complicated the lineshapes.

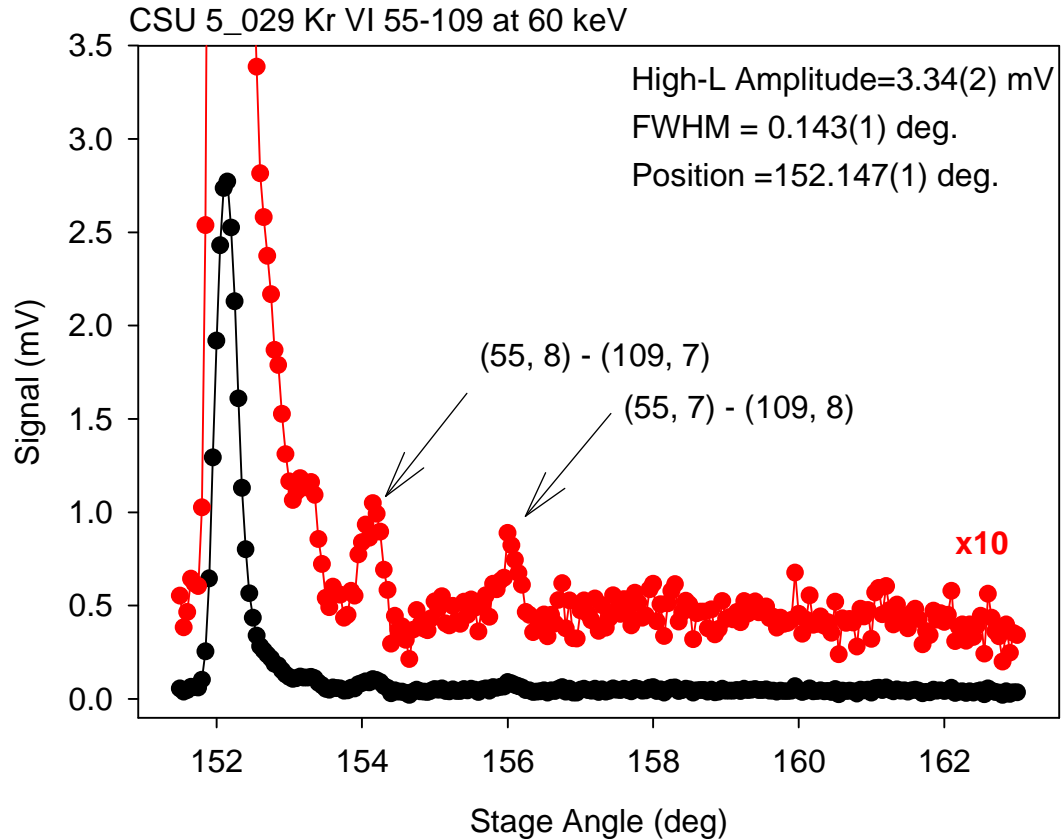


Figure 1.3: Typical scan of the 55 – 109 Rydberg fine structure of Kr VI. The transitions are identified from Ref. [8].

The problems in the Kr^{6+} study suggest that an improvement to the apparatus could be made by including a charge analyzing magnet just after the Rydberg target. Since the primary source of the background was believed to be due the overlap of the large residual Kr^{6+} primary ion beam with the Kr^{6+} signal ions formed by Stark ionization in the detector; separation of the Kr^{6+} primary ion beam from the Kr^{5+} ion beam would completely eliminate any potential overlap of the primary ion beam with the signal ions formed in the Stark ionizer. In addition, the inclusion of this additional bending magnet would reduce the amount of charged beam propagating through the apparatus, possibly leading to a reduction of the stray electric field. Reducing the stray electric field would lead to a reduction in the line width of the resolved transitions between specific high

angular momentum states and a reduction of the complications arising in the analysis of the resulting Rydberg fine structure pattern due to Stark shifting of the levels from their zero field positions.

Nearly 20 years of research and development of the RESIS technique and experimental apparatus culminate in this work where the properties of the common charge states of Th and U that occur in heavy element chemistry are investigated. One of the objectives of the research presented in this work was to construct a new apparatus that included the new ECR and a few additional improvements to the overall design of the apparatus to reduce background. Chiefly among these improvements was the introduction of an additional 15° charge selection magnet after the Rydberg target. The final objective of this work was to test the new apparatus by investigating the fine structures of Th^{4+} and U^{6+} actinide ions.

Chapter 2: Experimental Apparatus

2.1 Introduction and Overview of the apparatus

Description of the apparatus used in this research is broken up in this chapter into four sections corresponding roughly with four broad functions of the apparatus. Photographs of the apparatus used in this experiment are shown in Fig. 2.1 along side a schematic of the apparatus boxes highlighting the component sections as they will be grouped for discussion in the sections that follow. The first section of the apparatus deals with the creation and the selection of the ion beam. The components encompassed in this first hardware block are the ECR ion source, the two quadrupole doublet electrostatic lenses and the 20° bending magnet used for charge and mass selection. The second section of the apparatus deals with the creation Rydberg states via charge capture from the Rydberg target, the isolation of the beam of ions that have captured an electron from the target into a Rydberg state using a 15° bending magnet, and the manipulation of the populations of the Rydberg states using two einzel lenses, the pre-ionizing and re-mixing lenses, that were constructed for this research. The third section consists of the CO₂ Laser Interaction Region (LIR) used for resonant excitation of the Rydberg states into very high Rydberg states. Finally, the fourth section of the apparatus deals with the detection of the highly excited Rydberg states via selective Stark ionization.

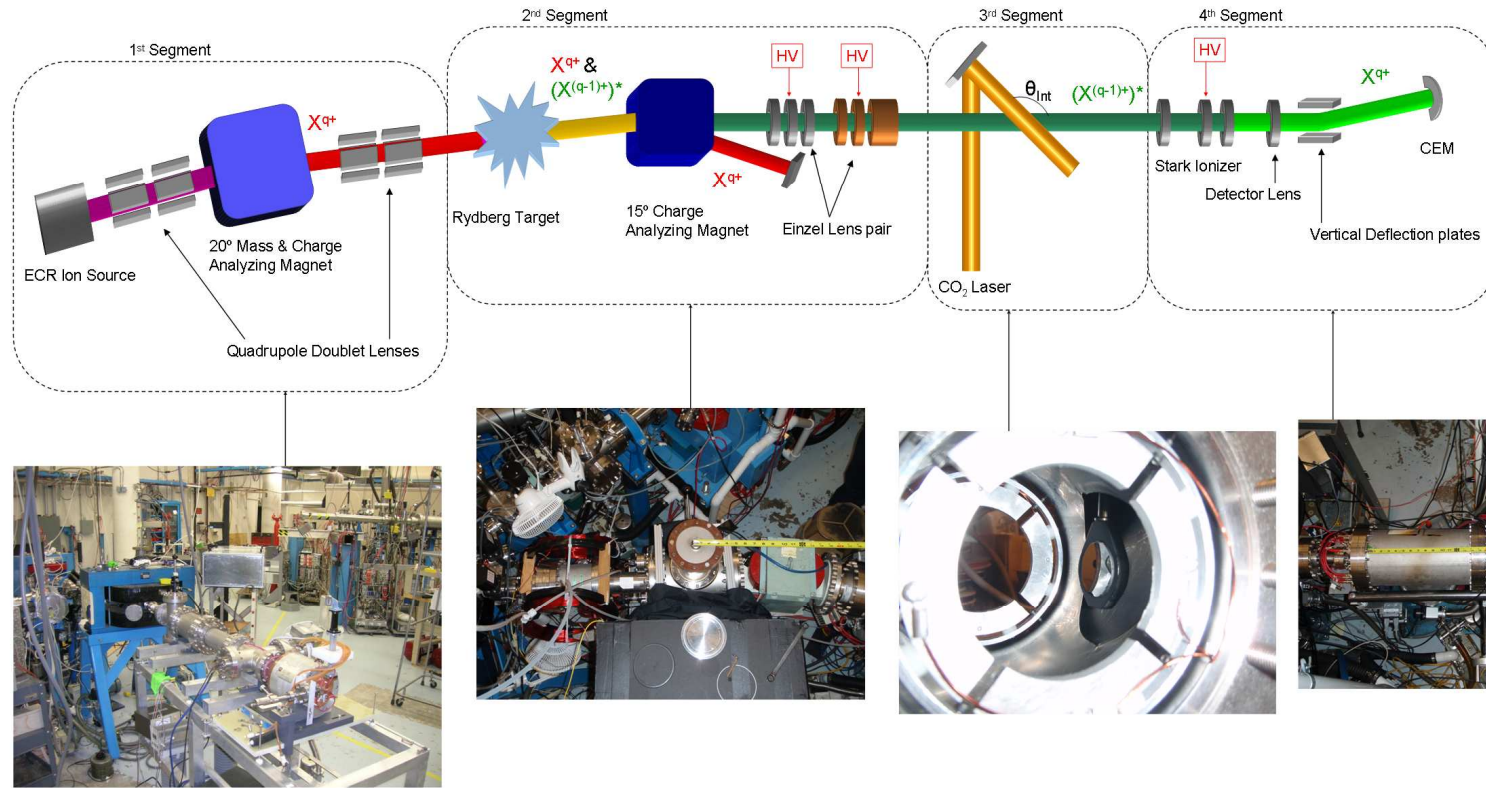


Figure 2.1: Schematic of the RESIS apparatus. The sections of the apparatus, as grouped and discussed in the text, are surrounded by dashed boxes. Along the top of the figure is a diagram of the apparatus showing graphical depictions of the components contained within the vacuum hardware shown in the photographs below. The graphical diagram shows the path of a hypothetical atom X with charge q as it progresses throughout the apparatus. The compensator has been neglected in the figure for clarity. The interior of the LIR assembly is shown in the photograph below to highlight the compensator and rotatable mirror used to vary the intersection angle the CO₂ laser makes with the ion beam.

2.2 Ion beam generation and selection

The ions studied in this work were produced using a 14 GHz permanent magnet ECR ion source manufactured by Xie Ion Equipment installed at the J. R. Macdonald Laboratory (JRML) at Kansas State University. This source easily produces multiply charged beams of any solid material that can be inserted into the ECR and attached to the sputter cathode. The ion source was maintained and operated by the staff at the J. R. Macdonald Lab and in general very little was required of the author to transport the desired ion beam through the RESIS apparatus.

The ion beams used in this research were generated by sputtering solid samples of Th or U metal. In order to create a beam of positively charged ions first a small amount of gas, called a seed gas, is introduced into the plasma chamber. The Xe seed gas is continuously fed into the plasma chamber during operation in order to sustain the plasma. Then microwaves with a frequency of 14 GHz are injected into the plasma chamber. The frequency of the microwaves is chosen to match the cyclotron frequency of the electrons in the magnetic field provided by a strong permanent magnet. The power of the injected microwaves was typically between 6 and 14 W for the studies presented in this work. The microwaves heat the electrons that are confined in the plasma chamber and these electrons ionize the gas inside the plasma chamber, forming positive ions.

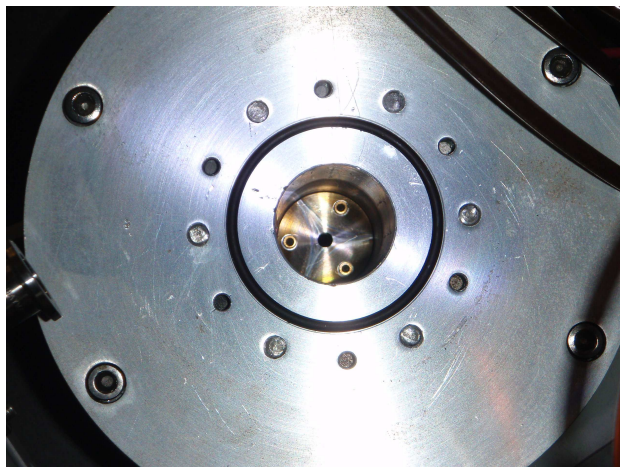


Figure 2.2: ECR Plasma chamber. The plasma created by the ECR is contained between the end plate with the small hole and the back of the ECR which has been removed to take this photograph.

The positive Xe ions strike a target, called a sputter target. The sputter target for this research consisted of a piece of either Th or U metal and was shaped to fit within the ECR plasma chamber, attaching by a small screw to the cathode feed-through and was held at a negative potential relative to the plasma. A sputter target of Pb metal is shown in the photograph in Figure 2.3.

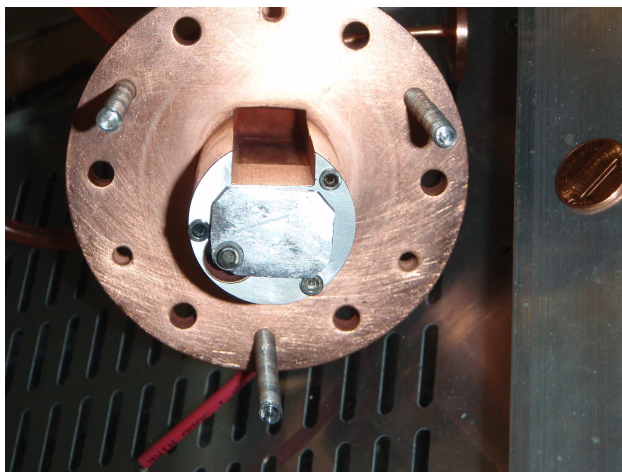


Figure 2.3: ECR sputter target. The Pb sputter target, shown mounted to the sputter cathode using a small screw was used to test the ECR ion generation capabilities during the initial phases of this research. The rectangular shape on the top of the sputter cathode mount is the microwave waveguide used to inject the microwaves into the plasma chamber. The penny on the right hand side of the photograph is shown for scale. The large copper back plate forms the back side of the ECR and mounts over the o-ring shown in Fig 2.2.

The sputter cathode is held at a negative potential relative to the ECR housing. For this work, the sputter electrode was typically held at potential between -500 to -2000 V depending upon the particular conditions inside the ECR on a given day. When the ions strike the cathode positive ions are ejected from the sputter target and enter the plasma. The entire ECR assembly is held at a high positive potential. The portion of the ECR held at high voltage is highlighted in Figure 2.4. The high voltage is supplied by a regulated Glassman model ER30P10.0-11 power supply. The positive potential draws the positive ions that are formed by the ECR's plasma out of the plasma chamber and down the rest of the beam line. Just on the other side of the extraction aperture is a set of vertical and horizontal deflection plates that are used to steer the ion beams as they exit the ECR.

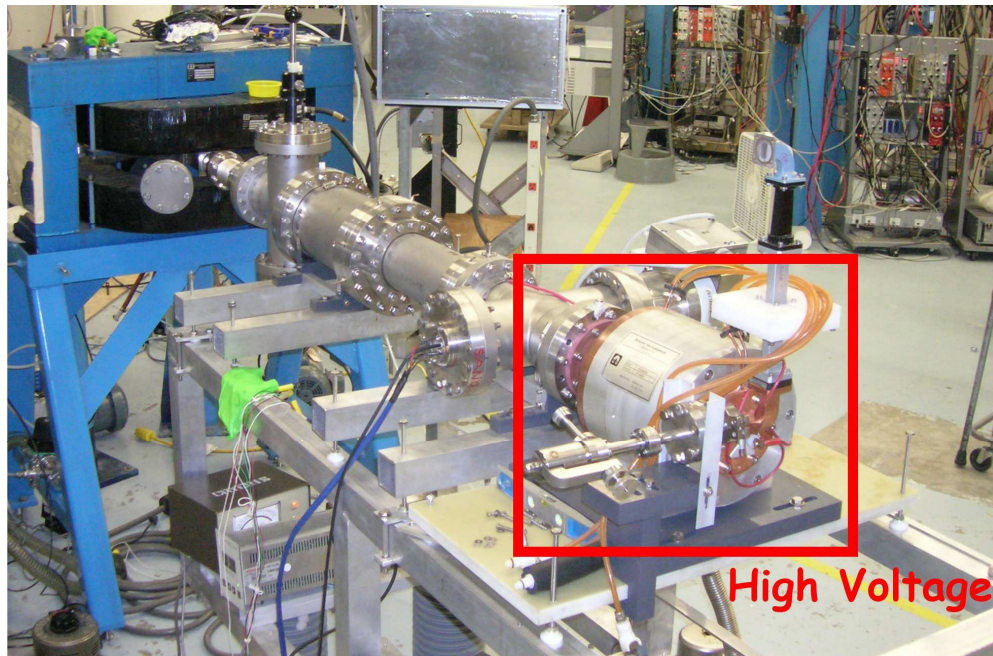


Figure 2.4: ECR ion source completely assembled. The portion of the photograph surrounded by the red box is held at a positive potential, relative to the rest of the beam line that is grounded. This causes the positive ions that are formed in the ECR plasma to be extracted from the plasma chamber. Combined with the exit aperture shown in Fig. 2.2 and the ion optics employed throughout the rest of the beam line, an ion beam is formed and transported to the RESIS apparatus where the experiments took place.

Following the ECR ion source is a series of ion optics that focuses and deflects the ion beams for transport through the rest of the apparatus. Just after the ECR ion source, shown in Fig. 2.4, a set of quadrupole doublet lenses were installed. These lenses, shown in Fig. 2.5, consist of a series of eight electrodes that are arranged around the ion beam. In total there are two sets of these lenses in operation for the entire RESIS apparatus, one set just prior to entry into the 20° magnet and then a set just following the 20° magnet. The second set of quadrupole doublet lenses has a set of magnet coils positioned around the lens assembly to provide additional vertical deflection of the ion beam if necessary. The potentials on the first set of quadrupole lenses were typically 700 V and 1160 V for the 150 keV U^{6+} beam. For the 100 keV Th^{4+} beam the first quadrupole lens had potentials of 1200 V axis and 1300 V applied. The second quadrupole lens had potentials of 1150 V and 1200 V applied for the U^{6+} beam and 1270 V and 1260 V for the Th^{4+} beam.

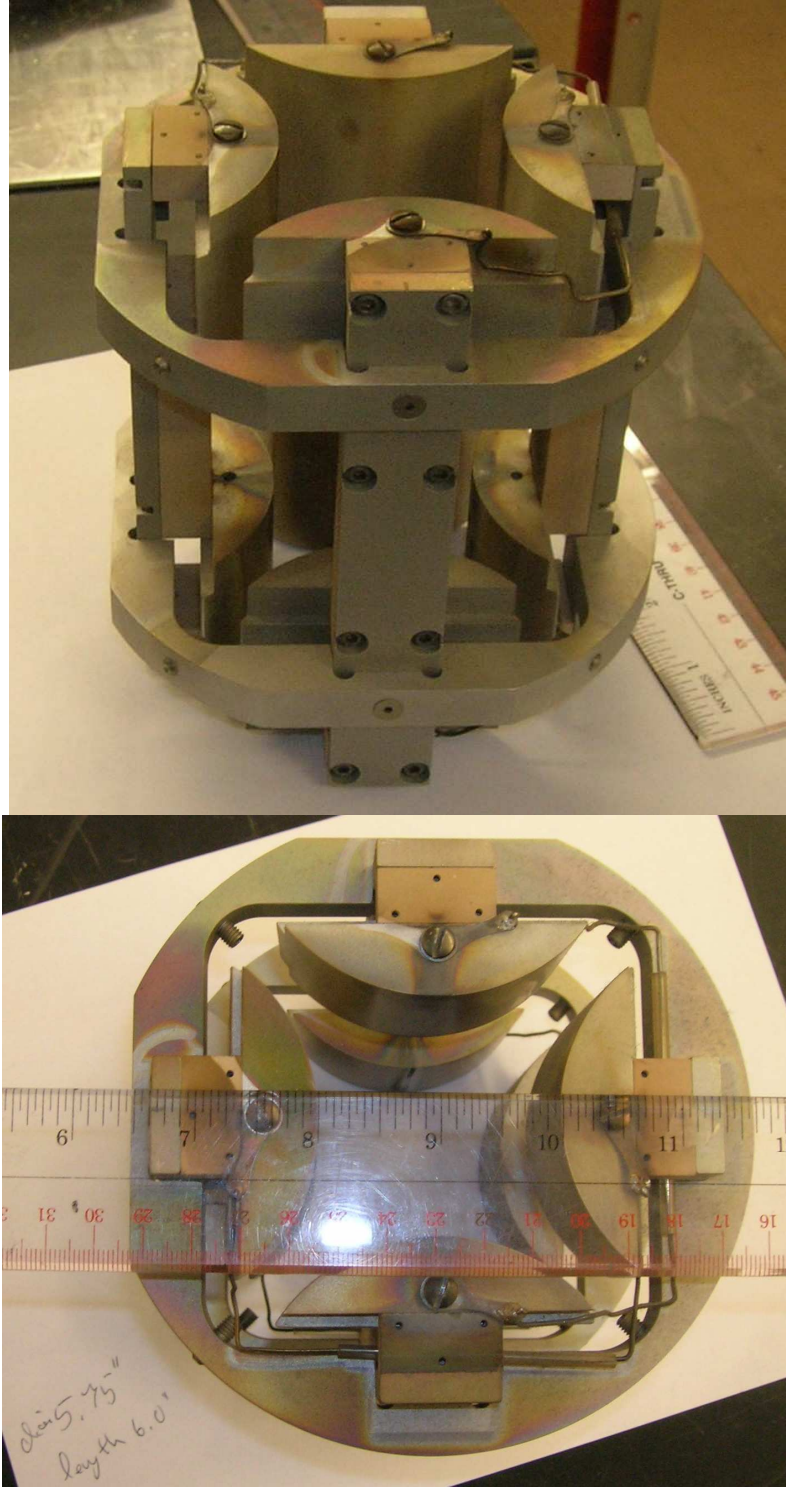


Figure 2.5: Quadrupole doublet lenses, extracted from the housings. The diameter of the opening between the adjacent electrodes is 2.125", an outer diameter of 5.75", and a total length of 6". Each lens set was installed in a 6" con-flat tube with high voltage electrical feed-throughs. The top image is a perspective view that shows the assembly and electrode arrangement and the bottom image is an axial view of the lens assembly.

After the ECR a 20° bending magnet separates the ion beams generated by the ECR by charge and mass. The 20° magnet operates in conjunction with a small 2 mm aperture, located 94 cm from the center of the magnet and mounted just prior to the Rydberg target and after the second quadrupole doublet lens, to allow only one beam of a given mass and charge at a time to propagate throughout the remainder of the RESIS apparatus.. Prior to this magnet all the beams generated by the ECR, regardless of charge and mass, are all traveling along the same direction.

The principle of operation of the 20° bending magnet is fairly straightforward. The magnitude of the force an ion experiences in an external magnetic field perpendicular to the direction of motion of the ion is given simply by,

$$F = qvB ,$$

where v is the velocity of the ion with charge q and B is the magnetic field applied. The velocity of the ion is dependent upon the mass of the ion, M_I , the charge of the ion, q , and the potential of the ECR, V_T , by

$$v = \sqrt{\frac{2qV_T}{M_I}} .$$

The deflection angle required to pass the ion beam through the 2 mm aperture can then be found to be related to the mass of the ion, charge, and magnetic field by

$$\Delta\theta = \frac{BL}{\sqrt{2V_T}} \sqrt{\frac{q}{M_I}} ,$$

where L is the length over which the magnetic field is present and can be approximated by the arc length of the magnet and is constant. From the above equation the dependence of the deflection angle on the charge and mass is clear. Thus, for beams of differing charge and mass different small deflection angles will occur. By varying the magnetic

field a spectrum of the beams is then generated. The magnetic field in the 20° magnet is measured by a Hall probe that was mounted between the coils. The ratio of M_I and q as a function of B can be used to identify the ion beams. A sample mass and charge analyzed spectrum is shown in Figs. 2.6 and 2.7 below for a Th sputter target in a Xe atmosphere. The two figures are shown to illustrate how the ECR conditions, namely the power of the injected microwaves, can vary the relative intensities of the various charged beams.

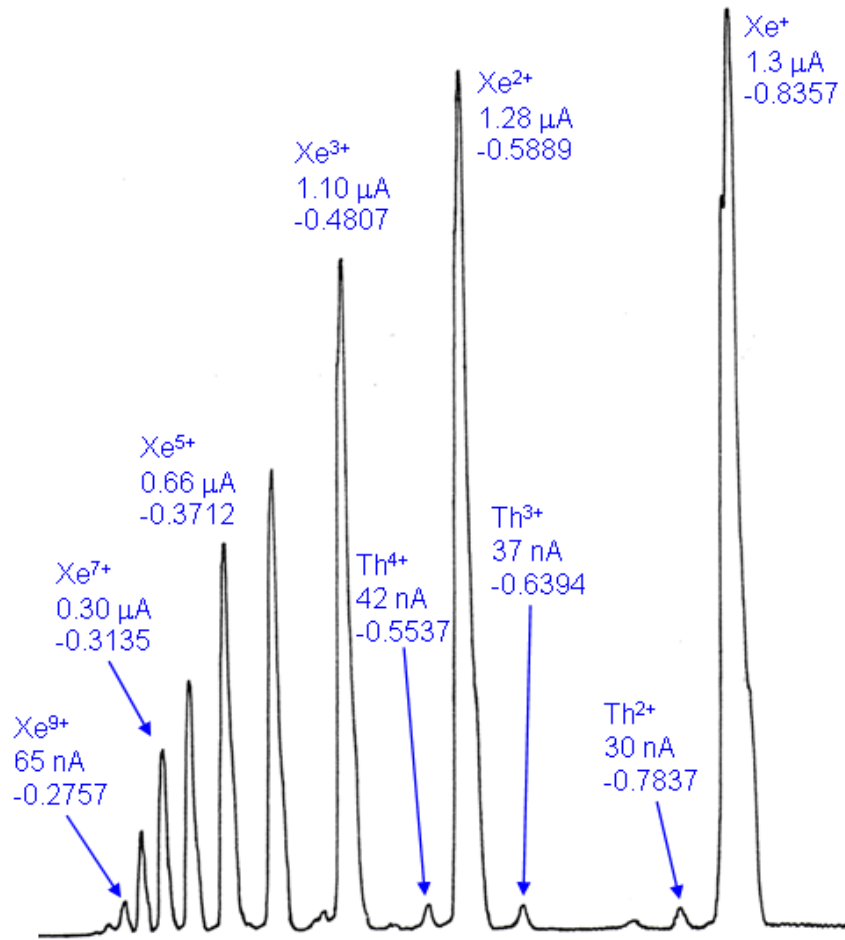


Figure 2.6: Spectrum of ion beams produced by the ECR as a function of the magnetic field in the 20° magnet. The beams are labeled by ion and also provided is the beam current and the hall probe reading of the magnetic field in the 20° magnet. The power of the microwaves injected into the ECR was 6 W to obtain distribution of charge states shown here. Some of the beams are unlabeled for clarity. Figure is reproduced from Book 12 page 71.

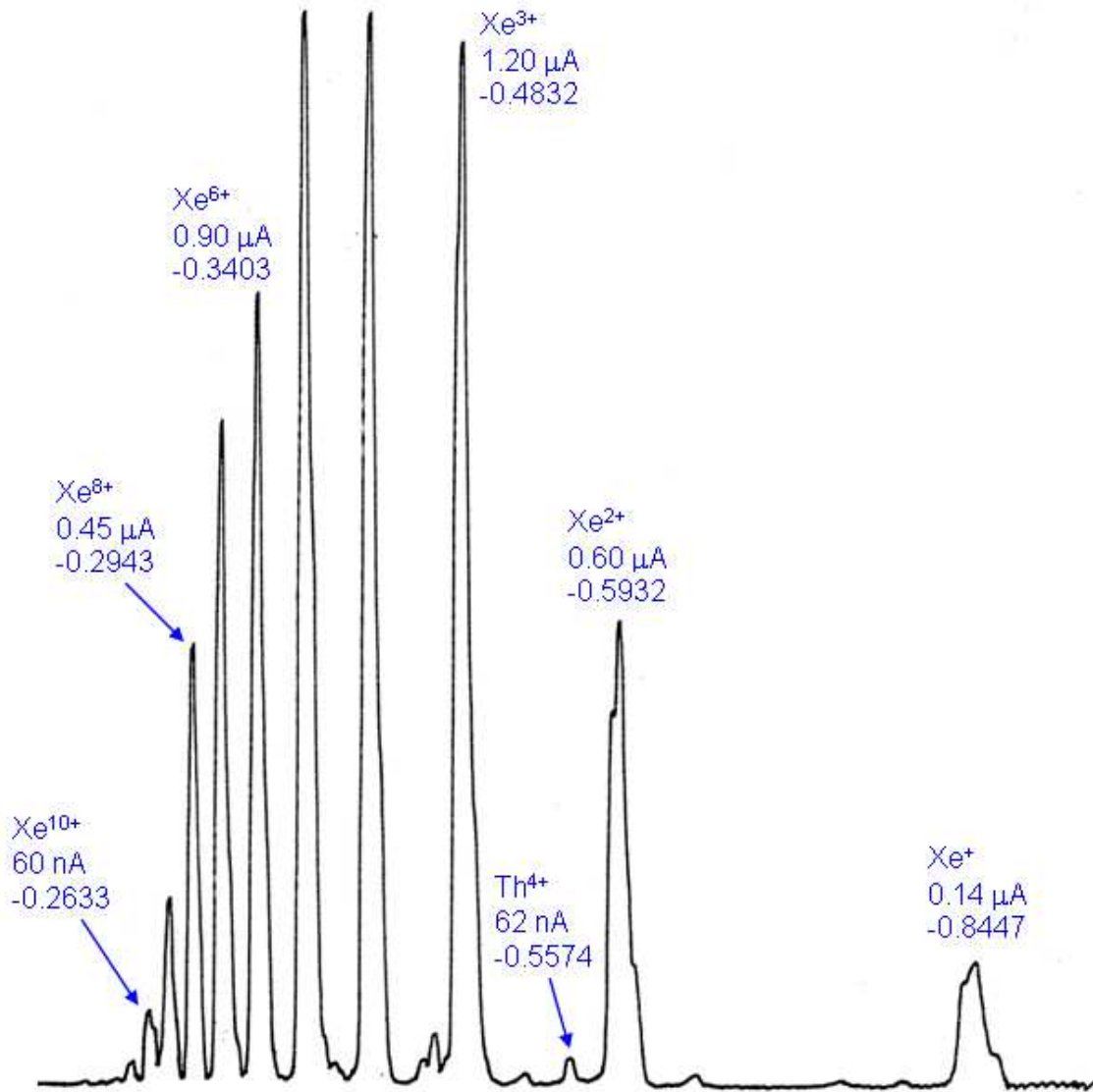


Figure 2.7: Spectrum of the beams produced by the ECR as a function of the field in the 20° magnet. This spectrum is similar to the one shown in Fig. 2.6. However, the power of the microwaves has been increased to 22 W. Higher power microwaves result in hotter plasma temperatures creating more highly ionized atoms, leading to the charge distribution shown here. With the higher power microwaves the charge distribution is now peaked toward the Xe⁴⁺ and Xe⁵⁺ beams in this figure compared with Fig. 2.5 where the charge distribution was peaked towards the Xe⁺ peak. This figure is reproduced from Book 12, page 77.

Characteristics such as the mass resolution, purity, velocity, velocity divergence, and angular divergence of the ion beams created by the ECR could impact the results of the measurements presented in this work. The mass resolution, $\Delta M/M$, of the beams can be

estimated from the above figures from the full width half maximum of the Th^{4+} peaks since Th has only one isotope [18]. Estimated in this fashion the mass resolution of the apparatus is:

$$\frac{\Delta M}{M} \approx 3.5\%$$

The velocity of the ion beam is of critical importance in determining the Doppler tuned laser frequency. Without careful calibration of the high voltage power supply used to extract the positive ions from of the ECR, it is impossible to know the final velocity of the ions to the accuracy desired for the measurement of the fine structure energies. The voltage output of the Glassman high voltage power supply as a function of the setting on the high voltage dial was measured using a 1/100,000 voltage divider and a Keithley model 197 microvolt DMM with a $>1 \text{ G}\Omega$ input impedance. The resistor across which the voltage is measured after the voltage divider is a $20 \text{ k}\Omega$ resistor. The effects of the input impedance of the Keithley DMM on the voltage measurement are negligible. The calibration of the potential to the high voltage dial setting is shown below in Fig. 2.8.

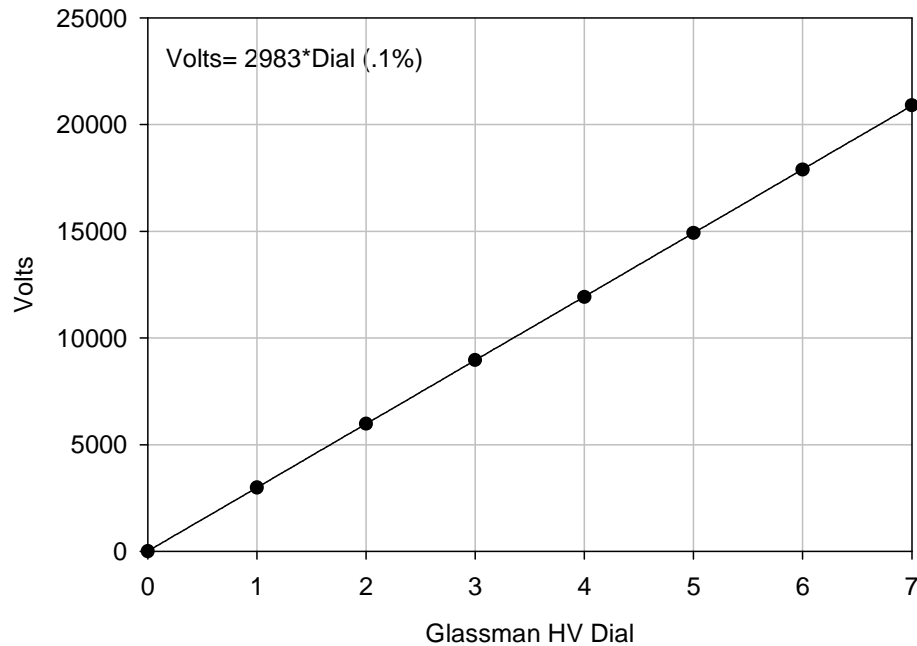


Figure 2.8: Calibration curve for the Glassman High Voltage supply used to supply the acceleration potential for the ion beams used in this experiment. This graphic is reproduced from page 50 in Book 4.

The voltage divider, in combination with three Agilent model 34401A digital voltmeters each with a $>10 \text{ G}\Omega$ input impedance, was calibrated by Julie Keele for the measurements of the Ni^+ fine structure pattern. The calibration of the voltage divider was carried out by observing the stage angle at which the CO_2 laser was Doppler tuned to be resonant with the eight Ar^+ transitions. The Doppler tuning of the CO_2 laser is described in Section 2.4. The properties of the Ar^+ ion were determined very precisely in a previous microwave study [19]. Using the properties determined previously the energies of the transitions were calculated. The beam velocity and perpendicular intersection angle were then adjusted to match the calculated transitions energies with the observed stage angle of the transitions [20]. The calibration of the voltage divider determined that the potential measured using the divider plus the Agilent DVM was lower than the actual potential, as determined by the beam velocity, by 0.31(8)%. The Keithley meter measurements were

consistent with the measurements reported by the Agilent meters, thus the calibration factor determined by Julie Keele was applied to the calibration curve shown in Fig. 2.8 as well. Thus, the terminal potential as a function of the HV dial setting, *Dial*, is given by:

$$V_{ECR} = 2992(3) \cdot Dial$$

For day to day voltage measurements a hand-held high voltage probe with a division factor of 1/1000 was also calibrated. The 1/1000 high voltage probe was manufactured by Fluke and is a hand-held model that plugs directly into a Fluke Model 83 digital multi-meter using a banana-plug. Table 2.1 lists the calibrated voltage measurements and the hand held probe measurements. The first column lists the lab book page where the dial setting in the second column can be found and the hand held probe measurement listed in the last column. The third column lists the potential calculated from the fit to the calibration plot in Fig. 2.8. The fourth column lists the potential calculated when the calibrated fit of the potential is corrected by the 0.3% underestimation of the Glassman high voltage divider that was observed by Keele [21]. The hand held high voltage probe fortuitously agrees with fourth column in Table 2.1. The calibration of the power supply potential of $V_{ECR} = 2992(3) \cdot Dial$ matches within 0.04% of the hand held probe measurements on the apparatus used for this experiment at the ~25kV potentials used for the observations presented in this work. It was therefore useful for convenient voltage checks.

Table 2.1: Measurements of the Fluke hand-held high voltage probe at various dial settings. At higher voltages the meter used to measure the hand held high voltage probe switches scales again only giving two digits past the decimal. There is a clear discrepancy between the third and fifth columns. The fourth and fifth columns agree much more closely, except at very low voltages.

Lab Book and Page	HV Dial Setting	2983*Dial (V)	2992*Dial (V)	1/1000 HV Hand-held probe measurement (V)
12-093	1.340	3997	4009	4.015×10^3
11-005	5.00*	14915	14960	14.93×10^3
12-003	8.33	24848	24923	24.94×10^3
12-027	8.335	24863	24938	24.95×10^3
13-059	8.360	24938	25013	25.02×10^3
11-056	8.38	24998	25072	25.10×10^3

The velocity spread of the ion beam created by the ECR could be an important factor in determining the lower limit of the width of the resolved transitions. An estimate on the energy spread of an ECR ion source is given by R. Pardo as:

$$\Delta E \approx 5q \text{ eV [22].}$$

Using this scaling rule, for the Th^{4+} experiments carried out in this work, the energy spread can be estimated to be ~ 20 eV. Thus the velocity spread can be estimated to be:

$$\frac{\Delta v}{v} \leq \frac{20 \text{ eV}}{100 \text{ keV}} = 0.02\% .$$

Another characteristic of the ion beam that is of importance is the angular divergence of the ion beam. The 6 mm diameter aperture that is at the entrance to the detector sets a limit on the divergence of the beam. Assuming that the beam is focused to a point at the 2 mm entrance aperture to the apparatus and diverges to fill the entire detector entrance aperture located 170.2 cm away, the maximum divergence of the beam is approximately ± 1.8 mrad ($\pm 0.10^\circ$) from center. These apertures also put limits on the instability of the beam pointing. The largest acceptance of the beam is $\pm 0.10^\circ$, this implies that at most the beam direction can change by $\pm 0.10^\circ$ from center. If the beam fills the entire aperture

then the resulting image on the beam viewer would be circular due to clipping of the beam off of the edges of the aperture. The shape of the beam imaged by a beam imaging system at the end of the beam line always showed that the beam is not diverging enough to clip off the edges of the entrance aperture in the detector.

The width of a RESIS transition arising from the angular divergence of the beam can be estimated if the beam angular distribution and homogenous width due to finite transit time through the CO₂ laser (described in Section 2.4) are the dominant sources of width. Assuming the beam distribution to be Gaussian the convolution integral of two Gaussians can be evaluated. Performing the integration, the width of the resulting Gaussian is found to be:

$$b_{Total} = \sqrt{b_H^2 + b_{IH}^2} , \quad (2.1)$$

where the b 's in the above equation are related to the full width half maximum of the Gaussians by

$$b \approx \frac{FWHM}{2.35} , \quad (2.2)$$

$2.35 \times b_H$ is the full width half maximum arising from homogenous sources, and $2.35 \times b_{IH}$ is the full width half maximum arising from inhomogeneous sources. Equation (2.1) can be used to give an indication of the angular divergence of the beam if the Stark width is neglected. Typical angular full width half maxima of RESIS transitions observed, when the stray electric field was believed to be minimized, was $\sim 0.28^\circ$. A typical tuning rate for the transitions observed in this experiment was 916 MHz per stage degree. Thus the 0.28° FWHM can be converted from stage degrees to a frequency FWHM of 256 MHz. The FWHM arising from the finite transit time of the CO₂ laser is estimated to be 120 MHz typically in this experiment. Applying Eq. (2.1) leads to the estimation that the

beam FWHM is 226 MHz, or 0.25° . This seems rather large considering the total acceptance angle of the apparatus is at most $\pm 0.10^\circ$ from center. This could imply that there were other sources of width, presumably the Stark width, that are contributing to the homogeneous width of the transition. The estimate of the FWHM divergence of the beam determined here can be viewed as an extreme upper limit. This upper limit is then $\pm 0.125^\circ$ from center.

Due to the nature of the ECR some of the sputtered U and Th metal is deposited on the inside walls of the plasma chamber. This can cause recycling of the sputter material when the plasma is present such that even when the sputter target is removed, beams of Th and U can still be present in the spectrum. Due to the close proximity in mass of the two ions it is possible that there could be U^{4+} present during the observation of the Th^{4+} spectra and Th^{6+} present during the observation of the U^{6+} spectra. In the case of the Th^{4+} observations the ground state configuration of U^{4+} is 3H_4 [2] which would produce a very complex Rydberg fine structure pattern. While the resolved Rydberg transitions in U^{4+} would produce a very feature rich spectra, it could also contain a very prominent peak of unresolved transitions between very high L states. This peak, referred to as the high- L peak throughout this work, would coincide closely to the intersection angle with the Th^{4+} high- L peak. The same is most likely to be true for Th^{6+} contamination with U^{6+} . The ground state configuration of Th^{6+} is not known. However, the high- L peak from Th^{6+} would not be resolved from the dominant U^{6+} high- L peak.

Another issue that arises in general with the RESIS technique is the inability to clearly distinguish between different isotopes of the same element in the beam, without great effort. According to the NIST isotope database Thorium metal exists solely as

^{232}Th [18]. According to the same database the natural abundance of U metal is 99.3% ^{238}U , 0.7% ^{235}U , and a very small fraction of ^{234}U . For the U studies the Uranium metal used was depleted of the ^{235}U isotope and therefore the ^{238}U was taken to be the only isotope observed. Since both elements dominantly occur in one particular isotope the effects of different isotopes on the observed Rydberg fine structure spectra were ignored.

2.3 Rydberg state population creation

In order to selectively populate the high L Rydberg states of interest a Rydberg target is used. The type of Rydberg target used for this work has been used in many different experiments [8,14,23] and well described in other publications [15,24,25]. Only a basic understanding of the Rydberg target was required for the experiments carried out in this work. A brief description of the target and the underlying principles of the target will be discussed here.

The Rydberg target consists of a thermal beam of rubidium that is excited from the ground state to a selected upper state. The thermal beam of rubidium is first excited from the $5S_{1/2}$ ground state to the $5P_{3/2}$ state using a 780 nm New Focus Vortex diode laser. The excitation from the $5P_{3/2}$ state to the $4D_{5/2}$ state is achieved using another New Focus Vortex diode laser with a wavelength of 1529 nm. The lasers used in the first and second steps of the excitation are locked to the transition frequencies by a pair of peak locking boxes. The principle operation of the lock boxes is to dither the frequency of the laser over a small frequency range while monitoring the amount of fluorescence in a Rb vapor cell with a photodiode. When the lasers are on resonance with their respective transitions, a clear peak is seen in the trace of the output voltage of the photodiode on an

oscilloscope. The peak lock box attempts to stay at the peak of the fluorescence by adjusting the voltage supplied to the laser diode, thus making small adjustments in the frequency of the laser. The final step in the excitation, from the $4D_{5/2}$ state to the $nF_{7/2}$ state is performed using a tunable frequency Ti:Sapphire laser. Figure 2.9 shows a simple level diagram of the stepwise excitation scheme from the Rb ground state to the various final states that were used in this experiment.

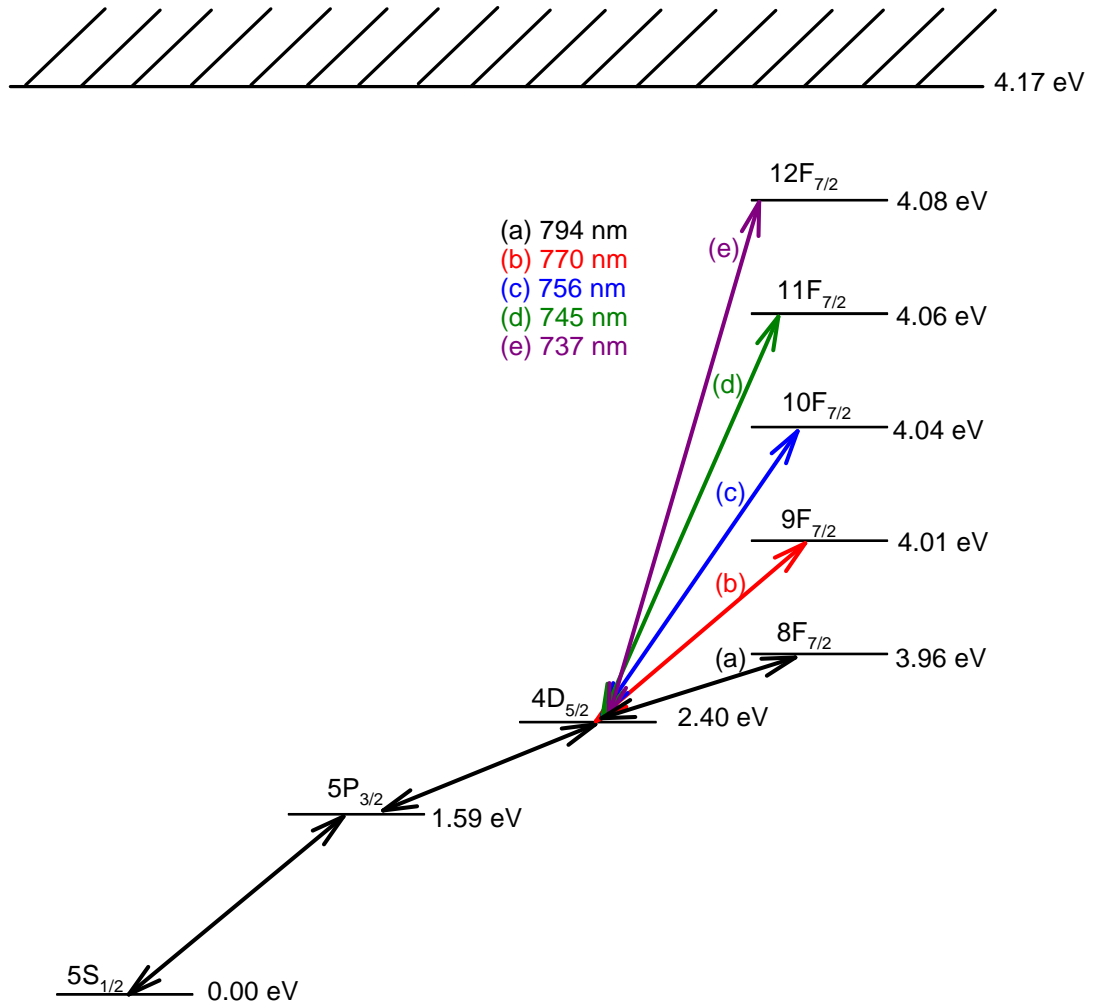


Figure 2.9: ^{85}Rb excitation scheme used for the creation of the Rydberg target used in this work. Stepwise excitation from the ground state to the $4\text{D}_{5/2}$ state is made using two CW diode lasers at the frequencies shown in the figure. The final excitation is made with a tunable Ti:Sapphire laser. The frequency of the Ti:Sapphire laser is chosen to match the resonant frequency between the $4\text{D}_{5/2}$ state and one of the $n\text{F}$ states shown. The spacing between levels has been adjusted for clarity.

The Ti:Sapphire laser used in this experiment is the same laser detailed in Daniel Fisher's dissertation [15]. When the Ti:Sapphire laser frequency is tuned the final transition in the excitation scheme a blue fluorescence is observed. This mirrorless maser transition has been described previously [24] and has been observed for all target final states used in this research. The blue emission could be monitored by a phototube and

used to trim the frequency of the third laser, which was otherwise free-running. In practice it was simpler to trim the third laser frequency by monitoring the CEM DC level in the Rydberg detector, since the background was absent if the target was off. The transition frequencies to the final target nF state from the $4D_{5/2}$ state used in this work had been previously determined by Fisher [15]. The transition frequencies used for the Rydberg target in this work are reproduced in Table 2.2 for reference. The Ti:Sapphire laser light is transported to a small optical surface which is mounted to the side of the target chamber on the beam line through a single mode optical fiber.

Table 2.2: Rb final state transition frequencies used in this work. The frequency of the final transition was measured using a Burleigh Model WA-20 wave-meter when the blue mirrorless maser transition was observed.

Final Target state	Predicted Frequency (cm^{-1})	Measured Frequency (cm^{-1})
$8F_{7/2}$	12614.37	12614.38
$9F_{7/2}$	12976.13	12976.15
$10F_{7/2}$	13234.76	13234.78
$11F_{7/2}$	13426.05	13426.08
$12F_{7/2}$	13571.49	13571.51

The unique advantage of having a Rydberg target with a selectable final state over other experiments where the final state of the target is fixed is that the distribution of states which capture an electron from the target to form Rydberg states can be tailored to match the current ion beam of interest. The capture cross section can be predicted using a Classical Trajectory Monte Carlo code developed by Ron Olson [26] to model the capture process between rubidium and Rydberg ions. The same code is described in detail in Daniel Fisher's dissertation [15]. Using the CTMC simulation the capture cross section of the excited electron into a given Rydberg state with principle quantum number n can be estimated as a function of the final nF state of the target. These simulations were used to estimate which final target state would produce the largest resolved RESIS

signal. Figure 2.10 shows the distribution of the capture cross sections into a given n for the 10F, 12F, and 14F targets for a Th^{4+} ion travelling at a velocity approximately 0.1% the speed of light. It was shown by Huang *et al.* [25] that the capture cross section drops off rapidly when

$$v \geq \frac{q^{2/7}}{n_T}$$

where v is the velocity of the ion beam in atomic units, q is the charge of the ion beam, and n_T is the target state. Although this behavior was not studied in detail in this work, it was an important consideration taken into account when deciding upon which target states to use.

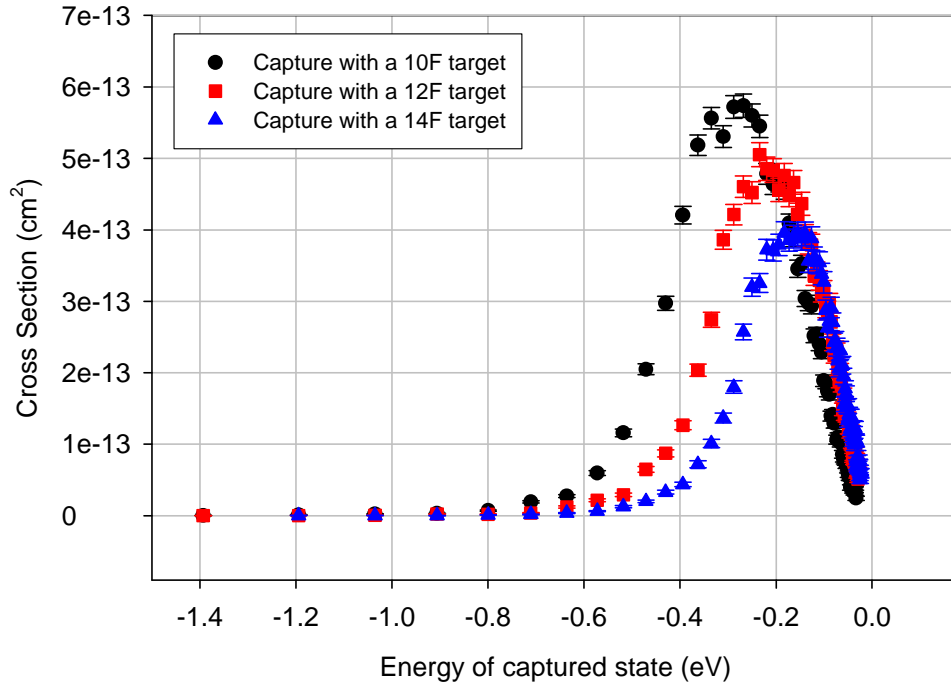


Figure 2.10: Capture cross section as a function of n for various target states for 100 keV Th^{4+} . As the target state increases, the peak of the capture distribution increases towards higher n as well, yet the total capture cross section decreases slightly. The 10F target was used in the observations presented in this work.

The Rydberg target is contained in a six way stainless steel cross with 10" Con-Flat ports on the ends and four ISO-100 flanges arranged around the middle. The ion beam enters through a 2 mm aperture; the 2 mm aperture is approximately 0.50" from the beam of rubidium to ensure that the ion beam intersects with the Rydberg target. The target chamber can be thought of in three sections. The lower section of the target is where the rubidium is heated. This lower section consists of a vessel for the containment of the supply of rubidium and a band heater element to vaporize the rubidium metal. The inner band heater used is an Omega MB1A1A1A1 heater that is 1" tall, a 1" inner diameter, and a resistance of 140 Ω . Typically, the heater was run at a power of 5.3 W to yield a Rydberg target that provided a capture ratio of 2% or greater. Below this section is mounted a diffusion pump which provides the vacuum in this lower portion of the target chamber. The thermal beam of rubidium is collimated through two ~3 mm holes in the top of the rubidium containment vessel and the outer casing of the lower target region. This outer casing serves to isolate the contaminated vacuum in the lower target chamber where the rubidium is heated from the relatively cleaner vacuum above. A schematic of the lower target region is shown in Fig. 2.11. The outer shell of the target is heated by a second heater that is an Omega MB2A1A1A1 band heater and is typically operated with a potential of 19 V. This outer heater is used to prevent clogging of the upper hole in the lower section. Typical pressure in the region of the target chamber was 3×10^{-6} T.

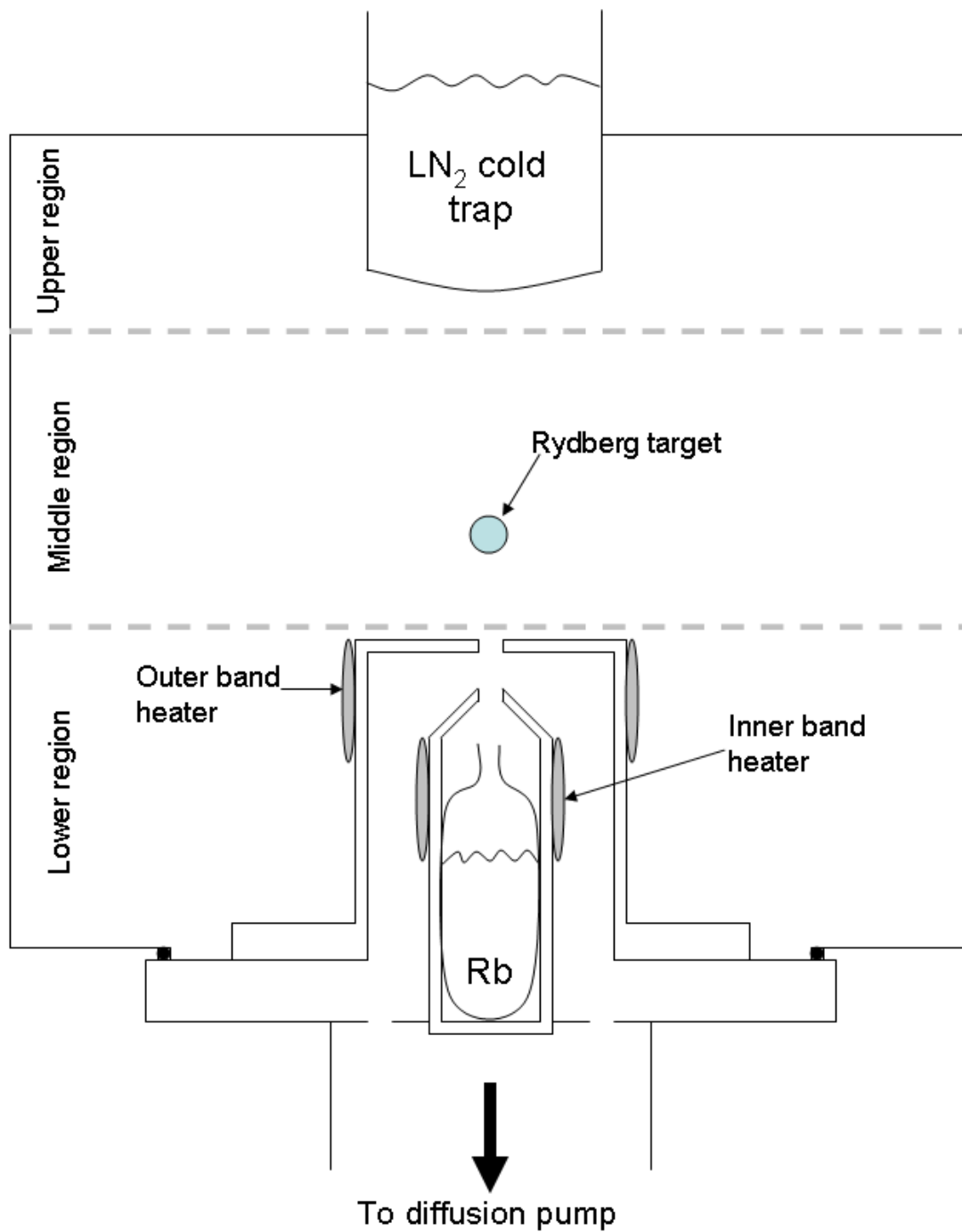


Figure 2.11: Schematic of the lower target region. Schematic is not to scale but shows the basic construction of the Rydberg target and the separate regions in the target chamber.

The section above, the middle section, is where the ion beam and excited rubidium beam intersect forming Rydberg states. The optical hardware necessary for the excitation of the thermal rubidium beam is mounted on a 2' x 4' optical table that is mounted to the target chamber using 80-20 hardware. A photograph of the optical table layout for the excitation of the rubidium is shown in Fig. 2.12 with the paths of the three CW lasers used in the excitation highlighted. The upper region is simply a stainless steel surface cooled by liquid Nitrogen that collects the Rb vapor in the target region.

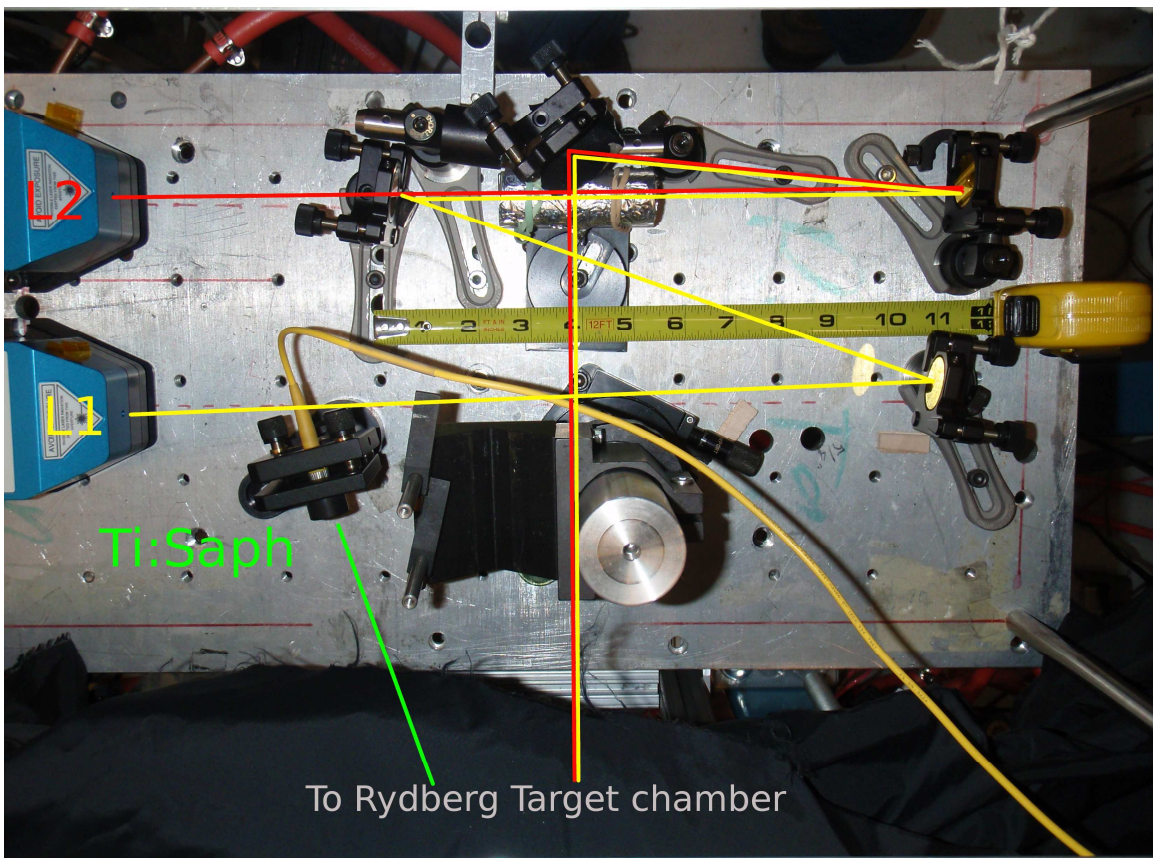


Figure 2.12: Optical layout used to excite the thermal plume of Rb. The arrows correspond to the different lasers as identified. The first two lasers are combined using a beam splitter. The Ti:Sapphire laser is simply transported using an optical fiber. The three lasers all intersect at the center of the Rb plume in the target chamber. The optical table is attached to the support framework using two manual motion stages which provide easy adjustment of the vertical and horizontal position of the point of intersection of the three laser beams. This adjustment allows for manipulation of the target position to maximize the RESIS signals. The lasers labeled L1 and L2 in the figure correspond with the transitions shown in Fig. 2.9.

Following the Rydberg target is a charge analyzing magnet. This particular magnet has a bending angle of 15° and a radius of curvature of 24" which operated in conjunction with a 0.50" diameter aperture located 20.3 cm beyond the end of the end of the magnet to separate the beam of Rydberg ions formed in the Rydberg target from the ions that did not capture an electron. The principles of operation of this magnet are identical to that of the 20° mass and charge analyzing magnet just after the ECR ion source. The tuning of the magnetic field required to steer the primary beam through the 0.50" aperture at the exit flange of the magnet can be derived in the same manner as that for the 20° analyzing magnet. Once the magnetic field, B , required to transport the primary beam is known the magnetic field, B' , required for the transport of the Rydberg ion beam through the remainder of the RESIS apparatus can be determined by the simple relation

$$B' = \frac{q}{q-1} B.$$

In much the same way as for the 20° magnet, a Hall probe was installed between the two poles of the 15° magnet to measure the magnetic field.

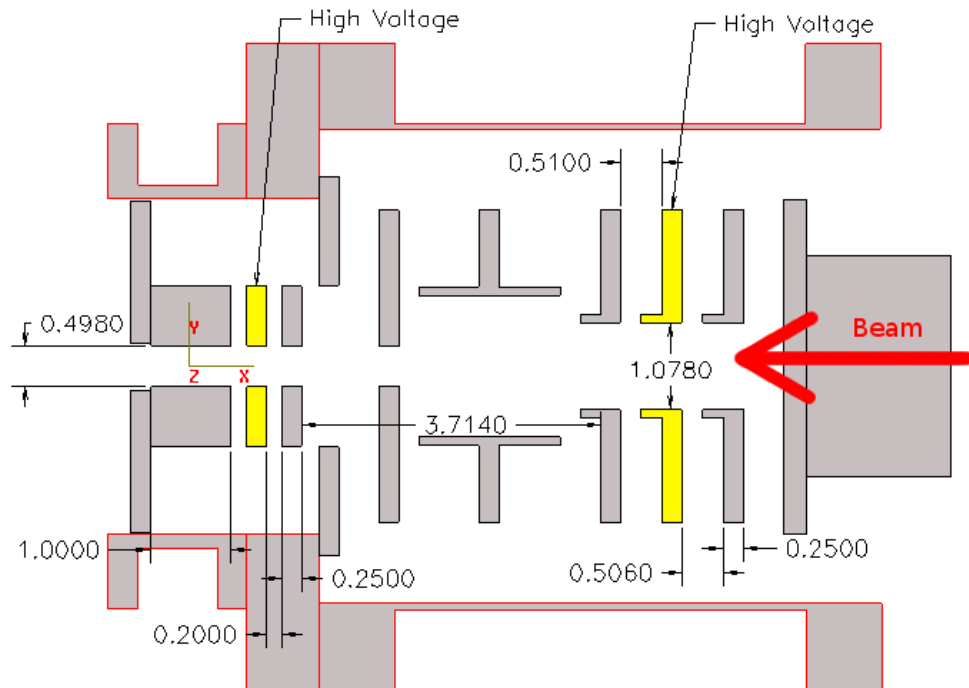
Following the 15° charge analyzing magnet is an assembly containing two Einzel lens assemblies. Just prior to the pre-ionizer and remixer Einzel lens assemblies is a set of plates arranged to the left, right, top, and bottom of the ion beam path. A balanced voltage can be applied to these plates forming an electric field just prior to the entrance aperture into the first Einzel lens. These plates serve to finely steer the ion beam through the lens assembly. A cutaway view of the pre-ionizing and re-mixing lens assembly is shown in Figure 2.13.

The first Einzel lens in the assembly, the pre-ionizing lens, focuses the beam for transport while also ionizing any ions in the Rydberg beam that have captured an electron

in a high n state. Very high- n Rydberg states are ionized in the RESIS detector in order to observe the RESIS signals. The pre-ionization of these very high- n states eliminates the initial population in these states, significantly reducing the background in the observation of the RESIS signals. The field in the pre-ionizing lens ionizes any Rydberg states with

$$n \geq \sqrt[4]{\frac{2Q^3}{F}},$$

where F is the field in the pre-ionizing lens in atomic units and Q is the charge of the ion core [15].



All Dimensions in Inches

Figure 2.13: CAD schematic cutaway of the Pre-ionizing and Re-mixing lens assemblies. The ion beam enters from the right hand side of the page and exits on the left hand side of the page. The electrodes are mounted on stainless steel support posts and spaced using 0.50" ceramic spacers. The posts are insulated from the high voltage lens electrodes using Mullite sleeves. The assembly is a modification of a Colutron model 200-B lens system. Electrodes colored in yellow are held at high voltage and electrodes colored in grey are grounded internally.

Following the pre-ionizing lens assembly is a second Einzel lens that also serves to focus the beam for transport. A SIMION simulation of the axial electric fields present in the pre-ionizing and re-mixing lens assemblies is shown in the bottom of Fig. 2.14 for typical potentials used in this work. The pre-ionizing and re-mixing lenses are intended to repopulate the lower L Rydberg states that might be resolved by laser excitation in the LIR. The repopulation mechanism is explained in the following chapter and is accompanied with data testing the function of the lenses.

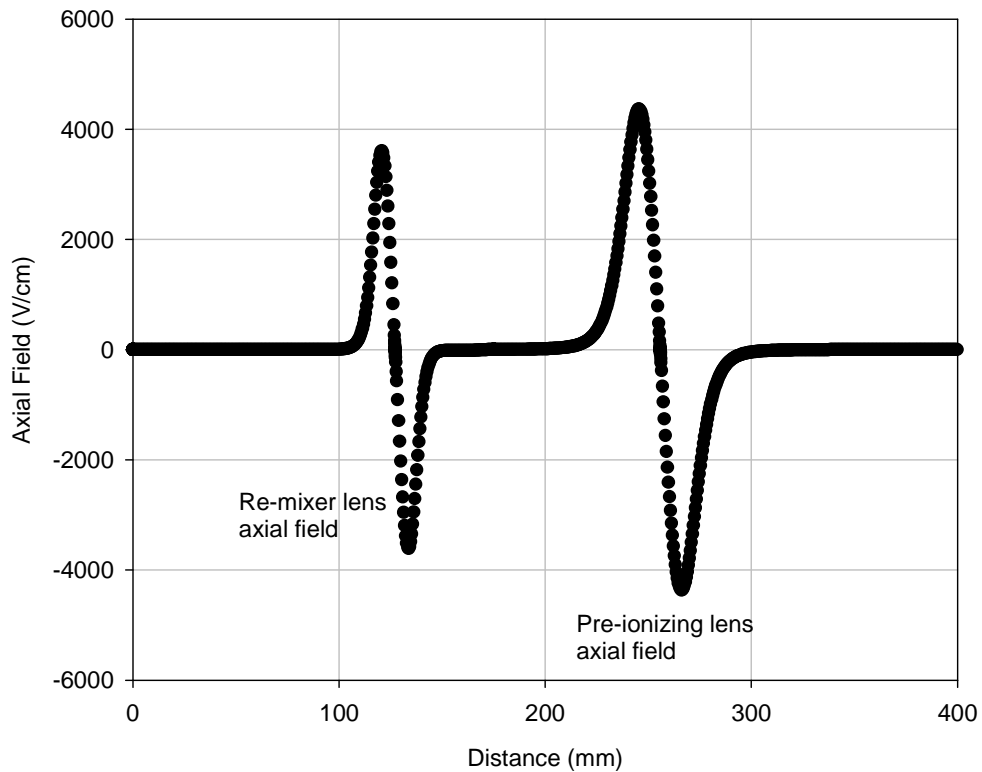
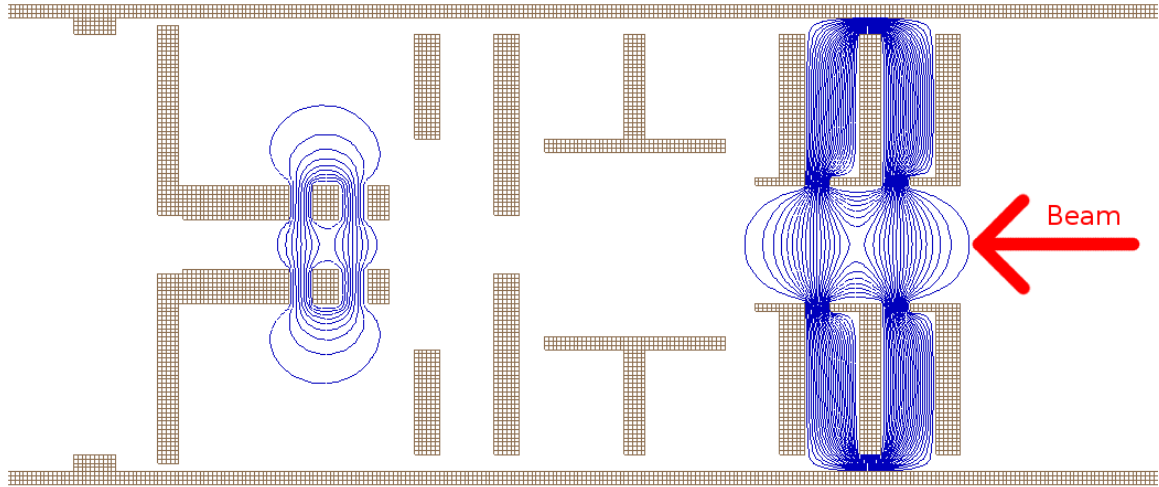


Figure 2.14: SIMION simulation of the fields present in the Pre-ionizing and Re-mixer lens assembly when a potential of 10.5 kV is applied to the Pre-ionizing lens electrode and a potential of 4.0 kV is applied to the remixing lens electrode. The effective lens distance, the ratio of the maximum E-field to the potential applied, of the two elements is 2.4 cm for the pre-ionizing lens and 1.1 cm for the re-mixing lens. The x-axis is relative to the SIMION potential array's origin, shown in the top figure start.

2.4 Laser Interaction Region

Following the Remixer lens is the Laser Interaction Region (LIR), a critical device in the RESIS technique. In the LIR a Rydberg state with n and L is excited to a much higher n' state with $L' = L \pm 1$ through the use of a CO₂ laser. The CO₂ laser is convenient to use in this application because of the closely spaced lasing lines that are in a range of frequencies that are close to the Rydberg transition frequencies between n and n' , as illustrated in Fig. 1.2. The available power from the CO₂ laser is typically high enough to saturate the transition. The probability of an excitation of an atom passing through a Gaussian beam can be modeled by employing time dependant perturbation theory for a simple two level system. A derivation of the transition probability for an atom excited by a TEM_{0,0} laser beam has been given by C. R. Quick and H.C. Bryant [27]. In the small field limit the excitation of the transition probability for an excitation from state $|n, L\rangle$ to $|n', L'\rangle$ is given by

$$P_{a \rightarrow b} = \pi \left(\frac{e}{2\hbar} \right)^2 \left[\frac{w_0}{w(z)} \right] \left(E_0 \cdot T \cdot \langle n, L | Z | n', L' \rangle \right)^2 \exp \left[-\frac{1}{2} (\omega' - \omega_0)^2 \cdot T^2 \right]. \quad (2.3)$$

where w_0 is the waist of the Gaussian laser beam, $w(z)$ is the distance from the center of the laser beam at which the intensity drops by $1/e$ a distance z from the waist, E_0 is the peak electric field at the beam waist, T is the transit time through the CO₂ laser beam waist, $\langle n, L | Z | n', L' \rangle$ is the matrix element representing the dipole transition between the two states and is evaluated with the aid of Eq. (60.7) in Ref. [28], ω_0 is the center frequency of the transition, and ω' is the driving frequency of the excitation field, in this

case the Doppler tuned frequency of the CO₂ laser. The transit time through the CO₂ laser beam waist is given by

$$T = \frac{w_0}{v \cdot \sin \theta_{int}} \quad (2.4)$$

where v is the velocity of the ion beam and θ_{int} is the intersection angle formed between the CO₂ laser and the ion beam. An interesting feature of this line shape is that its width depends on w_0 and not on w , the laser beam radius at the point of intersection. The typical power for the CO₂ laser used in the studies carried out in this work was 10 W and is in a TEM_{0,0} mode. The electric field is related to the CO₂ laser power, P , by

$$E_0 = \sqrt{\frac{4 \cdot \eta \cdot P}{\pi \cdot w_0^2}} \quad (2.5)$$

In Eq. (2.5) η is the wave impedance given by

$$\eta = \sqrt{\frac{\mu_0}{\epsilon_0 \cdot n}} \quad (2.6)$$

where n is the index of refraction of the material in which the Gaussian wave is travelling. In MKS units $\eta \approx 376.73 \Omega$. The waist of the CO₂ laser is $w_0 = 0.9$ mm according to the laser documentation, implying a field of 770 V/cm at the typical power of 10W. The diameter at the point of intersection with the ion beam, z , is given by

$$w(z) = \sqrt{w_0^2 \left[1 + \left(\frac{\lambda_0 \cdot z}{\pi \cdot w_0^2} \right)^2 \right]} \quad (2.7)$$

The distance from the output lens of the CO₂ laser to the intersection point with the ion beam in the LIR is 62.3" (0.1582 m). For the typical CO₂ laser wavelengths used in this work the diameter of the spot, given by Eq. (2.7), is 1.1 mm. The transition probability given in Eq. (2.3) neglects the effects of power broadening and saturation on the

transition. A typical value of $\langle 37,10|Z|73,11 \rangle$ in Th^{4+} , taking the RMS value over all possible m 's, is 0.4182 a.u. Taking the 10W typical power then the transition probability in Eq. (2.3) is found to be 19.5, well above saturation. All the transitions in this work were in the saturation regime according to Eq. (2.3).

A diagram of the LIR is shown in Figure 2.15. The LIR is constructed from a 6" conflat 4-way cube. Initially the CO_2 laser beam enters the region nearly perpendicular to the direction of propagation of the ion beam through a ZeSe window. The laser beam is then reflected off of a gold mirror at an angle. The mirror is attached to a rotatable post. By rotating the post the angle at which the reflected CO_2 beam intersects the ion beam is varied, a small bent piece of μ -metal is attached to the opposite wall preventing further interaction of the CO_2 laser with the ion beam by deflecting the laser beam off towards the top or bottom of the LIR. The rotation of the post on which the mirror is mounted is controlled by a Newark Model 496 rotation stage. The rotation stage is controlled by a Newark PMC200-P control module. This control module can be either locally controlled using the interface on the front panel of the device or connected to a PC via GPIB interface, allowing for remote control using a program written in LabVIEW 8.2.

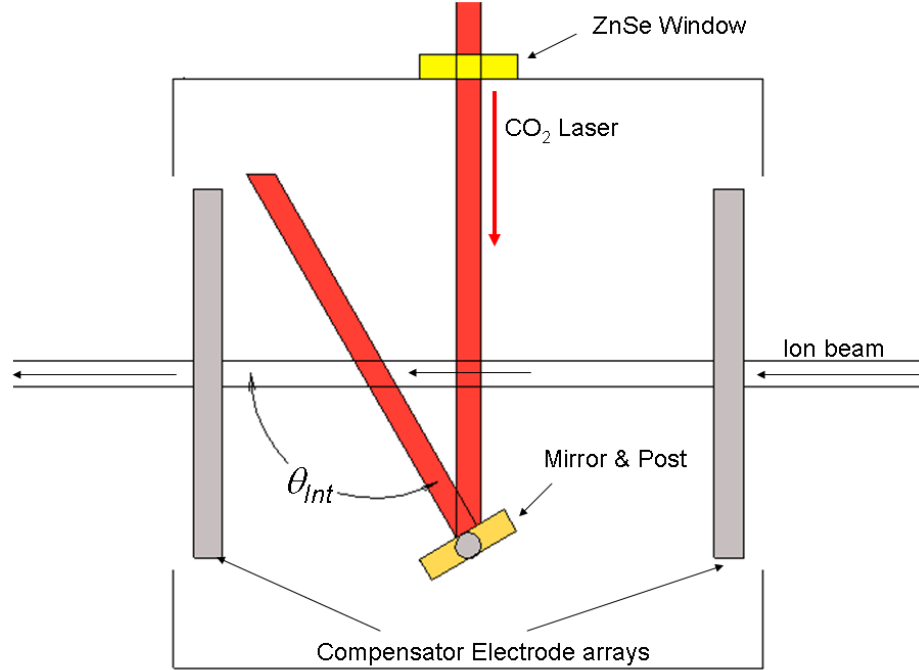


Figure 2.15: Schematic of the Laser Interaction Region (LIR). This diagram shows the construction and layout of the LIR as viewed from the top down. Not shown is the μ -metal shielding present inside the LIR.

As stated previously, and depicted in Fig. 2.15, by varying the angle at which the CO₂ laser intersects the ion beam the fixed frequencies of the CO₂ laser can be smoothly tuned over a range of frequencies exciting resonant transitions from specific high angular momentum Rydberg states into much higher Rydberg states. The laser frequency, as seen from the reference frame a Rydberg ion, ν'_L , is given by

$$\nu'_L = \frac{\nu_L}{\sqrt{1-\beta^2}} [1 + \beta \cos(\theta_{Int})]. \quad (2.8)$$

Calculation of the Doppler-tuned laser frequency relies upon knowledge of the velocity of the ion beam relative to the speed of light, β , the rest frequency of the laser, ν_L , and θ_{Int} . The velocity of the ion beam was determined by careful calibration of the accelerating potential as described earlier in this chapter. The intersection angle of the CO₂ laser with the ion beam is related to the angle recorded by the computer, θ_{Stage} , by an

offset, θ_{\perp} , the angle at which the CO₂ laser is reflected exactly perpendicular to the ion beam by

$$\theta_{Int} = 90^{\circ} - 2(\theta_{Stage} - \theta_{\perp}). \quad (2.9)$$

The calibration of the angle measured on the rotation stage at which the CO₂ laser is perpendicular to the ion beam is a critical in determining the Doppler tuned frequency of the CO₂ laser. The Doppler tuned laser frequency in turn determines the fine structure energy. As a result of the importance in determining the fine structure energies of the Rydberg fine structure spectra studied in this work it is important that the value of θ_{\perp} is known accurately. An error in the determination of θ_{\perp} of 0.05° can lead to an error in the determined fine structure energy of approximately 45 MHz or more depending upon the velocity of ion beam being studied. The calibration of θ_{\perp} is described in Chapter 3.

Since the velocity of the ion beam is known precisely due to careful calibration of the accelerating potential and θ_{\perp} is known, a spectrum with respect to the energy difference between the hydrogenic frequency of a particular Rydberg transition and the Doppler-tuned CO₂ laser frequency can be generated by slowly varying the intersection angle. A single resolved RESIS transition is shown in Fig. 2.16 below to illustrate this. For each point the angle of intersection of the CO₂ laser with the ion beam was adjusted by 0.10°.

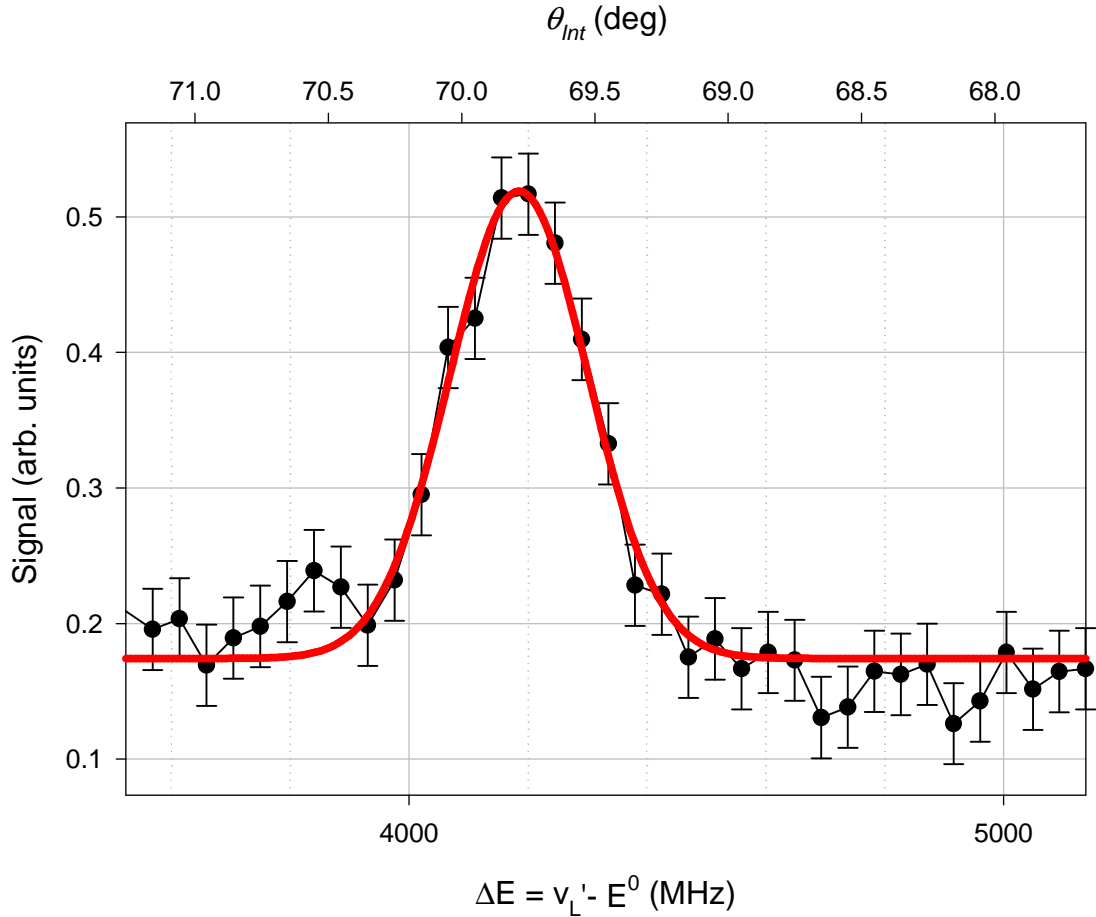


Figure 2.16: Th^{3+} (37, 8) – (73, 9) resolved transition. The bottom x-axis is the difference between the CO_2 laser's Doppler-tuned frequency and the hydrogenic transition frequency between the $n = 37$ and $n' = 73$ Rydberg levels in Th^{3+} and the top x-axis is the intersection angle made between the Doppler tuned CO_2 laser and the ion beam.

The sources of width of the resolved RESIS transitions, such as the one shown above in Fig. 2.16, can combine the homogenous widths arising from individual atom and inhomogeneous width arising from the differences between atoms. Sources of inhomogeneous width include the width due to the angular and velocity spread of the ion beam. Since there are two different tuning magnets used, if the velocity of the ion beam is significantly different over the profile of the ion beam this would be manifested as an increased angular divergence of the ion beam. The angular divergence of the beam was estimated earlier in this chapter to be approximately 0.25° at maximum; this is most likely

an over-estimate of the divergence of the ion beam. The width in frequency due to the maximum angular spread in the beam can be determined by differentiation of Eq. (2.8),

$$\Delta v_{\theta \text{ spread}} = v_L \cdot \beta \cdot \Delta \Theta \cdot \sin(\theta_{int}). \quad (2.10)$$

For typical beam velocities relative to c of 0.001 and intersection angles of 70° , the width of the transition due to the angular spread of the beam is 113 MHz. The width of the resolved RESIS transition due to the velocity spread, $\Delta(c\beta) = 0.02\% \cdot \beta$, of the beam can be determined by

$$\Delta v_{v \text{ spread}} = v_L \frac{\Delta(c\beta)}{c} \left| \cos(\theta_{int}) \right| \quad (2.11)$$

For the typical beam velocities and intersection angles studied in this work the width of the transition due to the velocity spread of the beam is 1.9 MHz. This source of width is then completely negligible.

However, the homogenous sources of width such as: the spectral width of the CO_2 laser, the natural linewidth of the transition, transit width due to the finite interaction time between the CO_2 laser and the ion beam, and Stark broadening effects on the transition also contribute to the total width of the resolved RESIS transition. Of these four possible homogenous sources of width the transit width and Stark broadening of the transition are dominant. The natural linewidth [29] of states typically explored in this work is approximately 0.08 MHz. The width of the transition due to the finite interaction time between the CO_2 laser and the ion beam can be calculated from

$$\Delta v_{Transit} \approx 0.375 \left(\frac{c\beta}{w_0} \right) \sin(\theta_{int}) \quad (2.12)$$

where $c\beta$ is the velocity of the ion beam in MKS units and w_0 is the waist of the laser. For a typical θ_{int} of 70° and beam velocity of 2.9×10^5 m/s for the Th^{4+} ion beam, the transit width is calculated to be 113 MHz.

The width due to Stark broadening of the transition by external electric and magnetic fields has typically been a limiting source of width in past studies using the RESIS technique. The stray magnetic field which could produce a motional electric field in the LIR was reduced to a negligible level by the inclusion of μ -metal shielding inside the LIR. The full width of the high- L RESIS transition due to the linear Stark effect, Δv_{Stark} , can be estimated as half the separation between the two extreme Stark eigenstates [15,28] and is given by

$$\Delta E(a.u.) = \frac{3n(n-1)}{2Q} F, \quad (2.13)$$

where F is the magnitude of the field in atomic units and Q is the charge of the ion core. Efforts to reduce the stray electric field due to contact potentials were made in by careful consideration of the materials used in the construction of the LIR [15]. Despite the best efforts to minimize them, stray electric fields present within the LIR as large as 100 mV/cm were observed. Electric fields of this magnitude can result in a number of complications of the RESIS optical spectra as a result of Stark interactions between the different Rydberg levels. Chiefly among these issues is the rise of significant Stark induced broadening and shifts in the upper state energies of a resolved RESIS transition from the zero field position, which in turn complicates the analysis of the resulting fine structure observations. This is discussed further in Chapter 4.

By reducing the stray electric field in the LIR it was believed that any semi-resolved RESIS transitions on the side of the high- L transition would become nearly fully resolved

due to the reduction in the unresolved- L transition's line width. Also a reduction in the stray electric field present would reduce the Stark induced shifts of the upper state energies, eliminating a potential additional complication in the analysis of the fine structure observations. A device was constructed to reduce the stray electric field present in the LIR by allowing for the creation of an opposing field with arbitrary x , y , and z components. This device is detailed in Chapter 3.

2.5 RESIS detector

The Rydberg ion beam then passes into the RESIS detector region after exiting the LIR. The detector region consists of two 10" diameter con-flat tubes that have a total length of 28". Contained within the stainless steel tubes is a series of electrodes that make up the Stark ionizer, deflection plates that are used to direct the ion beams onto the Channel electron multiplier, and a beam imaging system. The detector region used in this work is similar to the region described in detail in Daniel Fisher's dissertation [15]. The difference between the detector region described in Daniel Fisher's dissertation and the detector region used in this work is the inclusion of two additional modifications. These modifications are described in detail in Chapter 3. The basic operation of the detector will be described in this section. A general overview schematic of the initial detector assembly used for this work is shown in Figure 2.17. The beam enters on the left hand side of the image through a 6 mm aperture. The ion beam then passed through the Stark ionizer, the operation of which is described below.

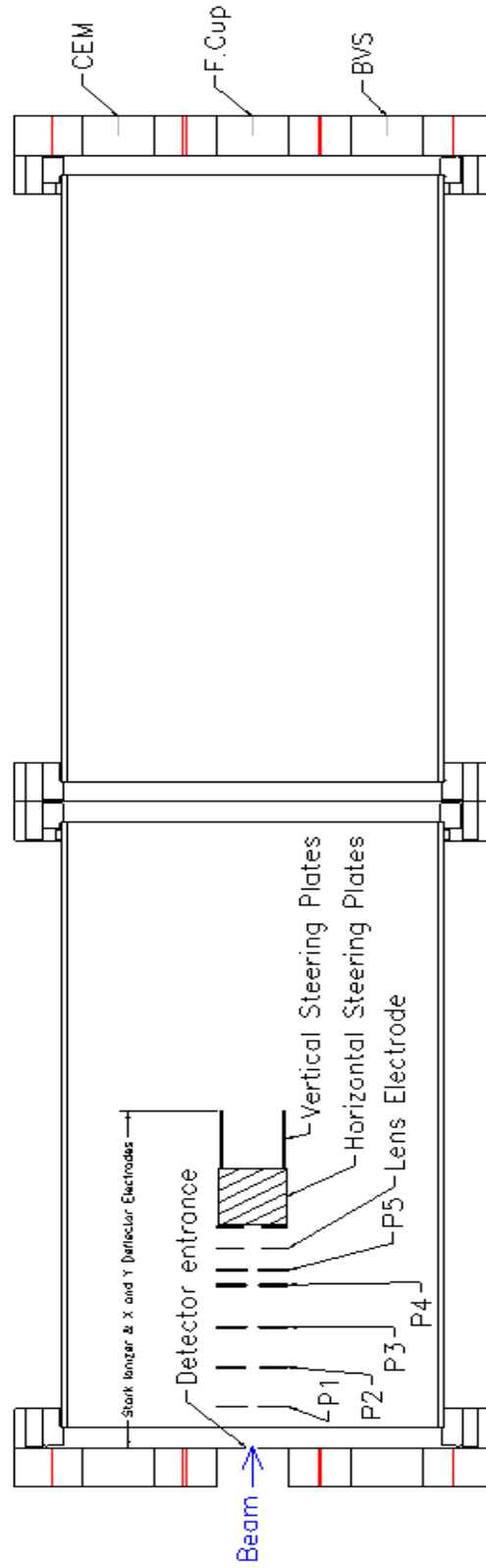


Figure 2.17: CAD schematic of the original detector region. This view is a vertical slice through the detector region showing the detector in the initial configuration. The beam, indicated by the blue arrow, enters the detector through a 6 mm diameter aperture. The electrodes, indicated P1 through P5 form the Stark Ionizer and have aperture diameters of 6.4 mm [15]. There is a 3 mm diameter aperture in front of the entrance to the CEM. The CEM, Beam Viewing System (BVS), and Faraday Cup (F.Cup) were attached to the 2 3/4" CF ports as indicated in the figure.

The ions formed in the Stark ionizer and any remaining ions are then deflected by a pair of steering electrodes into the detection electronics located at the end of the detector as indicated. The CEM was attached on the top port located 2.9" above the horizontal, the beam imaging system was located in the lower port, and a Faraday cup is used to monitor the ion beam current was mounted on the middle port.

The purpose of the detector is to detect Rydberg states that were resonantly excited by the CO₂ laser in the LIR. To accomplish this, the ions that are excited by the CO₂ laser are ionized by the Stark Ionizer, energy tagged to differentiate these ions from ions of similar charge formed by other processes, deflected vertically to differentiate these ions by charge from ions that had not been ionized in the Stark ionizer, and collected on a CEM. A closer view of the of the Stark Ionizer electrode arrangement is shown in Fig. 2.18.

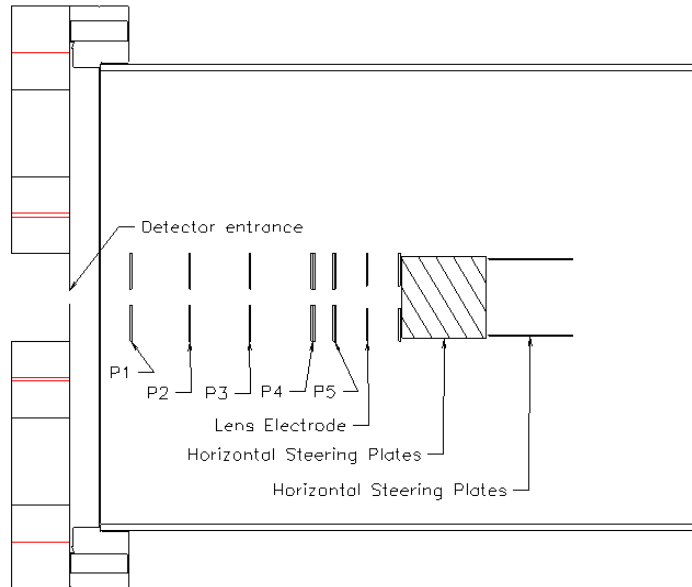


Figure 2.18: Detailed picture of the Stark Ionizer electrodes. The electrodes labeled P1, P2, P3, and P4 are all spaced by 2.5 cm [15]. Connections to the P1, P2, P3, and P4 electrodes exist to the outside of the vacuum chamber and are made using 5 kV SHV connections. The P5 electrode is grounded internally. There are also external connections for the vertical and horizontal steering plates that are used to deflect the ion beam and the lens electrode that may be used to focus the beam.

For this work the Rydberg ions that were highly excited by the CO₂ laser enter the detector region and are ionized by an electric field produced by applying a potential to the P3 electrode in the Stark Ionizer. The Stark ionizer was set up in what is known as that “Long Gap Stripper” configuration. In this configuration a potential, V_{LGS} , is applied to the P3 electrode, a potential of $2/3V_{LGS}$ is applied to the P2 electrode, and $1/3V_{LGS}$ is applied to the P1 electrodes. The P4 electrode is then grounded. The electrodes can also be energized in an alternate “Short Gap” stripper arrangement to achieve higher ionizing fields if necessary. This alternate arrangement is detailed in Fisher’s dissertation [15]. The separation between adjacent electrodes is 2.5 cm, implying that a potential of 1000 V on the P3 electrode results in a 400 V/cm field in the long gap stripper.

The electric field in the Stark ionizer is tuned such that it Stark ionizes all Stark states with a particular principle quantum number n in the region between the P3 and P4 electrodes. For ions entering an electric field diabatically the lowest energy Stark states ionize at a field approximately given by

$$F(\text{a.u.}) = \frac{1}{9} \frac{q^3}{n^4}, \quad (2.14)$$

where F is the field in atomic units. The highest energy Stark states ionize in a field given approximately by

$$F(\text{a.u.}) = \frac{2}{9} \frac{q^3}{n^4}. \quad (2.15)$$

It was shown by D. Fisher [15] that the field suggested by Eq. (2.14) nearly maximized the size of the RESIS excitation signal. The field in the Stark ionizer was tuned by applying potentials to the P1, P2, and P3 electrodes to nearly match the field recommended by Eq. (2.14) in the gap between the P3 and P4 electrodes in order to be

certain that all of the Rydberg ions excited by the CO₂ laser were being ionized and collected. The field prior to the P3 electrode is a factor of three smaller, and it should not ionize any of the n -states.

A schematic of the potential applied in the Stark ionizer electrodes used in this work and the resulting electric field is shown in Fig. 2.19 to illustrate the operation of the Stark ionizer and resulting energy change of the ions formed by Stark ionization. The ions enter from the left side of the figure and pass to the right. At first the ions enter a region of electric field that is a third of the field required to ionize the levels of interest. This field is below the lower limit for ionization of Rydberg states with a particular n , given by Eq. (2.13). Once the ions pass the P3 electrode the field rapidly changes, becoming three times stronger; strong enough to ionize all the Rydberg states with a given n . In this way all the ions of principle quantum number n_2 , excited by the CO₂ laser, diabatically ionize in the stripper and experience a change in kinetic energy given by

$\Delta KE = \Delta q \cdot V_{Stripper}$, where Δq is the change in the charge of the ion as a result of ionization in the Stark ionizer.

As mentioned previously, the ions formed by Stark ionization are then directed into a CEM at the end of the beam line by a set of horizontal and vertical electrostatic deflection plates. The horizontal plates apply a small deflection in the horizontal plane to finely steer the ion beams into the CEM or BVS. The dominant deflection is in the vertical direction into the CEM. The vertical deflection of the ion beam is proportional to the charge and inversely proportional to the kinetic energy of the ion beam. In this way the ion beams are separated in the vertical plane of the detector by charge and energy. The ions formed by Stark ionization in the field between the P3 and P4 electrodes are tagged

by an increase, or decrease, in kinetic energy and separated from other ions of the same charge and mass. Since, due to pre-ionization, there should be no Rydberg states in the beam able to be ionized at this field, unless excited by the CO₂ laser, this technique should be background free.

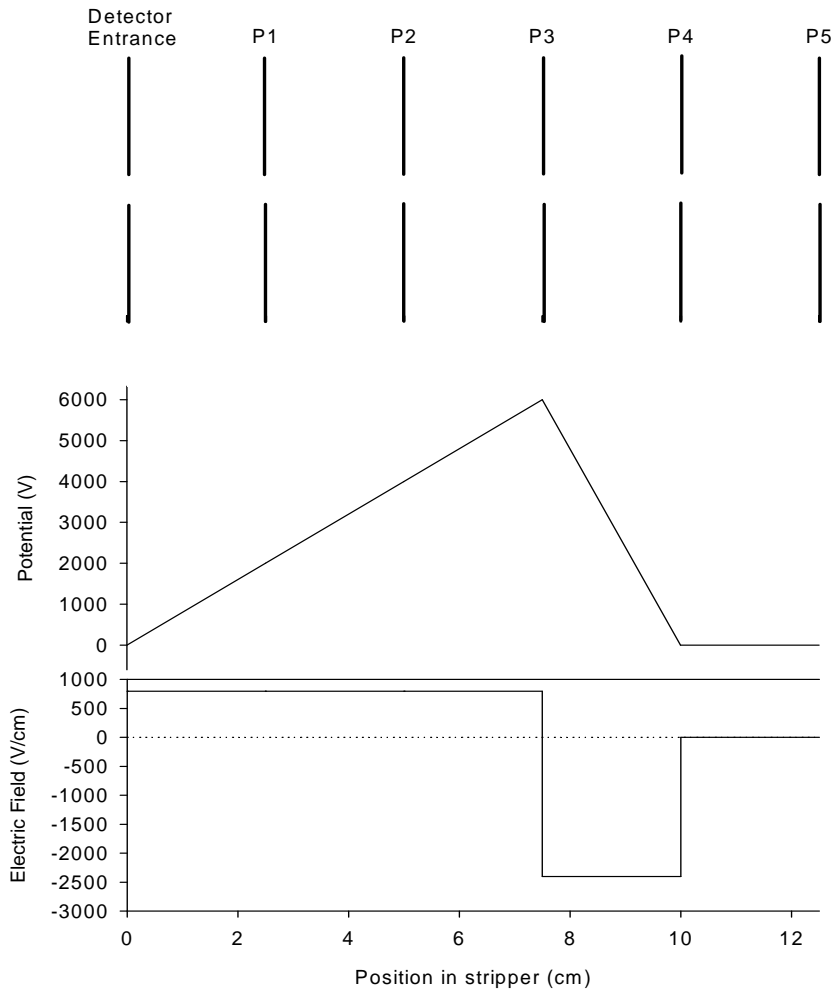


Figure 2.19: Schematic of the potential (middle) and electric field (bottom) in the Stark Ionizer that was used in this work to ionize the $n = 73$ levels in Th^{3+} . The field between the P3 and P4 electrodes is three times the field in the region of the stripper between the entrance and the P3 electrode. When the ions are stripped of a highly excited Rydberg electron by the stronger field in this region their kinetic energy is increased by 6 keV, in this case.

Chapter 3: Apparatus Evaluation Data

Described in this chapter are four devices that were constructed to improve the experimental apparatus and the calibration of the perpendicular intersection angle of the CO₂ laser. Since each of the sections presented in this chapter are separate, an outline of the chapter is provided below.

- Section 3.1 describes the theory of enhancing the potentially resolvable lower L Rydberg populations by Stark regeneration in a focusing element. This section also provides data evaluating the effect of the re-mixer lens on the size of the resolved RESIS transitions with respect to the high- L signal. A small enhancement is observed.
- Section 3.2 describes the reduction of the stray electric field in the LIR through the use of a device constructed during the course of this work. This section also presents data evaluating the effectiveness of this device in compensating for the stray electric field. Studies of the excitation linewidth yield estimates of the limiting sources of linewidth.
- Section 3.3 provides details of the calibration procedure used to determine the perpendicular intersection angle of the CO₂ laser with the ion beam.
- Section 3.4 describes the modifications to the RESIS detector that were developed in an attempt to reduce the background, which is the dominant source of noise in the experiment. Data accumulated clarifies the source of the background, a fundamental limitation in this experiment.

3.1 RESIS transition enhancement

After the 15° magnet are two einzel lenses. The objective of the second of these lenses, which is located just before the Laser Interaction Region (LIR), is to repopulate the shorter lived lower L Rydberg states that could be resolved by the RESIS technique by exchanging population with the longer lived higher L Rydberg states. The Rydberg states studied in this work have an approximate lifetime obtained from the transition rate of the free decay of a state. This transition rate for a state with a given Q , n , and L can be estimated using the formula developed by Chang [30] for hydrogen-like states:

$$A(Q, n, L) = \frac{1.08 \times 10^{10} Q^4}{n^3 (L + 0.5)^2} \text{ s}^{-1}. \quad (3.1)$$

For a typical $n = 37$, $L = 9$ state that was resolved in the Th^{4+} experiment Eq. (3.1) estimates a lifetime of 1.7 μs . The transit time between the Rydberg target and the LIR was approximately 3.0 μs . This implies that only ~17% of the initial population in the (37, 9) state is left to be excited by the CO_2 laser. The very high L (37, 36) state in Th^{3+} has a lifetime of 24.4 μs , implying that ~88% of the initial population is still present at the LIR. Since the $L = 9$ state was very well resolved by the RESIS technique in this work it would be beneficial then to repopulate of the $L = 9$ state with populations taken from higher longer lived states to enhance the signal size.

The mechanism of repopulating the shorter lived lower L states with some of the population of the longer lived higher L states to enhance the RESIS signal is referred to as Stark regeneration. It is based on a combination of adiabatic and diabatic changes to electric field. The limit determining if the changes in the electric field are either adiabatic or diabatic with respect to a certain state arises from the adiabatic theorem. The adiabatic

theorem states that if a system begins in an eigenstate and if the electric or magnetic field is varied slowly then the system will remain in the eigenstate that evolves continuously from the initial state [31]. The critical time scale is:

$$\Delta t_{crit} \cong \frac{\hbar}{\Delta E}, \quad (3.2)$$

where ΔE is the energy separation between adjacent eigenstates. If the Rydberg ions enter the electric field in the re-mixing lens adiabatically, meaning that the time that is required for the magnitude of the electric field to become large enough to Stark mix a particular (n, L) level into the Stark manifold is much longer than Δt_{crit} , the state will evolve adiabatically into a Stark eigenstate. Then, if the electric field changes polarity faster than Δt_{crit} the transition will be diabatic and the Stark energy of the state will be reversed. Finally if the electric field is reduced to zero adiabatically the lower L levels will be regenerated.

The conditions that must be met then for Stark regeneration of a particular lower L state to occur are given by:

$$\Delta t_{mix} \gg \frac{\hbar}{\Delta E} = \Delta t_{crit} \quad (3.3a)$$

and

$$\Delta t_{switch} \ll \frac{\hbar}{\Delta E} = \Delta t_{crit} \quad (3.3b)$$

where Δt_{mix} is the time required for the field to change from a zero field to a field sufficient to mix the (n, L) level into the Stark manifold, Δt_{switch} is the time over which the polarity of the electric field is changed, and ΔE is the zero field energy deviation from

hydrogenic of a particular (n, L) state. The field required to Stark mix a (n, L) Rydberg state is given by Eq. (2.11),

$$\Delta E(a.u.) = \frac{3n(n-1)}{2Q} F_{mix} . \quad (2.11)$$

In this application of Eq. (2.11) ΔE is the energy deviation of a particular (n, L) state from the hydrogenic energy. In the case of the $(37, 9)$ state in Th^{3+} : $\Delta t_{crit} \approx 0.07$ ns and $F_{mix} = 3.6$ V/cm.

The Stark regeneration technique can be understood more clearly with the aid of Fig. 3.1. Figure 3.1 is an example of the Stark eigenstates as a function of electric field for the $n = 5$ states in hydrogen. The actual states of this study, *e.g.* the $n = 37$ levels in Th^{3+} , are much more complicated but analogous. Let us assume that the lifetime of the states in Fig. 3.1 depends upon Eq. (3.1), ignoring the fact that the P-state lifetime is shorter than the S-state lifetime in Hydrogen. Let us also assume that the states are equally populated initially and allowed to decay so the population in the lower L states, $L = 0, 1,$ and 2 , is negligible while there is a significant population remaining in the $L = 3$ and 4 levels. In zero electric field, $n, L,$ and m are all valid quantum numbers and the populations in the various states are isolated in their individual states. We then turn the electric field up in intensity to 200 V/cm slowly, allowing the states to evolve adiabatically into Stark eigenstates and with energies shown on the far right hand side of the figure. In an electric field L no longer becomes a valid quantum number, instead the electric quantum numbers n_1 and n_2 are used [28]. The electric quantum numbers are related to n and m by

$$n_1 + n_2 + m + 1 = n . \quad (3.4)$$

The quantity $n_1 - n_2$ can be used, in conjunction with m to describe the $(n_1 - n_2, m)$ Stark eigenstate. The population initially in the $L = 4, m = 0$ state that evolves into the $(4, 0)$ Stark state is shown at (a) with a red square and the population initially in the $L = 3, m = 0$ state that evolves into the $(2, 0)$ Stark state is shown at (b) with a blue circle. Then the polarity of the electric field is changed rapidly, meaning that wave function remains unchanged as the electric field changes sign. This causes the populations that were in the $(4, 0)$ and $(3, 0)$ Stark states to be switched into the $(-4, 0)$ and $(-3, 0)$ Stark states, shown as the red square at (c) and blue circle at (d) in Fig. 3.1 respectively. The Stark eigenfunctions are distorted and therefore possess electric dipole moments. If the electric field changes sign rapidly then the sign of the Stark energy changes sign. The electric field is then reduced to zero slowly, allowing the populations which are now shown at (c) and (d) in Fig. 3.1 to evolve adiabatically into the $n = 5, L = 0$ and 1 states. In this way the populations of the shorter lived lower $L = 0$ and 1 states have been regenerated by the longer lived higher $L = 3$ and 4 states.

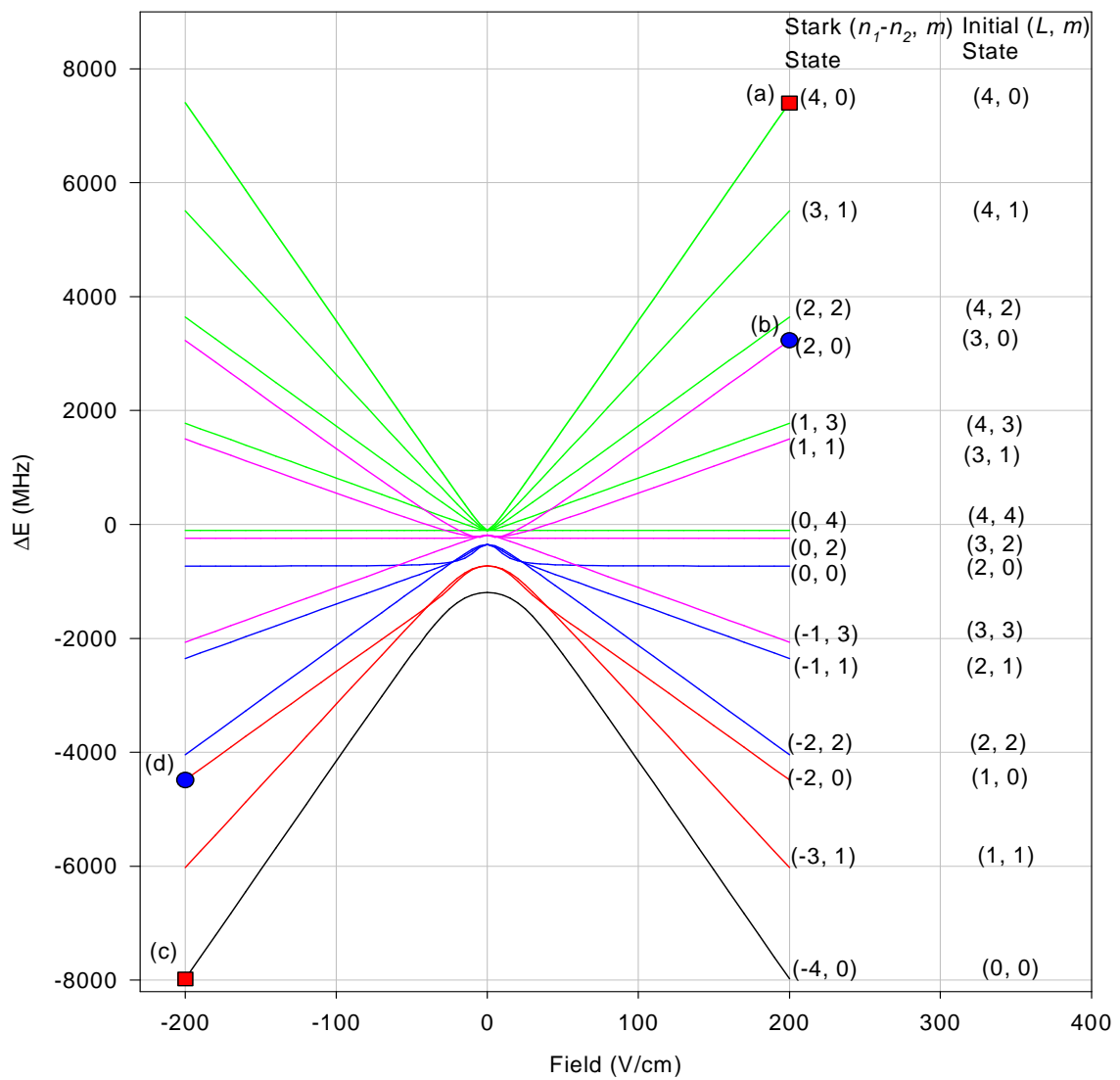


Figure 3.1: Graphical depiction of the $n = 4, L$ Stark levels in Hydrogen.

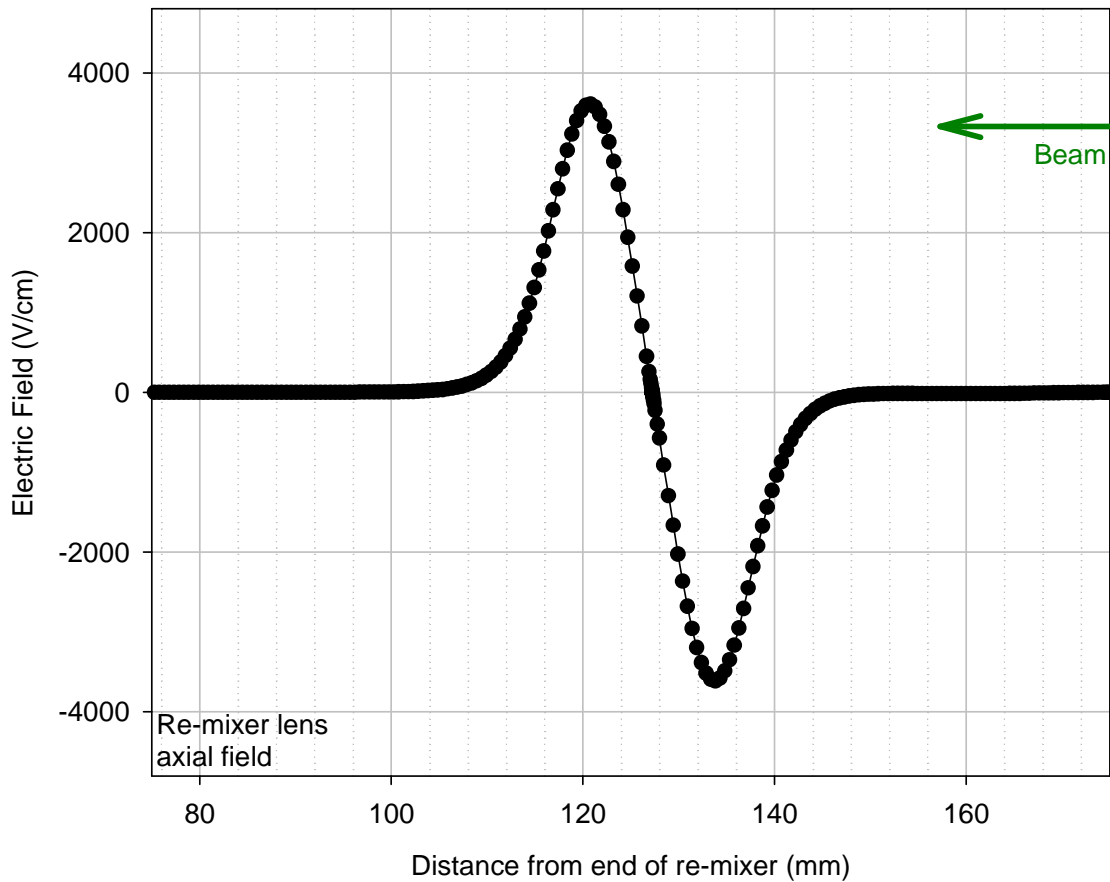


Figure 3.2: SIMION simulation of the longitudinal electric field through the center of the re-mixer. The beam enters from the right hand side of the page and passes to the left, as indicated by the green arrow.

Models of the electric field present in the re-mixing lens using SIMION were carried out for the typical potential of +4000 V that was applied to the re-mixer during the Th^{3+} observations. A plot of the axial electric field in the region of the re-mixer in SIMION is shown in Fig. 3.2. The magnitude of the transverse electric field as the ion passes through the re-mixer when the ions are slightly off the center axis must also be considered when determining if the condition for Stark regeneration has been met in the re-mixer. The transverse electric field as a function of distance from the center of the re-mixer lens

is shown in Fig. 3.3. The transverse field clearly becomes larger than the 3.6 V/cm required to completely Stark mix the (37, 9) state in Th^{3+} very rapidly as the distance from the center of the re-mixer is increased slightly. Figure 3.4 is a plot of the minimum electric field in the re-mixer as a function of radial distance.

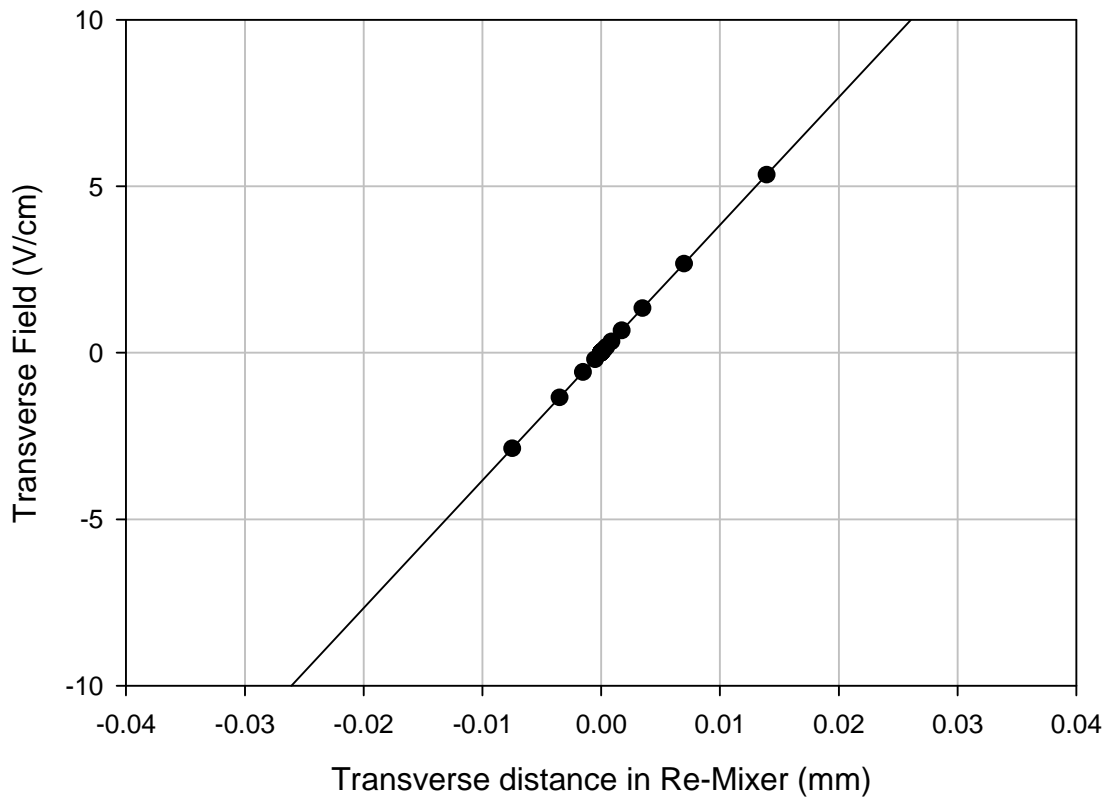


Figure 3.3: SIMION simulation of the transverse electric field in the re-mixer lens as a function of the radial distance. The transverse electric field becomes large enough to Stark mix the (37, 9) state at a very small distance (~ 0.01 mm) from the center of the re-mixer lens. The radius of the re-mixer lens is 6.3 mm.

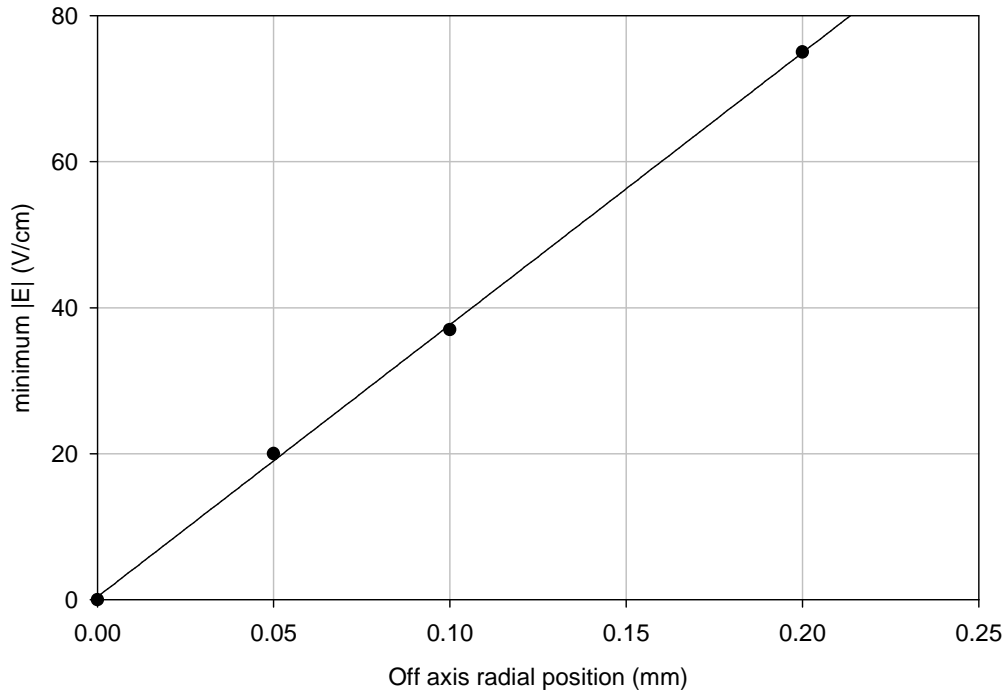


Figure 3.4: Calculated minimum electric field in the re-mixer as a function of the radial distance. The radius of the re-mixer lens is 6.3 mm.

The minimum electric field becomes greater than 3.6 V/cm at a radial distance of only 0.01 mm away from the center. The simulations of the electric field present in the re-mixer suggest that the field vector in the re-mixer rotates around from one direction to the opposite while the entire time, for a majority of the ion beam, the $(37, 9)$ state in Th^{3+} is Stark mixed. A small distance from the center of the re-mixer lens the field vector rotates about, changing polarity in the axial direction, in a length of 0.05 mm. In this situation $\Delta t_{\text{switch}} = 0.17$ ns. This indicates that the change in field polarity is neither slow enough to be adiabatic nor fast enough to be diabatic. The time required for the electric field produced by the re-mixer lens to become greater than the 3.6 V/cm required to Stark mix the $(37, 9)$ state in Th^{3+} is $\Delta t_{\text{mix}} = 15$ ns. This indicates that the ions in the beam enter the re-mixer lens adiabatically, pass through an electric field that changes polarity at an intermediate rate, and exit adiabatically. A similar analysis of the pre-ionizing lens

determines that $\Delta t_{switch} = 0.18$ ns and $\Delta t_{mix} = 46$ ns. This indicates similar behavior. If the ions pass through both lenses in this manner, some enhancement of the lower L signals might be expected.

Tests of the enhancement of the $L = 9$ level in Th^{3+} were conducted by examining the amplitude of a resolved RESIS transition compared with that of the high- L peak. A sample scan with the re-mixing lens on is shown in Fig. 3.5(a) and with the lens off in Fig. 3.5(b). Table 3.1 lists the results of comparing the ratio of the resolved RESIS transition to the high- L transition. An enhancement of the $L = 9$ signal by 29(7)% is observed.

A much simpler picture of the enhancement of a resolved RESIS transition starts with the assumption that the populations are scrambled across all the different L 's as the ions pass through the pre-ionizing lens, radiatively decay during the 11.43 cm between the two lens elements, and the populations are then scrambled again when passing through the re-mixer lens. The enhancement, EF , in the RESIS transition that is then predicted is:

$$EF = e^{\Delta t_{transit} / \tau(Q,n,L)} \quad (3.5)$$

where $\Delta t_{transit}$ is the transit time between the two lenses and $\tau(Q,n,L)$ is the radiative lifetime of the state. Using this simple model a maximum enhancement of the (37, 9) transition in Th^{3+} of 27% is expected. Measurements found that the re-mixer lens enhanced the (37, 9) – (73, 10) transition by 29(7) %. The maximum enhancement predicted in the simple model is surprisingly close to the ~29% enhancement observed, despite the conclusions that the fields in the re-mixer and pre-ionizing lenses do not change sign rapidly enough to implement diabatic switching.

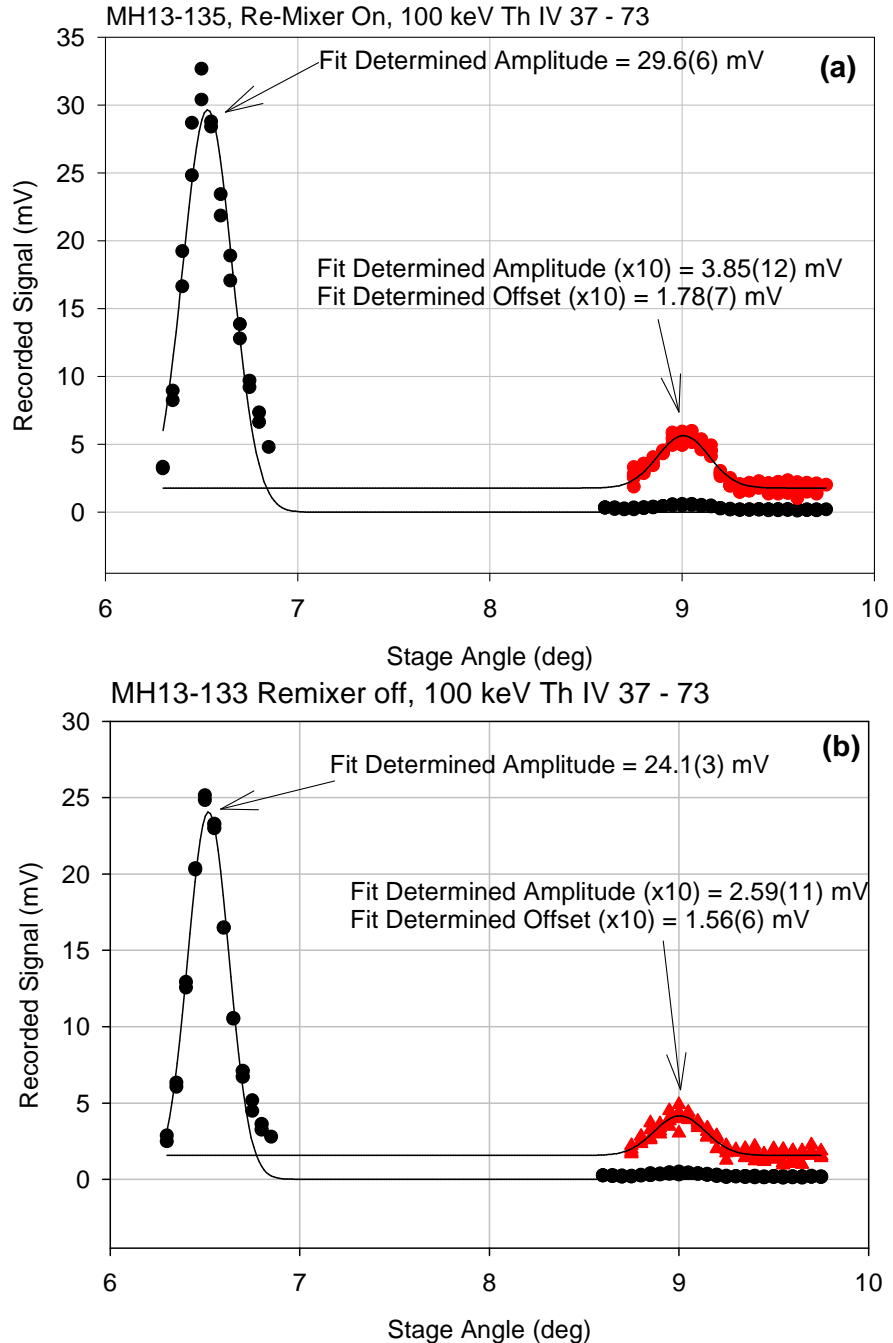


Figure 3.5: Th^{3+} (37, 9) – (73, 10) transition, (a) with the re-mixing lens on and (b) with the re-mixing lens off. The amplitude of the resolved peak on the right hand side of the graph was compared with that of the unresolved- L peak on the left hand side. This was taken to be a sort of normalization for when the re-mixing lens was turned off due to the additional focusing effects of the re-mixing lens on the beam. The unresolved- L peak was fit to a three parameter Gaussian, and is shown by the black points. The red triangles are the (37, 9) – (73, 10) transition multiplied by 10 for clarity and this peak was fit to a four parameter Gaussian since the offset in the observed signal amplitude is a larger fraction of the signal size in the resolved signal case.

Table 3.1: Measured ratios of the (37, 9) – (73, 10) transition in Th^{3+} to the high- L transition. The second column is the ratio of the high- L transitions to the resolved RESIS transition while the remixer lens was held at 4.0 kV. The fourth column is the same ratio observed with the remixer lens turned off.

Remixer lens on		Remixer lens off	
Run ID	$S(HL)/S(L=9)$	Run ID	$S(HL)/S(L=9)$
13-015	1.781(100)%	12-145	1.326(251)%
13-016	1.606(93)%	12-146	1.358(270)%
13-017	1.797(111)%	12-148	1.563(327)%
13-085	1.590(50)%	13-018	1.473(125)%
13-090	1.510(40)%	13-019	1.199(111)%
13-115	1.140(50)%	13-086	1.050(90)%
13-118	1.330(50)%	13-087	1.100(80)%
13-131	1.250(60)%	13-088	1.060(50)%
13-134	1.153(55)%	13-089	1.060(50)%
13-135	1.298(46)%	13-116	0.980(50)%
13-AVG	1.520(100)%	13-119	1.030(50)%
		13-133	1.076(48)%
Weighted Average	1.38(6)%	Weighted Average	1.07(3)%

3.2 Reduction of the Electric field in the LIR

The presence of a stray electric field in the LIR results in complications to the analysis of the resulting Rydberg fine structure due to Stark induced broadening of the transitions and shifting of the upper state energies. In the Kr^{6+} experiment there was an electric field approximately 100 mV/cm present. It was believed that the large field could be related to the large amount of residual primary Kr^{6+} beam propagating through the LIR. Thus, the addition of the 15° magnet would reduce the stray electric field by preventing the large residual primary beam from entering the LIR. Also, in Dan Fisher's dissertation the stray electric field present in the LIR was dealt with by applying a small bias potential to the mirror and post assembly inside the LIR.

The inclusion of the 15° magnet did not eliminate the stray electric fields present in the LIR. A stray field approximately 60 mV/cm was found to still be present. Applying a potential to the mirror and post assembly did not eliminate this stray electric field. Thus, to reduce the complications in the analysis due to the stray electric field, a device was constructed that came to be called the "compensator". The compensator was intended to apply a small electric field in an arbitrary direction in order to cancel the existing field within the LIR. The compensator consists of a series of eight electrodes arranged in two rings of four inserted within the LIR. Figure 3.6 shows the CAD drawing of the electrode ring assembly and retaining ring used to keep the electrodes in place inside the LIR.

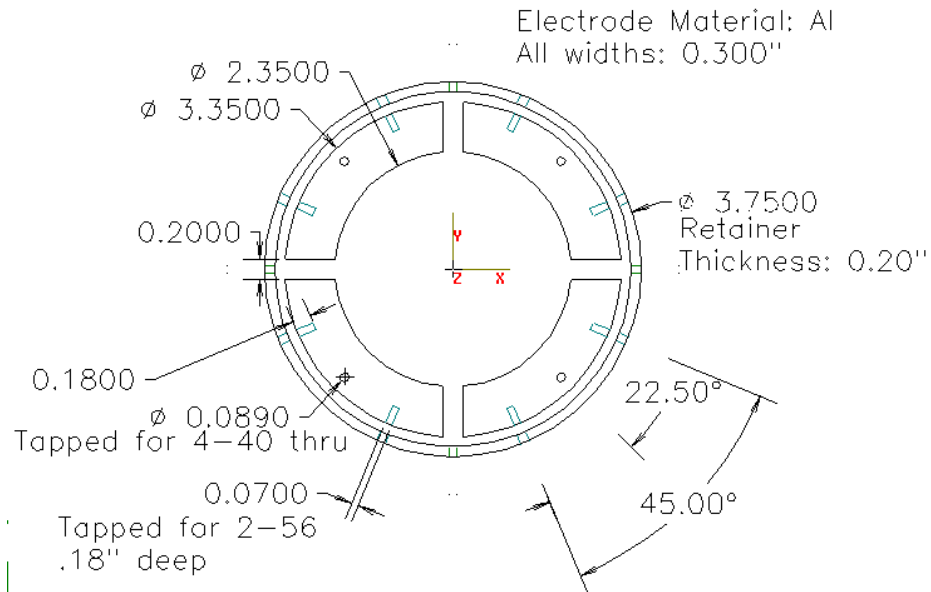


Figure 3.6: CAD drawings of the electrode rings of the electric field compensation device.

The small electrodes and the support ring used to mount the electrodes inside the LIR are made out of aluminum. The small electrodes are held to the outer ring by a pair of 4-40 nylon screws. The spacing between the electrodes and the outer support ring is determined by a 6-40 nylon nut slid over the mounting screw. The electrical connections between the electrodes forming the electric field compensation device and the electrical feed-through are made using a length of 24 gauge enameled magnet wire attached to the electrodes using a 6-32 screw. Figure 3.7 shows a photograph of the completed electrode assembly inside the LIR. The arrays are spaced by 5" inside the LIR. This spacing was chosen by the physical constraints inside the LIR and to keep the reflective surfaces of the electrodes as far away from the CO₂ laser beam as possible.

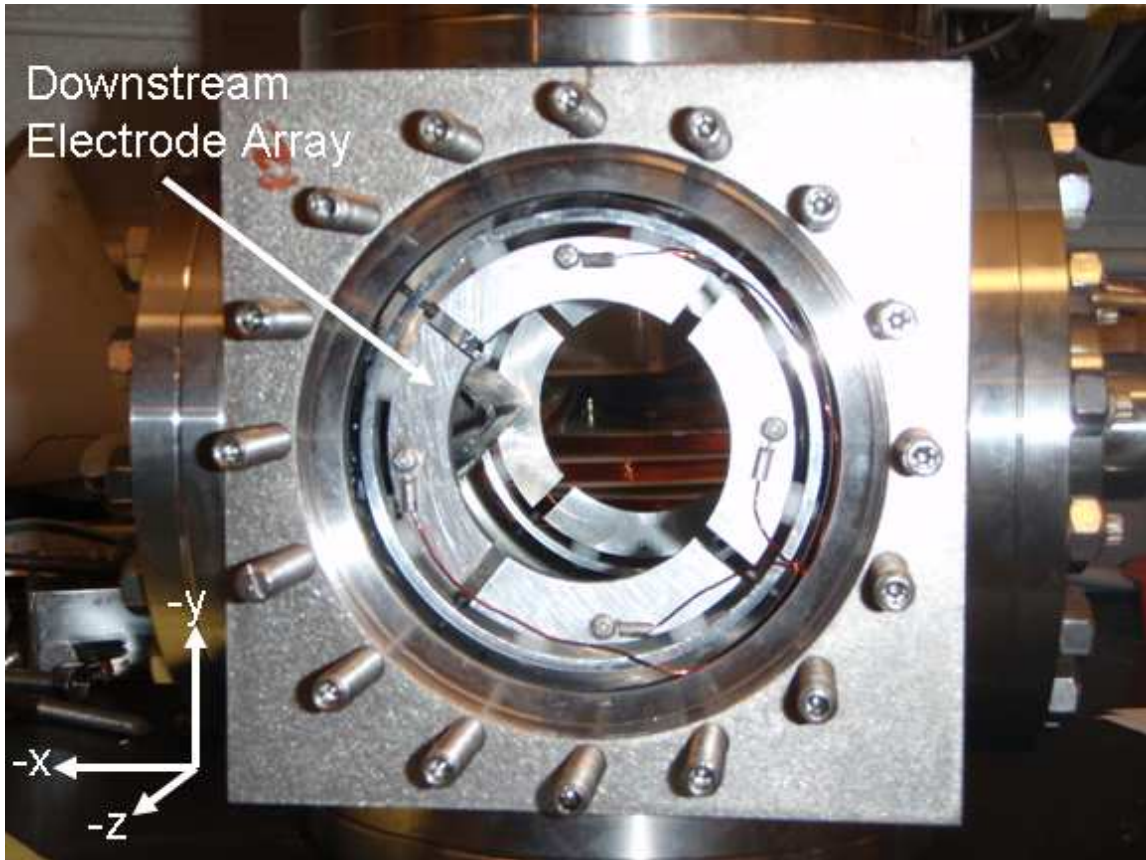


Figure 3.7: Completed electrode ring assembly of the compensator device. The axis shown in the bottom left of the figure corresponds with the axes of the compensator's control box. The z-axis is pointing out of the page. The nearest electrode arrangement in the photograph is referred to as the downstream array and the farthest arrangement on the opposite side of the LIR is referred to as the upstream array.

The compensator produces an electric field in the LIR by applying a small voltage to the array of electrodes. A voltage is applied to the electrodes in three principle axes, arranged in a right-handed coordinate system as defined in Fig. 3.7. The positive z-axis of the compensator is aligned anti-parallel to the direction of propagation of the ion beam. The y-axis is oriented towards the bottom of the RESIS apparatus and the x-axis of the compensator is oriented towards left as viewed from the ion beam. The arrangement of the axes of the compensator and electrode labels are shown in Fig. 3.8.

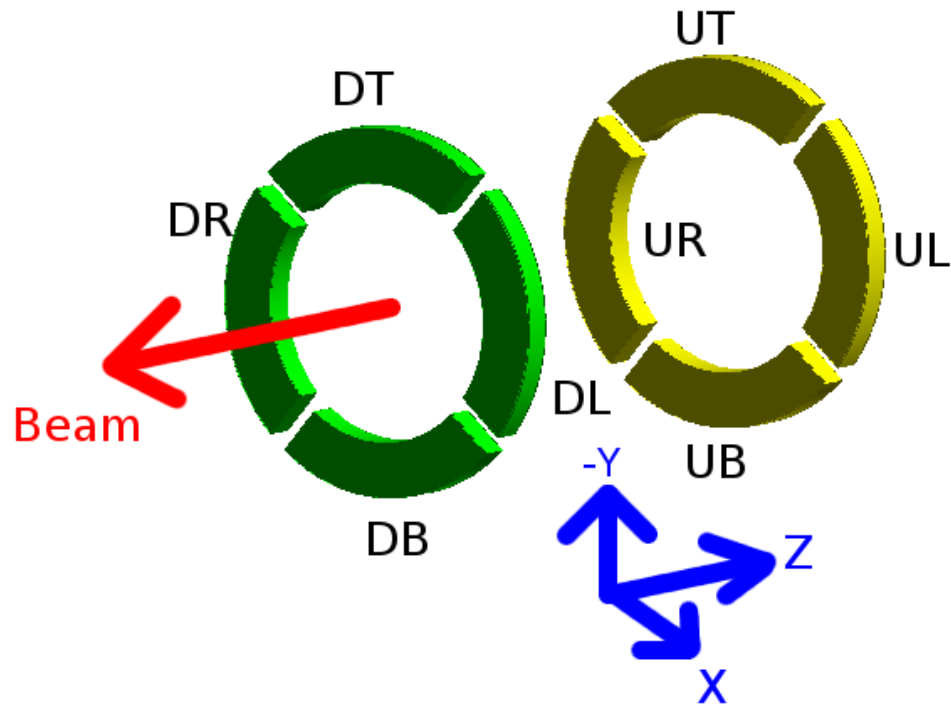


Figure 3.8: Graphical depiction of the arrangement of the axes of the compensator. The electrodes are labeled using two letters. The first letter designates Upstream and Downstream and the second letter designates the position: Top, Bottom, Left, and Right (e.g. UT for Upstream Top, DB for Downstream Bottom).

The control panel for the compensator consists of three different knobs that adjust the potentials applied to the electrodes. An electrical schematic of the control panel for the compensator is shown in Fig. 3.9. The arrangement of the electrodes as shown in Fig. 3.8 allows for a field to be oriented along the y and x-axes as shown by applying a balanced potential to top and bottom electrodes or the left and right electrodes. To produce an electric field along the z-axis the balance between the upstream and downstream sets of the electrode rings is adjusted. The control circuit shown in Fig. 3.9 also allows for any arbitrary combination of balanced potentials on the electrodes to create a field with arbitrary x, y, and z components.

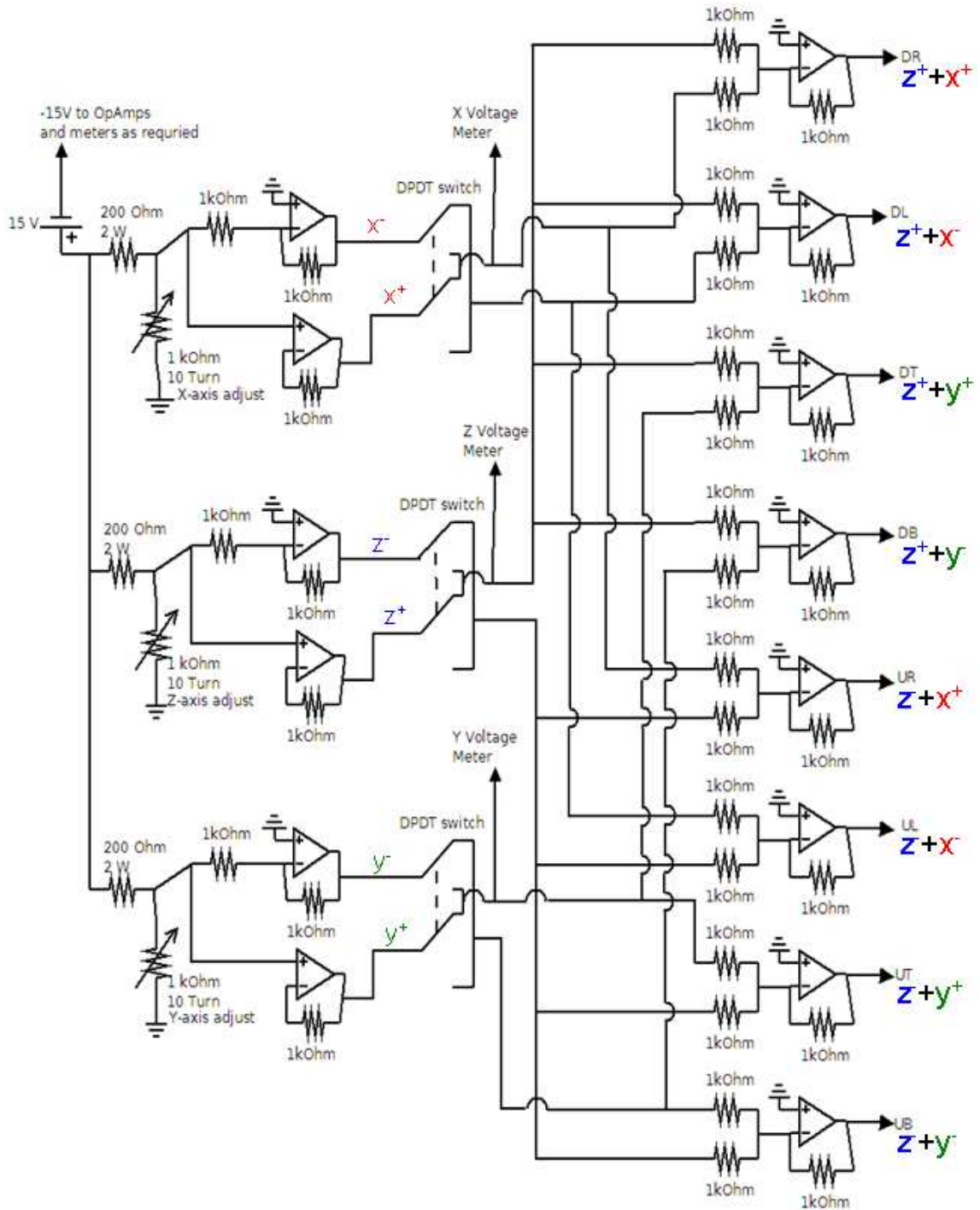


Figure 3.9: Compensator control electrical circuit. The two letter codes on the far right hand side of the diagram correspond to the electrode designations in Fig. 3.8. The color coded x, y, and z on the far right hand side of the figure correspond with the potentials applied to the electrodes for reference. The polarity of the potential is indicated by the superscripted + or – on the upper right.

A SIMION simulation of the compensator and LIR assembly was constructed to help understand the characteristics of the complete assembly. The uniformity of the electric field produced by the compensator electrodes can be characterized by applying a ± 1 V potential to the electrodes in the x, y, and z directions as well as applying a 1 V potential to the post and mirror assembly and examining the x, y, and z components of the resulting electric field.

Figure 3.10 is a series of plots of the x, y, and z components of the electric field through the center of the LIR and compensator assembly when a balanced potential of ± 1 V is applied to the x-axis electrodes of the compensator. From Fig. 3.10 it can be seen that the field mostly lies in the X-plane of the compensator and varies dramatically throughout the LIR. Figure 3.11 is the same series of plots except with ± 1 V is applied to the y-axis electrodes of the compensator. The same behavior in Fig. 3.11 is observed; the dominant field lies in the same plane as the energized electrodes and varies widely throughout the length of the LIR.

Figure 3.12 is another series of plots of the x, y, and z components of the electric field when a potential of ± 1 V is applied to the z-axis electrodes of the compensator. In this case a majority of the field lies along the z-axis, as expected; however, the variation throughout the LIR is much less than the previous cases. Instead of the field changing from ~ 0.17 V/cm at the edges to nearly zero at the center the electric field from the compensator is now much more uniform, only varying by $\sim 40\%$ from the maximum occurring near the electrode edges to the center of the LIR.

X, Y, and Z components of the electric field in the LIR when ± 1 V is applied to X-axis of the compensator

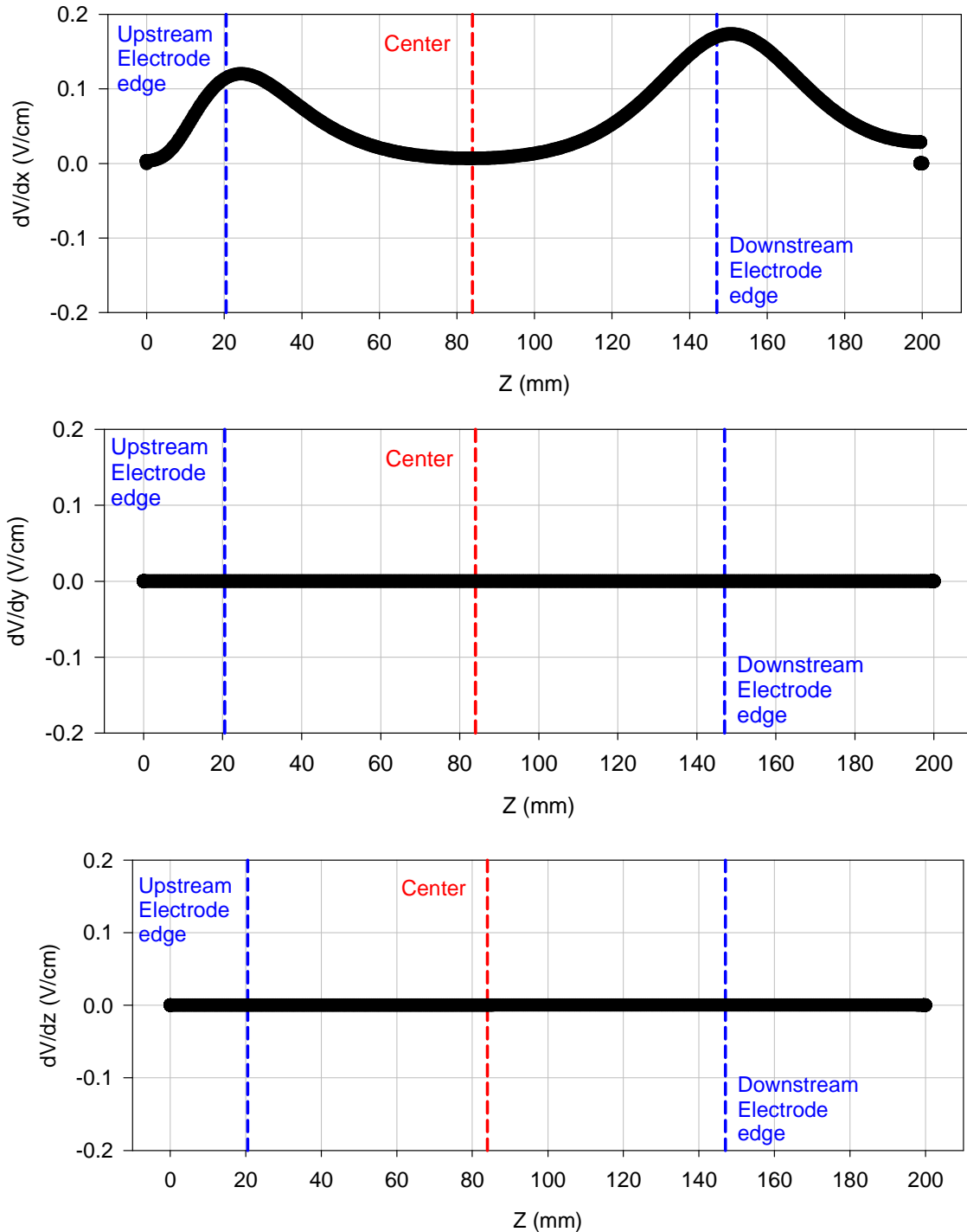


Figure 3.10: Plot of the x (top), y (middle), and z (bottom) components of the electric field when a potential of ± 1 V is applied to the x-axis electrodes of the compensator. For reference the center of the LIR is indicated with a red dashed line. The blue dashed lines on either side of the center line indicate the edges of the compensator electrodes. The x-axis is the position in the LIR. The beam enters at 0 mm and exits the LIR at 200 mm.

X, Y, and Z components of the electric field in the LIR when ± 1 V is applied to Y-axis of the compensator

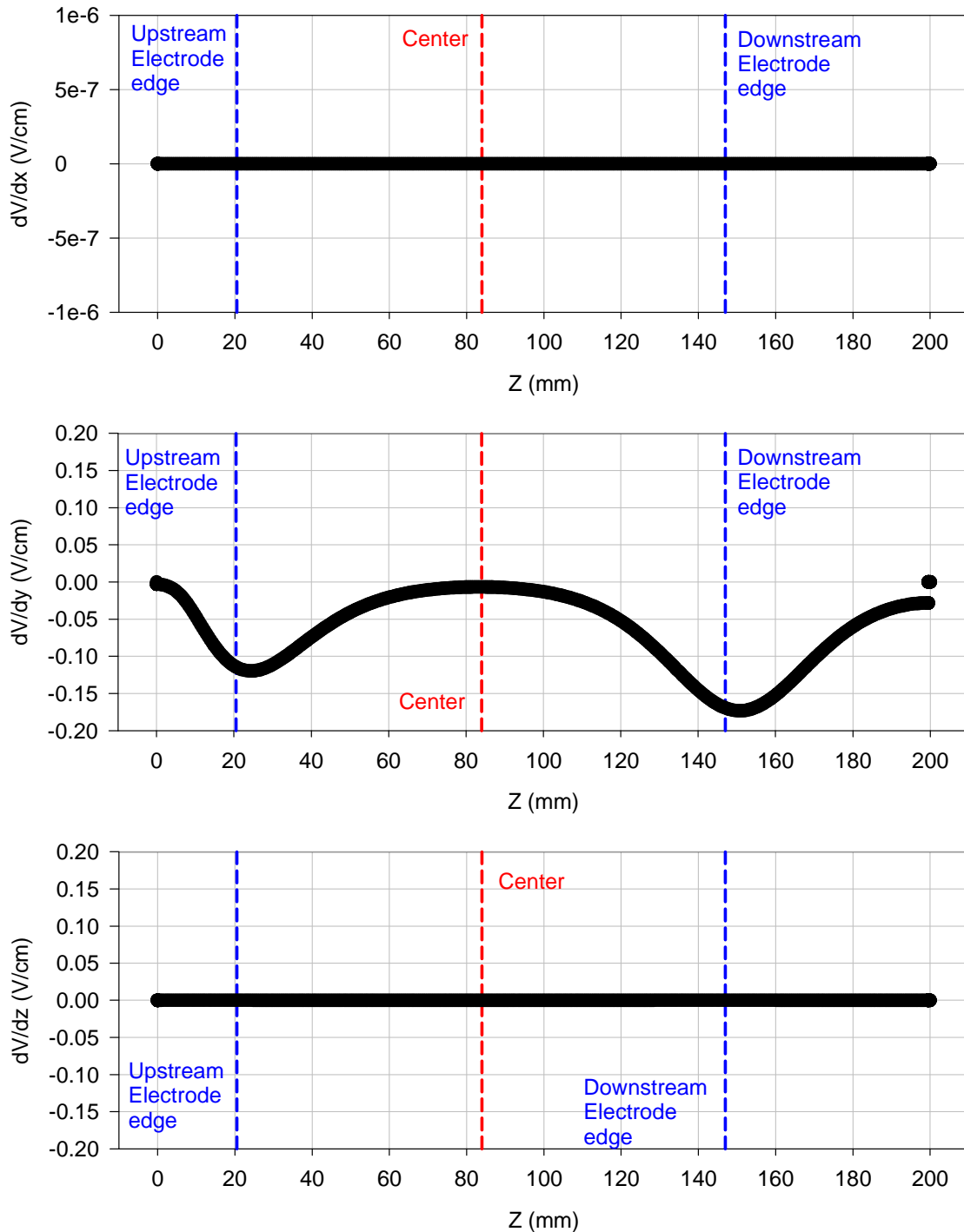


Figure 3.11: Plot of the x (top), y (middle), and z (bottom) components of the electric field when a potential of ± 1 V is applied to the y-axis electrodes of the compensator. For reference the center of the LIR is indicated with a red dashed line. The blue dashed lines on either side of the center line indicate the edges of the compensator electrodes. The x-axis is the position in the LIR. The beam enters at 0 mm and exits the LIR at 200 mm.

X, Y, and Z components of the electric field in the LIR when ± 1 V is applied to Z-axis of the compensator

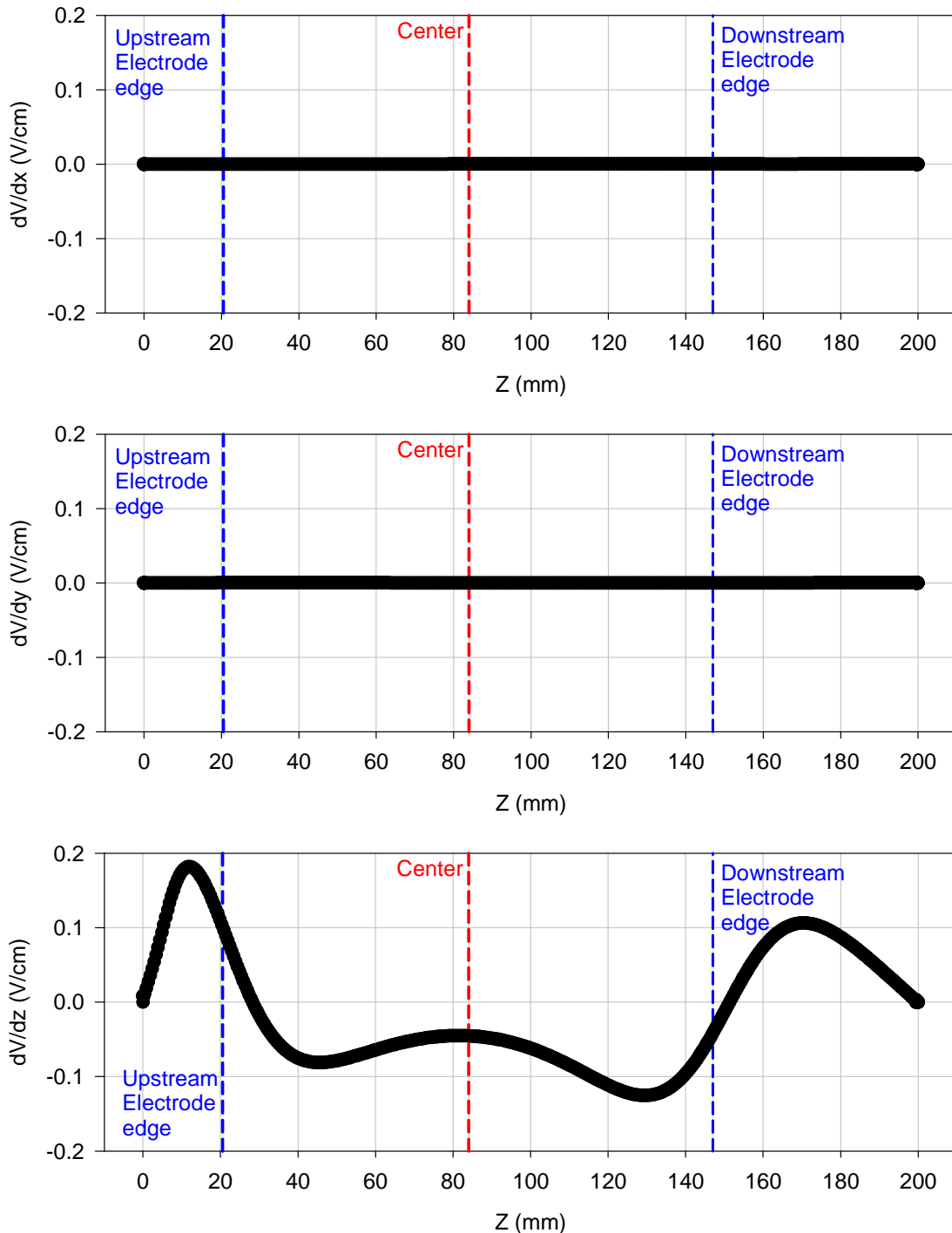


Figure 3.12: Plot of the x (top), y (middle), and z (bottom) components of the electric field when a potential of ± 1 V is applied to the z-axis electrodes of the compensator. For reference the center of the LIR is indicated with a red dashed line. The blue dashed lines on either side of the center line indicate the edges of the compensator electrodes. The x-axis is the position in the LIR. The beam enters at 0 mm and exits the LIR at 200 mm.

X, Y, and Z components of the electric field in the LIR when +1 V is applied to the mirror and post.

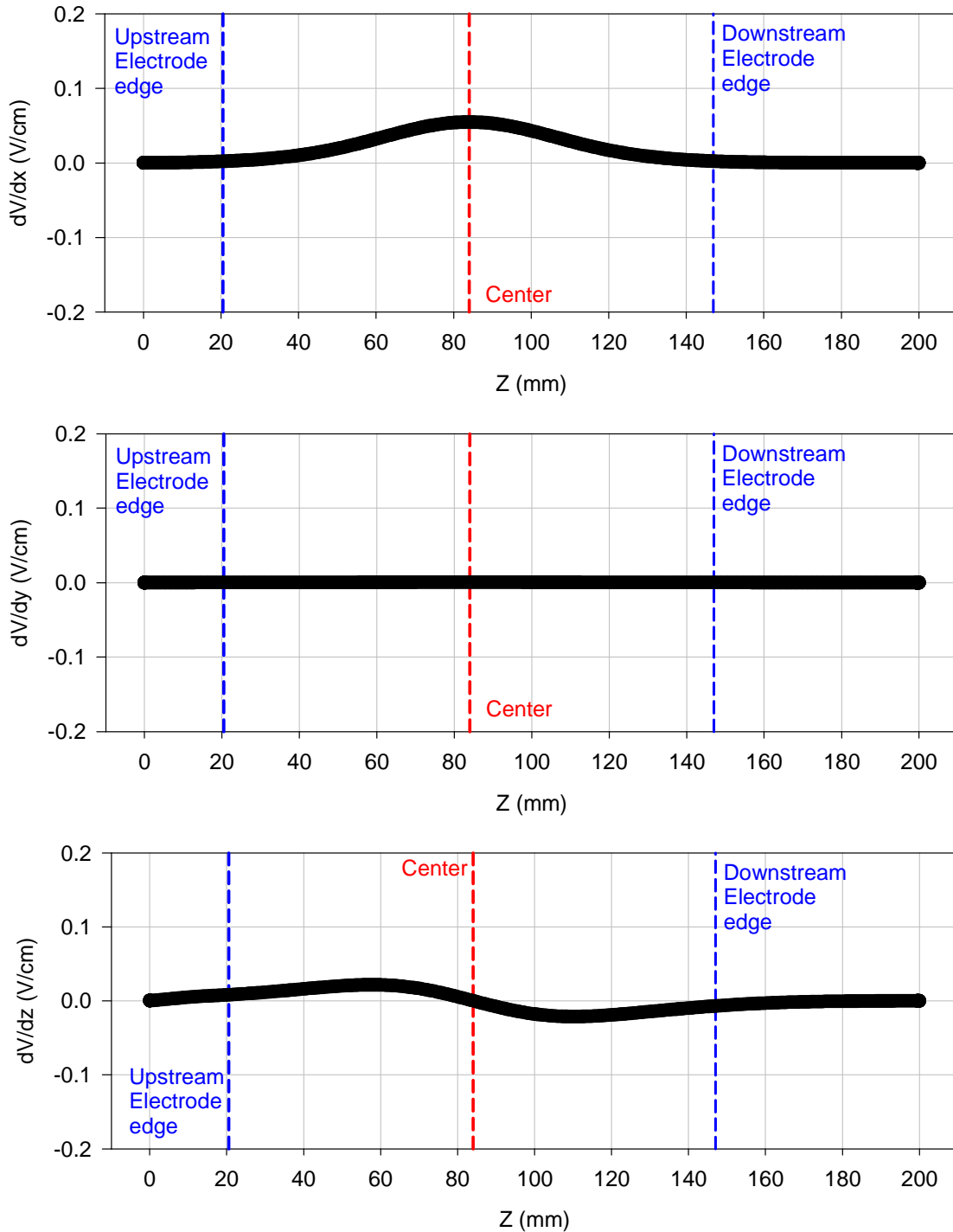


Figure 3.13: Plot of the x (top), y (middle), and z (bottom) components of the electric field when a potential of 1 V is applied to the mirror assembly inside the LIR. For reference the center of the LIR is indicated with a red dashed line. The blue dashed lines on either side of the center line indicate the edges of the compensator electrodes. The x-axis is the position in the LIR. The beam enters at 0 mm and exits the LIR at 200 mm.

Figure 3.13 is the final series of plots of the x, y, and z components of the electric field components throughout the center of the LIR when a potential of 1 V is applied to the mirror and post inside the LIR. In this case the field lies primarily in the XZ plane. The maximum magnitude of the electric field magnitude generated by the mirror is nearly a factor of three smaller than the maximum field generated by the compensator electrodes with the same potential applied.

What can also be seen from the figures is that the field produced by the X- and Y-axis of the compensator is very non-uniform. The field in these axes varies from a maximum magnitude of ~ 0.18 V/cm near the electrodes to nearly zero in the center. The field produced by the Z-axis of the compensator is much more uniform, only decreasing by a factor of ~ 2 in the center from the maximum electric field located near the electrodes. The field could be made more uniform by simply moving the electrode arrays closer together in the LIR. Improving the field uniformity would then come at the expense of usable Doppler tuning range in the LIR.

The compensator was constructed during a study of the Pb^+ Rydberg fine structure [23]. This was a convenient time to test the compensator using an ion beam with known resolved RESIS transitions. The study was carried out by examining the Rydberg spectrum of the $n = 20 - 83$ transition in Pb^+ . This transition was chosen because the $n' = 83$ upper state was approximately 2.5 times more sensitive to the effects of Stark broadening when compared with the $n' = 53$ upper state that was used in the study of the Pb^+ fine structure.

When the compensator was initially installed into the LIR a spectrum was observed with all of the compensator electrodes held at zero potential. The resulting spectrum is

shown in Figure 3.14(a). The first obvious thing to notice about this spectrum is that there are very complex line shapes occurring due to Stark mixing of the L 's in the $n' = 83$ upper state. An example of this mixing can be seen in the far right peak that is labeled $(20, 9) - 83$. The full width half maximum of the $(20, 9) - (83, 10)$ transition centered at ~ 1700 MHz is 434 MHz, suggesting a stray electric field of ~ 40 mV/cm. The full width half maximum of the high- L transition is 641 MHz.

The compensator was then activated by applying small potentials to the electrodes creating an opposing field with x-, y-, and z-axis components. The potentials applied to the electrodes were adjusted by initially observing the signal at $\Delta E = 0$ MHz. The signal at this location was minimized as much as possible. Once that was accomplished it was observed that there was what appeared to be some resolution between the unresolved- L and the $(20, 11) - (83, 12)$ transition at 550 MHz. The process of minimizing the signal at 550 MHz was then repeated and the potentials applied in the x, y, and z directions finely tuned. This procedure was considered completed when the resolved transitions could not be narrowed any further. At this point the field was believed to be minimized as much as possible and a final spectrum was taken, shown in Fig. 3.14(b), for comparison with the previous spectrum. In Fig. 3.14(b) the resolved transition on the far right is now Gaussian in shape and has a full width half maximum of only 170 MHz, or an angular full width half maximum of 0.39° . The width of the unresolved- L peak has been reduced to 271 MHz with the reduction in electric field.

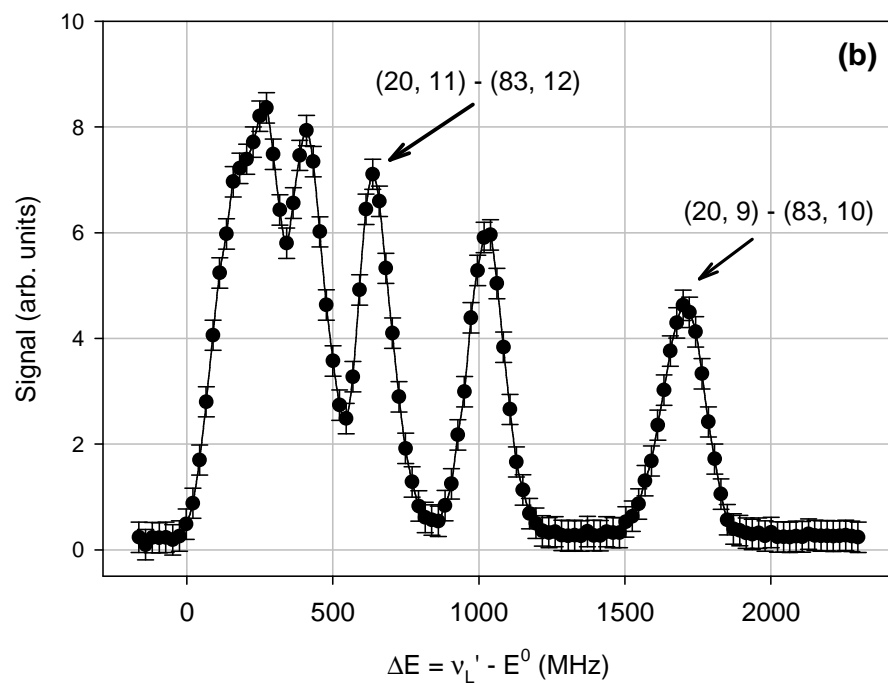
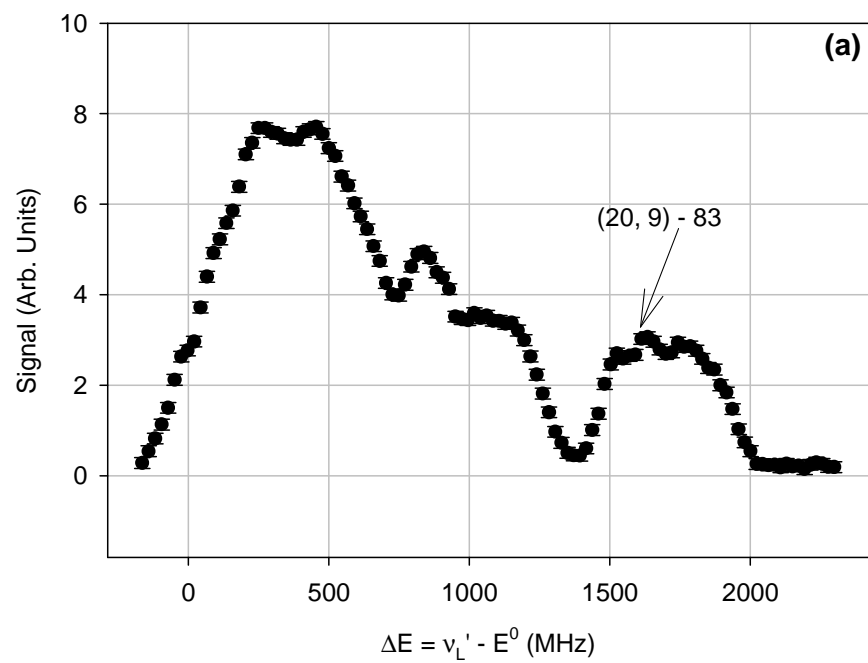


Figure 3.14: Comparison of the resolution of RESIS transitions in $20 - 83 \text{ Pb}^+$ with the compensator off (a) and then tuned to minimize the field (b). The plot in (a) is from scan #10-073 and the plot in (b) is from scan #10-074.

As discussed in the previous chapter, there are other sources of width besides Stark width that contribute to the width of the resonance such as widths due to the angular divergence of the ion beam, velocity spread of the beam, and from the finite transit time through the CO₂ laser. If the angular divergence of the beam is at a maximum 0.25°, as discussed in Chapter 2, then the contribution to the width from the angular spread of the beam is less than 109 MHz. The width contribution from the estimated 10 eV velocity spread of the beam is 3 MHz and the contribution to the width from the finite transit time through the CO₂ laser beam is 52 MHz. As discussed in Chapter 2, the total linewidth of the transition is the quadrature sum of the linewidth contributions from the individual sources of linewidth. In this case the resulting total linewidth is estimated to be 121 MHz at most.

An estimate of the electric field can be obtained by diagonalizing the Stark Hamiltonian. A program was adapted from existing Fortran code that simulates the composite line shape of the resolved RESIS transition once the zero field linewidth of the transition is known. Given a zero stray electric field linewidth of the transition of 121 MHz, the 434 MHz fitted FWHM of the peak in Fig 3.14(a) results in an estimate the electric field to be ~40 mV/cm. In Fig. 3.14(b) the 170 MHz linewidth results in an estimate of ~10 mV/cm for the stray electric field.

Since the source of the stray electric field is not understood, transitions on either side of θ_{\perp} were studied. The two transitions that were studied in Pb⁺ were the n = 20 to 83 and n = 20 to 84 transitions. The first transition was shown in Fig 3.14 before and after minimizing the stray electric field. The 20 – 84 transition is shown in Fig. 3.15 (a) before and (b) after adjusting the compensator to minimize the stray electric field. Table 3.2

lists the dial settings on the compensator control box that were used to minimize the line widths of a variety of transitions studied in the course of this work.

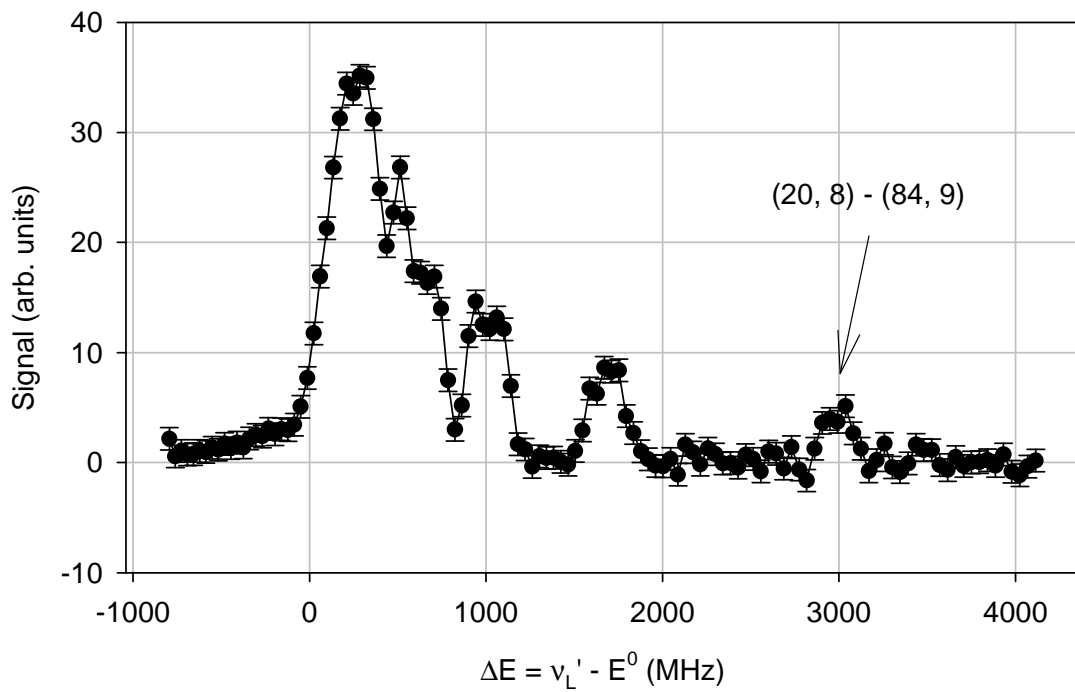
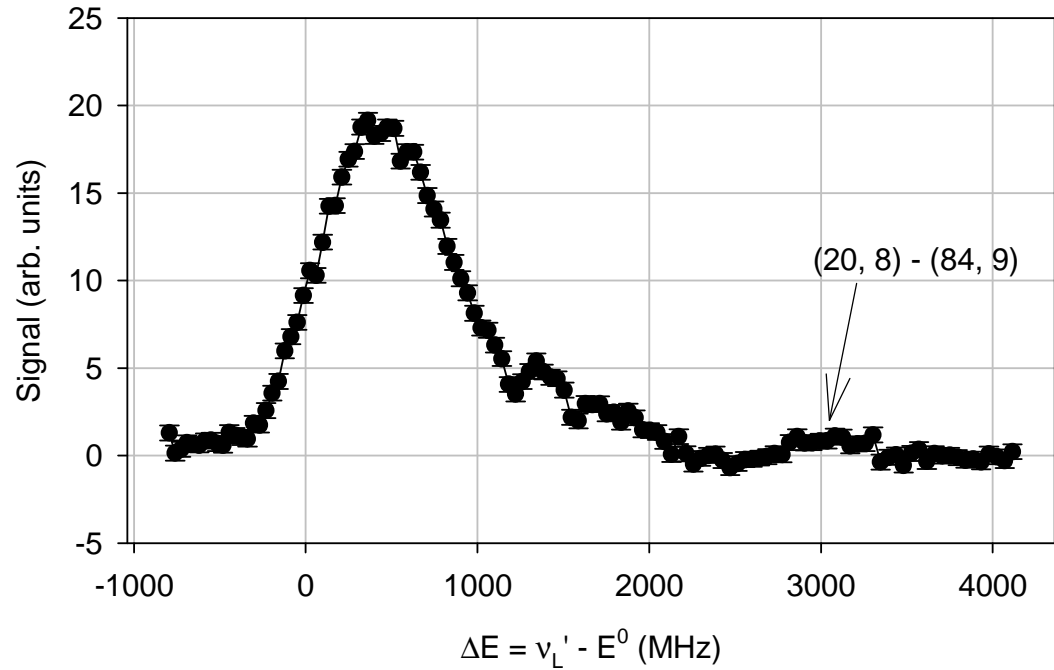


Figure 3.15: Comparison of the resolution of RESIS transitions in $20 - 84 \text{ Pb}^+$ with the compensator off (a) and then tuned to minimize the field (b). The plot in (a) is from scan #8-116 and the plot in (b) is from scan #9-119

Table 3.2: Compensator settings used to minimize the line widths of the $n = 20 - 83$ and $20 - 84$ transitions in Pb^+ and the $37 - 73$ and $38 - 79$ transitions in Th^{3+} . The row labeled as interaction position gives the distance in millimeters from the center of the LIR at which the CO_2 beam intersects the ion beam. A positive value indicates the transition took place upstream, closer to the ECR ion source, and a negative value indicates the transition took place downstream, farther from the ECR ion source.

Transition and Ion:	Pb^+	Pb^+	Pb^+
	20 - 83	20 - 83	20 - 84
Scan ID #	10-073	8-114	8-117
Compensator Axis			
X (V)	1.75	0.48	0.29
Y (V)	-0.91	0.28	0.00
Z (V)	-0.53	-0.58	0.38
Mirror and Post (V)	0.00	0.70	0.90
Interaction position (mm)	18	18	-37

Simulations of the electric field as a function of position were carried out using the values for the compensator voltages that are listed in Table 3.2. The x, y, and z-components of the electric field at the location of the interaction of the Doppler tuned CO_2 laser with the ion beam are listed in Table 3.3 for the different transitions studied. The last two rows in Table 3.3 can provide important clues as to the source of the stray electric field in the LIR. For clarity, the electric field vectors listed along the last two rows of Table 3.3 are plotted in Fig. 3.16. It is intriguing that the electric field seems to always point towards the rear of the LIR and have approximately the same size on all three dates.

Table 3.3: Components of the electric field in the LIR. The last two rows are the magnitude in the XZ-plane and the angle from the positive Z-axis of the electric field.

Transition and Ion:	Pb^+	Pb^+	Pb^+
	20 - 83	20 - 83	20 - 84
Scan ID #	10-073	8-114	8-117
Interaction position (mm)	18	18	-37
dV/dx (mV/cm)	23	35	31
dV/dy (mV/cm)	12	-3	0
dV/dz (mV/cm)	29	45	-61
$ E _{XZ}$ (mV/cm)	37	57	68
Direction	38°	38°	153°

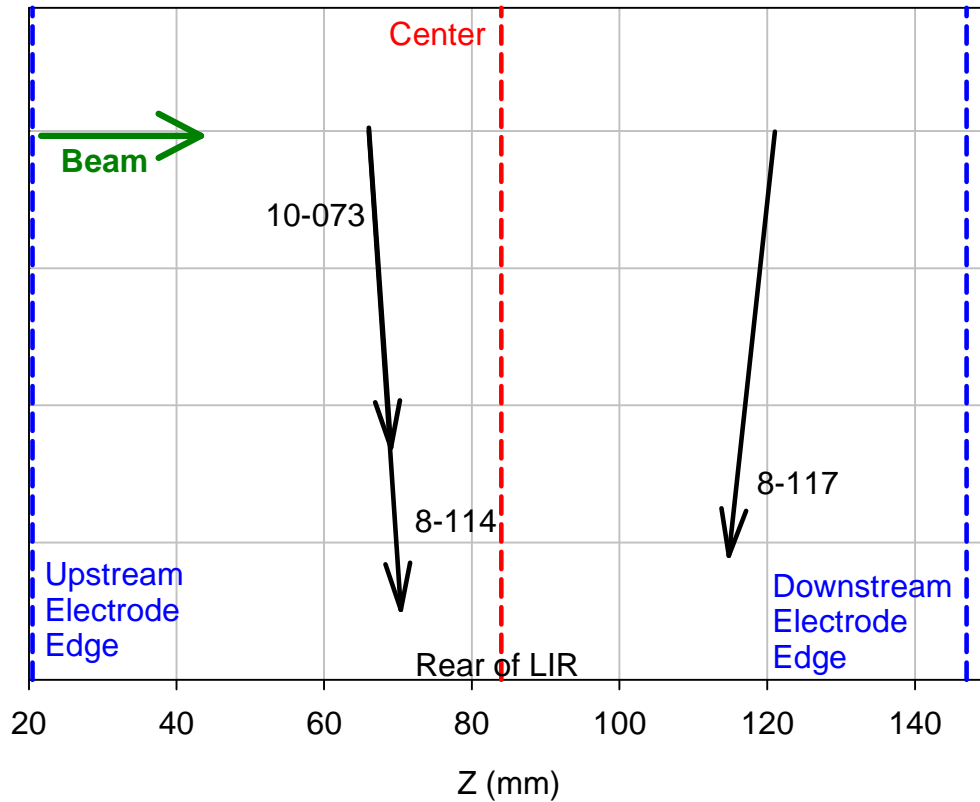


Figure 3.16: Plot of the electric field vectors determined from SIMION simulations of the LIR and compensator assembly. The scan identification numbers are provided next to the vectors for reference with Table 3.6. The x-axis represent the position through the LIR, the beam enters at 0, off to the left hand side of the page, and passes through from left to right. The length of the arrows in the figure corresponds with the magnitude of the electric field listed in Table 3.6.

From the tests of the compensator with the Pb^+ it was shown that the compensator can minimize the stray electric field present in the LIR. Examination of the Rydberg transitions on either side of θ_{\perp} using Rydberg transitions in Pb^+ suggest that the source of the stray electric field is constant and directed towards the rear of the LIR. The motional field from the earth's magnetic field is approximately 0.3 Gauss near the apparatus. This magnetic field would result in a motional electric field approximately 40 mV/cm. It is unlikely that the motional electric field is the source of the stray electric field because an

electric field of this magnitude would only be present if there was zero μ -metal shielding inside the LIR. Another possible source of stray electric field could be the result of a contact potential between the gold mirror/aluminum post assembly in the LIR and the surrounding LIR housing. This could produce an external electric field even though the post is externally grounded. Efforts to eliminate this type of field by putting a bias potential on the aluminum post might have failed due to inadequate electrical contact between the mirror and post assembly.

3.3 Calibration of the stage angle

As mentioned in Chapter 2, the angle recorded by the computer from the rotation stage is related to the intersection angle between the CO₂ laser and the ion beam by an offset angle, θ_{\perp} . This angle represents the angle on the rotation stage at which the reflected CO₂ laser beam propagates exactly perpendicular to the ion beam. Roughly, an error in the determination of θ_{\perp} of 0.05° will lead to an error in the determined fine structure energy of ~ 45 MHz or more, depending upon the velocity of ion beam being studied. Thus, it is critical that the value of θ_{\perp} be known accurately in order to precisely determine the fine structure energies and corresponding properties of the positive ion core being studied.

In order to accurately determine θ_{\perp} the Rydberg fine structure of Si⁺ was observed and analyzed using previous determinations of the properties of Si²⁺ [14]. These properties were measured with great accuracy using the microwave RESIS technique and are reproduced in Table 3.4 from Ref. [14] for reference. The microwave RESIS technique is different from the optical RESIS technique in many different ways. A full

description of the technique is provided in Erica Snow’s dissertation [11] and is beyond the scope of this work. However, it is important to note that the microwave technique has an advantage over the optical RESIS technique in that the observed energies of the fine structure transitions are independent of θ_{\perp} and depend only upon the microwave frequency. As a result of this the microwave RESIS technique is capable of determining the Rydberg fine structure energies with at least an order of magnitude greater precision than the optical RESIS technique and correspondingly higher accuracy in the determined properties of the positive ion core.

Table 3.4: Si^{2+} properties determined using the microwave RESIS technique and the long range polarization model.

Si^{2+} Property	Value [14]
α_{d}	11.666(4) a.u.
$\alpha_{\text{q}} - 6\beta_{\text{d}}$	-53.6(6.2) a.u.

The Si^{+} Rydberg fine structure transitions observed in this work were transitions between $n = 19$ and $n' = 51$ or 52 with beam velocities of $v/c = 0.00078455$. These two transitions were chosen due to their relatively low upper state n , which are insensitive to the effects of stray electric fields that could be present in the apparatus. Simulations of the effects of stray electric fields on the upper state energies involved were carried out by diagonalization the resulting Stark Hamiltonian and determining the resulting line shape from the eigenvalues using a Fortran90 program called StarkWin that was developed by the author. The calculations carried out showed that the upper states involved in this calibration of the θ_{\perp} angle were insensitive to even moderate values of stray electric field of 100 mV/cm. As a result of this, the energy contributions due to stray electric fields in the upper state fine structure energies were neglected in this analysis.

Examples of typical optical RESIS excitation spectra are shown in Fig. 3.7 for both the Si^+ transitions used in determining θ_{\perp} . Each spectrum was fit to a standard Gaussian function using SigmaPlot 2001. The resulting fitted centers for each observation of the Rydberg fine structure for Si^+ are given in Table 3.5.

The Si^+ fine structure was observed seven times, each time resolving three transitions between specific high- L Rydberg states to average out the effects of small fluctuations in the ion beam trajectory in the final determination of θ_{\perp} . Fluctuations in the beam trajectory and the CO_2 laser frequency would slightly change the stage angle and add to an uncertainty in the value of θ_{\perp} determined in this method.

Table 3.5: Fitted centers of the resolved Si^+ fine structure transitions observed using the optical RESIS technique. The errors listed are the uncertainty in the position determined by a four parameter Gaussian fit to the observed signals.

Data File	Transition $(n, L) - (n', L')$					
	$(19, 10) - (51, 11)$	$(19, 9) - (51, 10)$	$(19, 8) - (51, 9)$	$(19, 10) - (52, 11)$	$(19, 9) - (52, 10)$	$(19, 8) - (52, 9)$
12-089	--	--	--	-10.351(4) $^{\circ}$	-9.542(5) $^{\circ}$	-8.014(8) $^{\circ}$
12-090	--	--	--	-10.335(5) $^{\circ}$	-9.534(6) $^{\circ}$	-8.007(9) $^{\circ}$
12-095	--	--	--	-10.357(7) $^{\circ}$	-9.543(9) $^{\circ}$	-8.043(13) $^{\circ}$
12-095B	--	--	--	-10.373(7) $^{\circ}$	-9.568(10) $^{\circ}$	-8.042(15) $^{\circ}$
12-091	12.679(7) $^{\circ}$	13.513(10) $^{\circ}$	15.124(16) $^{\circ}$	--	--	--
12-093	12.568(8) $^{\circ}$	13.374(8) $^{\circ}$	14.966(13) $^{\circ}$	--	--	--
12-094	12.558(7) $^{\circ}$	13.355(8) $^{\circ}$	14.949(13) $^{\circ}$	--	--	--

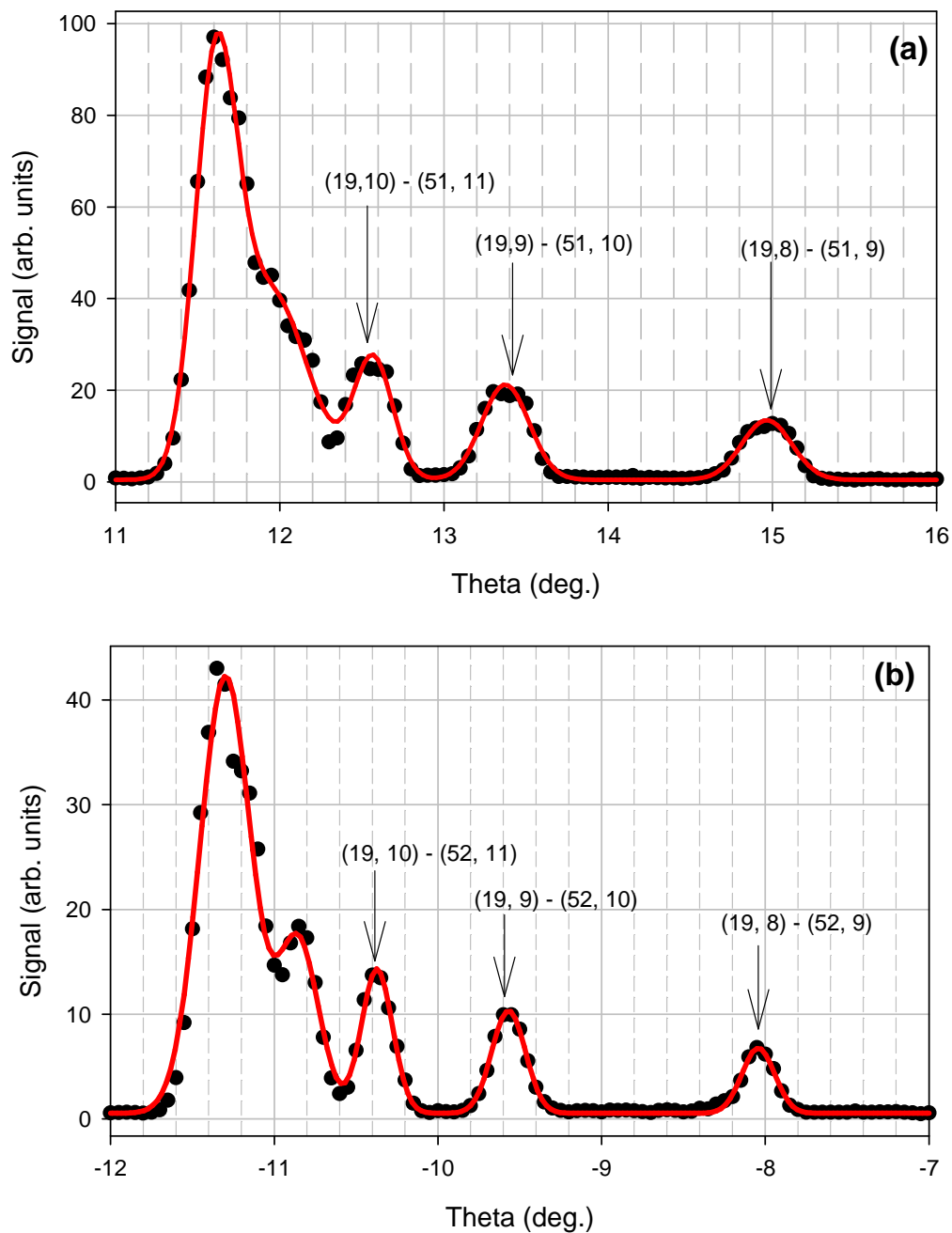


Figure 3.17: Observed Si^+ (a) 19 – 51 and (b) 19 – 52 fine structure transitions used in determining the perpendicular intersection angle of the CO_2 laser with the ion beam. The x-axis represents the angle of the rotation stage controlling the angle the mirror makes with the ion beam as recorded by the computer.

The accurate determination the dipole polarizability of the Si^{2+} ion and contributions to the Rydberg fine structure energies proportional to $\langle r^{-6} \rangle$ using the microwave RESIS technique allows for accurate computation of the fine structure energies using the long range polarization as described in Chapter 1. Additional contributions to the energies of the resolved transitions arise from interactions of the energy levels with other Rydberg series and the relativistic energy of the Rydberg electron that was ignored in the derivation of the effective potential model. These contributions to the energy of the resolved fine structure transitions are added in as *ad hoc* corrections to the energy used to calibrate the stage angle and are discussed in detail in relation to the polarization analysis of the Th^{4+} ion later in this work. Table 3.6 summarizes the calculated fine structure energies using the parameters determined in earlier investigations of the Si^+ Rydberg fine structure [14], the higher order contributions to the energy of the fine structure transitions, and the final transition energy used in calibration of the intersection angles.

Table 3.6: Calculated fine structure energies of Si^+ transitions observed to calibrate θ_{\perp} . The second column lists the energy contributions calculated using the parameters in Table 3.2 and the long range polarization model. Column 3 and 4 are the small energy contributions arising from the relativistic energy ignored in the derivation of the effective potential model and second order energies resulting from the mixing of adjacent Rydberg levels. Column 5 is the sum of columns 2, 3, and 4. The final column lists the calculated laser frequency required to excite the given transition.

Transition (n, L) – (n', L')	ΔE^{Pol} (MHz)	ΔE^{Rel} (MHz)	$\Delta E^{[2]}$ (MHz)	ΔE^{Total} (MHz)	ν_L' (cm^{-1})
(19, 10) – (51, 11)	918.20	21.26	0.21	939.67	1047.1750
(19, 9) – (51, 10)	1549.59	25.18	0.68	1575.45	1047.1963
(19, 8) – (51, 9)	2756.58	30.03	2.42	2789.03	1047.2367
(19, 10) – (52, 11)	920.11	21.34	0.21	941.66	1053.6034
(19, 9) – (52, 10)	1552.62	25.27	0.68	1578.57	1053.6247
(19, 8) – (52, 9)	2761.60	30.14	2.42	2994.16	1053.6652

A value of θ_{\perp} was determined by insisting that the observed angles of the Si⁺ fine structure transitions listed in Table 3.5 corresponded with the calculated fine structure energies listed in Table 3.6. The θ_{\perp} determined from each resolved transition in this fashion is shown in Table 3.7. A value of θ_{\perp} was determined from a weighted average of the values listed in Table 3.7. Taking the weighted average yields $\theta_{\perp} = 1.076(2)^{\circ}$. The reduced χ^2 is 39, presumably due to beam pointing instability, and thus the error bar was expanded by 6.2. A value of $\theta_{\perp} = 1.076(12)^{\circ}$ was then chosen.

Table 3.7: θ_{\perp} determinations obtained by requiring that the resolved RESIS transitions in the Si⁺ Rydberg spectrum correspond with the calculated fine structure energies. The errors listed are the errors determined by the fit of the resolved transitions to a Gaussian.

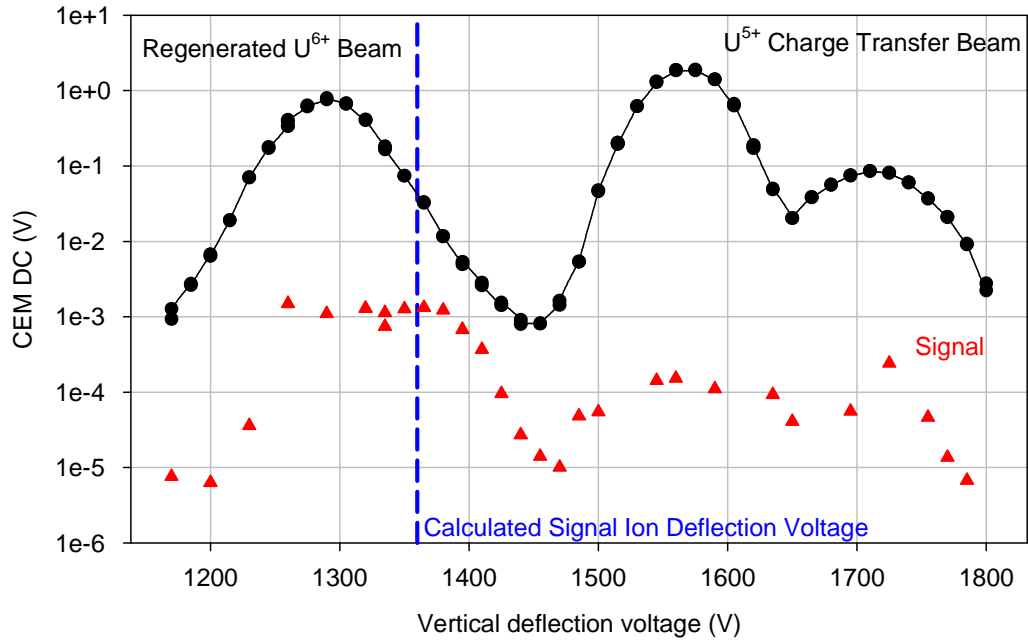
Data File	Transition $(n, L) - (n', L')$					
	(19, 10) – (51, 11)	(19, 9) – (51, 10)	(19, 8) – (51, 9)	(19, 10) – (52, 11)	(19, 9) – (52, 10)	(19, 8) – (52, 9)
12-089	--	--	--	1.049(4) [°]	1.062(5) [°]	1.099(8) [°]
12-090	--	--	--	1.065(5) [°]	1.070(6) [°]	1.106(9) [°]
12-095	--	--	--	1.043(7) [°]	1.061(9) [°]	1.070(13) [°]
12-095B	--	--	--	1.027(7) [°]	1.036(10) [°]	1.070(15) [°]
12-091	1.194(7) [°]	1.216(10) [°]	1.257(16) [°]	--	--	--
12-093	1.083(8) [°]	1.077(8) [°]	1.099(13) [°]	--	--	--
12-094	1.073(7) [°]	1.058(8) [°]	1.082(13) [°]	--	--	--

3.4 Detector modifications and sources of background

As previously mentioned, in the Kr⁶⁺ study a background was present which was the primary source of noise in the RESIS excitation spectrum. It was believed that the background could have been due to the presence of ionizable Rydberg levels that were previously emptied by the pre-ionizing lens or from the incomplete resolution of the Stark ionized and energy tagged Kr⁶⁺ ions from the residual primary Kr⁶⁺ ions and other Kr⁶⁺ ions had been formed from other processes. These sources of background led to the idea to install a 15° charge analyzing magnet after the Rydberg target, separating the

residual Kr^{6+} ions from the Kr^{5+} ions formed by charge exchange with the target. Figure 3.18 shows the profile of the U beams in the detector after installation of the 15° magnet. Notice that there is a large beam present with the same charge and energy as the U^{6+} beam. This was quite a surprise since the U^{5+} beam is well resolved from the U^{6+} beam by the 15° magnet. When the detector is tuned to optimally detect the signal ions, a background more than an order of magnitude larger than the signal is present, as Fig. 3.18 shows. Modifications to the detector were made in an attempt to reduce the background.

Indicated in Fig. 3.18, by the blue dashed line, is the vertical deflection potential at which the ions ionized in the Stark Ionizer would be located when a potential of +5000 V is applied to the stripper electrode. The significant size of the U^{6+} regenerated primary ion beam dwarfs the signal ion beam in the detector resulting in a significantly reduced signal to noise in the RESIS spectra. A figure of merit that can be monitored easily is ratio of DC to signal. Ideally, using the RESIS technique, this ratio should be ~ 1 . In Fig. 3.18 this ratio is ~ 25 .



Detector Version: Straight Terminal Potential: 15 kV P3 Voltage: +5.0 kV

Pre-ionizing Lens Voltage: -8.0 kV Remixing Lens Voltage: -2.0 kV

Figure 3.18: Profile of 90 keV U^{5+} and U^{6+} beams entering the CEM in the RESIS detector. This figure is taken from scan #MH8-150. The regenerated primary U^{6+} ion beam is half of the magnitude as the U^{5+} charge transfer beam. The x-axis represents the deflection voltage applied and the y-axis is the CEM DC voltage output when a potential of -1300 V was applied to the CEM. The red triangles correspond with the signal detected by the lock-in amplifier for reference. The peak of the maximum signal from the 55 – 104 transition in U^{5+} is not clearly resolved from the regenerated U^{6+} primary beam, increasing the background.

The CEM DC measured as a function of the rate of the ions, R , entering the CEM is given by

$$CEMDC(V) = R \cdot g \cdot e \cdot 10^8 \Omega, \quad (3.6)$$

where g is the gain of the CEM when -1100 V is applied to the CEM and e is the electron charge, when the electrometer set to a resistance of 10^8 Ohms. The rate of ions entering the detector when the CO_2 laser is on is

$$R_{LaserOn} = R_{BG} + R_S \quad (3.7)$$

and when the CO_2 laser is off is

$$R_{LaserOff} = R_{BG} , \quad (3.8)$$

where R_{BG} is the rate of ions entering the detector which contribute to the background and R_S is the rate of ions entering the detector which contribute to the signal. A typical time over which a single data point is collected is 20 s. During that 20 second time the CO₂ laser is blocked for a total of 10 s. The difference in the number of ions entering the CEM between when the CO₂ laser is on and off, ΔN , is a measure of the RESIS signal and is given by:

$$\Delta N = N_{LaserOn} - N_{LaserOff} = (R_{LaserOn} - R_{LaserOff}) \cdot 10 \text{ s} = R_S \cdot 10 \text{ s} , \quad (3.9)$$

where $N_{LaserOn}$ is the number of ions entering the CEM when the laser is on, $N_{LaserOff}$ is the number of ions entering the CEM when the laser is off, $R_{LaserOn}$ and $R_{LaserOff}$ are the corresponding rates, and R_S is the rate of ions entering the CEM that contribute to the signal. The uncertainty in the number of ions when the laser is on or off is the square root of the number of the number of ions entering the detector,

$$\sigma_{LaserOn} \approx \sigma_{LaserOff} = \sqrt{R_{BG} \cdot 10 \text{ s}} , \quad (3.10)$$

since $R_{BG} \gg R_S$. The error in the difference ΔN , $\sigma_{\Delta N}$, is given by

$$\sigma_{\Delta N} = \sqrt{R_{BG} \cdot 20 \text{ s}} . \quad (3.11)$$

The error in R_S , σ_S , can then be obtained from Eq. (3.9) and (3.11) and is given by

$$\sigma_S = \frac{\sqrt{R_{BG} \cdot 20 \text{ s}}}{10 \text{ s}} . \quad (3.12)$$

The error in the measured CEM DC can be expressed as

$$\sigma_{DC}(\text{V}) = \sigma_S \cdot g \cdot e \cdot 10^8 \Omega . \quad (3.13)$$

In the limit that $R_{BG} \gg R_S$ Eqs. (3.6) and (3.12) imply

$$\sigma = \sqrt{\frac{CEMDC(V) \cdot g \cdot e \cdot 10^8 \Omega}{5}}, \quad (3.14)$$

which is then an expression for the noise as a function of the CEM DC. One missing value in Eq. (3.14) is the gain of the CEM, g . A study of the noise, as estimated from the scatter of the signal in the y-channel of the lock-in amplifier, as a function of the CEM DC was conducted to determine the value of g with beams of U^{6+} , Ba^{2+} , and Pb^{2+} and to obtain an estimate for the shot noise [21].

The shot noise is a lower limit on the noise that could be expected for a given amount of CEM DC. The black points in Fig. 3.19 correspond to the observed noise level as a function of the CEM DC. All of the points shown in Fig. 3.19 have been adjusted to a collection time of 20 seconds and for a CEM potential of -1100V. The shot noise limit can be obtained by adjusting the parameter g to achieve predicted values of σ , in Eq. (3.14), that are consistent with the lowest points on the graph. Other sources of noise will increase the noise level. The red triangles correspond with the calculated σ from Eq. (3.14) with g fixed at 5000. In this way the shot noise limit in 20 seconds as a function of the CEM DC with a CEM voltage of -1100 V was determined to be:

$$\sigma_{DC} = \sqrt{1.602 \times 10^{-8} \text{ V} \cdot CEMDC(V)}. \quad (3.15)$$

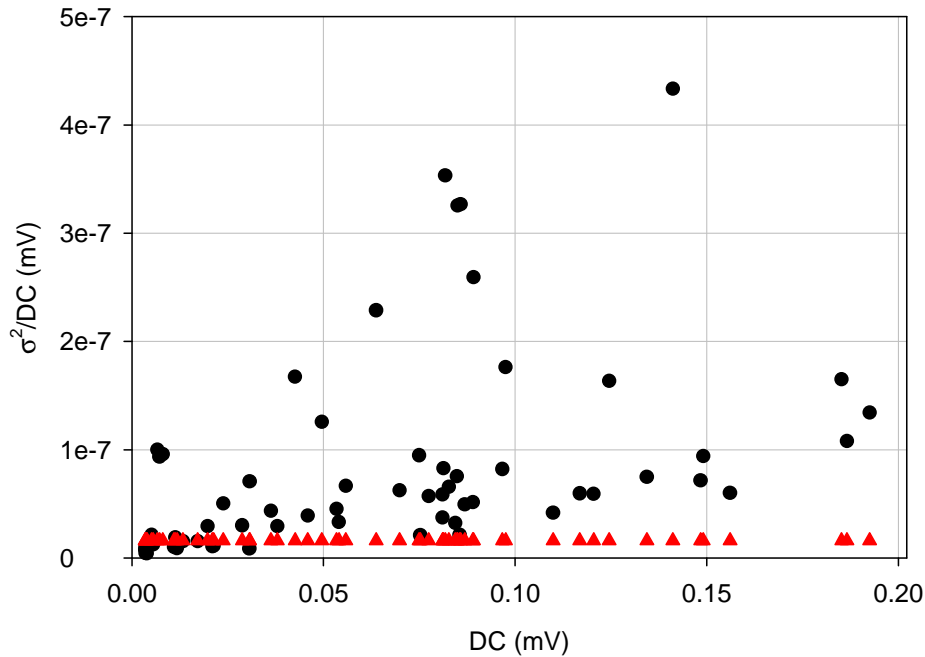


Figure 3.19: Noise level as a function of the CEM DC.

As mentioned previously, the energy tagged ions formed by Stark ionization in the stripper and those formed by other processes could not be fully resolved in the CEM, as shown in Fig. 3.18. To observe the Rydberg fine structures of the Fr-like actinide ions it was required that a modification to the detector housing be devised and implemented that would increase the energy resolution of the detector. The modification consisted of a piece of custom vacuum hardware that tilts the back of the detector upwards at an angle of 8° . This small elbow and revised detector configuration is highlighted in red in the center of Fig 3.20. The upward tilt of the detector increased the vertical deflection of the ion beam necessary to be incident upon the CEM face to $5.9''$. The doubling of the vertical deflection corresponded to nearly a two-fold increase in the vertical separation between all the beams at the entrance to the CEM, and reduced background in the observed in the RESIS spectra.

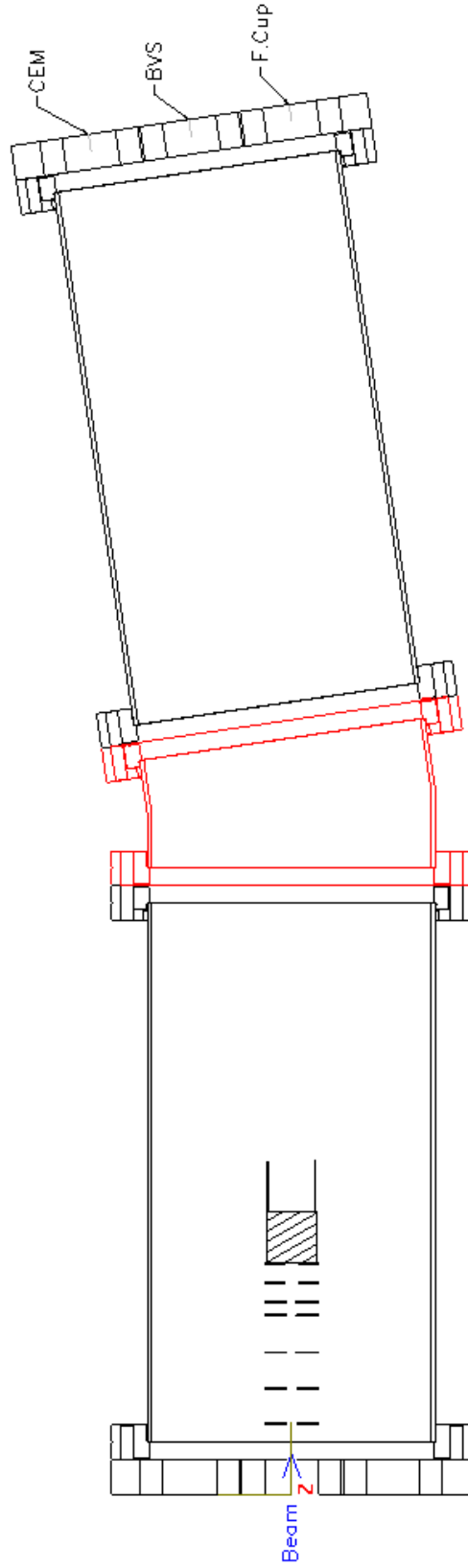
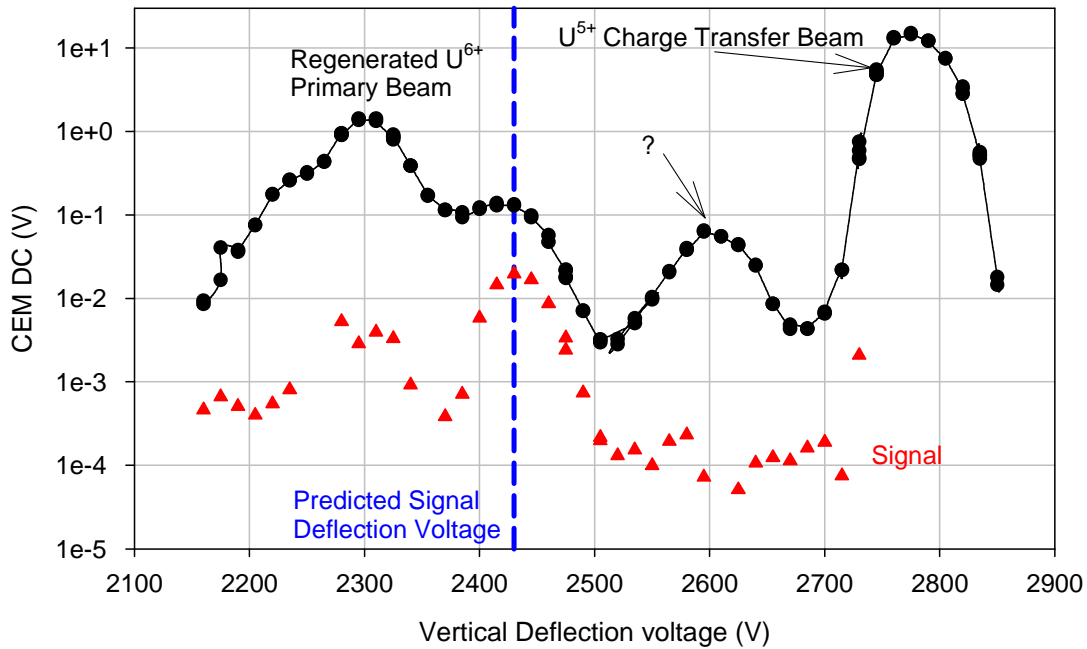


Figure 3.20: Revised detector design. In this version of the detector the addition of the 8° vertical tilt, highlighted in red, results in a doubling of the distance of the CEM entrance from the straight path of the ion beam. This results in a doubling of the kinetic energy resolution of the detector. The arrangement of the BVS and F.Cup are switched in this configuration from the previous configuration. This configuration has the added benefit of no longer requiring switching of the polarity of the vertical deflection plates to image the beam on the BVS.

The increased energy resolution of the new tilted detector that was used in this work is demonstrated in Figure 3.21 and clearly shows the resolution of the ions formed by Stark ionization in the stripper from those formed by other processes. The signal ions occur at 2430V and are well separated from the regenerated U^{6+} primary ions at 2300 V and from the U^{5+} ions at 2780V.

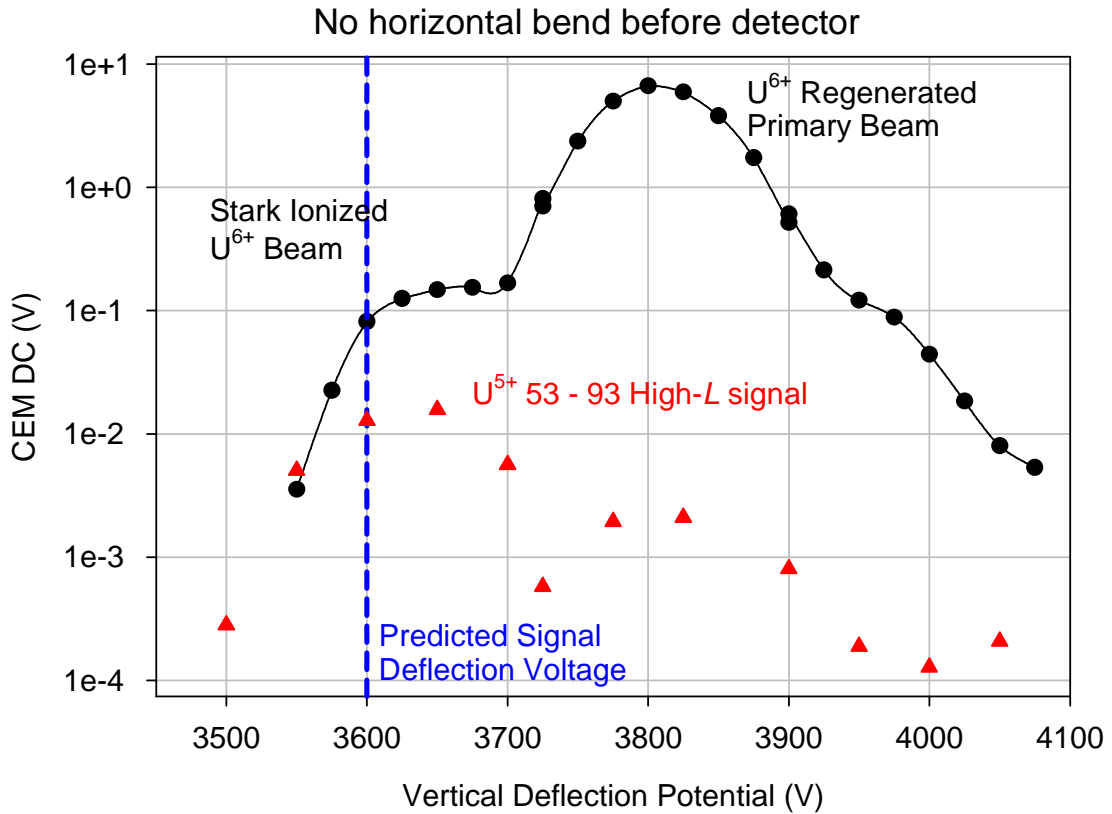


Detector Version: Tilted Terminal Potential: 15 kV P3 Potential: +5.6 kV
 Pre-ionizing Lens potential: -9.0 kV Re-mixing Lens Potential: -3.0 kV

Figure 3.21: Profile of the 90 keV U^{6+} and U^{5+} beams entering the CEM after installation of the $\sim 8^\circ$ vertical tilt in the detector. This figure is reproduced from scan #MH11-003. The CEM had a -1500 V potential applied for this profile. The blue dashed line corresponds with the location predicted for the 52 – 102 U^{5+} signal ions formed by Stark ionization when the stripper electrode is held at a potential of +5600V.

To avoid any complications that could arise due to the unknown beam at 2600V the positive power supply that supplied the potential to the stripping electrodes was changed to a negative power supply so that the signal ion beam would appear on the opposite side of the regenerated primary beam. The profile of the beams in the detector after changing the potentials is shown in Figure 3.22. Despite this new configuration the ratio of the

CEM DC to signal was non-ideal in both cases. At the peak signal in Fig. 3.21 this ratio is ~ 7 and in Fig. 3.22 this ratio is ~ 6 .



Detector Version: Tilted Terminal Potential: 25 kV P3 Potential: -8.1 kV
 Pre-ionizing Lens potential: 9.5 kV Re-mixing Lens Potential: 3.5 kV
 Figure 3.22: Profile of the 150 keV U⁶⁺ and U⁵⁺ beams entering the detector using the new potential arrangement. This figure is reproduced from Scan #11-103

Although the upward tilt of the detector improved the energy resolution of the detector the modification has not eliminated the background. A second device was constructed to charge analyze the beams just before entering the detector. The device consisted of a set of electrostatic deflection plates just prior to the entrance of the detector. The detector region was then attached to the beam line via a 3.375" con-flat flexible coupling and a movable supporting mount that allows the detector to swing about a fixed point just prior to the entrance of the detector. The detector conveniently already housed a 6 mm aperture at its entrance. By using this aperture in conjunction with the

electrostatic deflection plates and swinging the detector off the straight line axis of the rest of the beam line, the regenerated primary beam would be deflected into the side of the entrance aperture when the charge transfer ion beam was steered to enter the detector. The deflector plates were installed in a 6" Con-Flat 6-way cross that was being used to attach an additional turbo pump just prior to the detector. A CAD schematic of the complete horizontal deflection assembly showing the bellows and front flange of the detector containing the 6 mm entrance aperture is shown in Fig. 3.23. The supporting mount was designed and constructed by Charles Fehrenbach at JRML and the electrostatic deflection assembly was designed and constructed by the author at Colorado State University.

The horizontal deflection of the ion beams is achieved using a series of two different electric fields to deflect the beam. Two different electric fields are required to adjust both the horizontal position and direction of the deflected beam. The horizontal deflection plates consist of two sets of stainless steel plates held at high voltage that are separated by 6 cm. The plates were constructed out of 0.0625" thick stainless steel mounted to 0.25" thick stainless steel supports. The 0.065" thick plates are electrically isolated from the support plates by 0.187" diameter ceramic spheres that were purchased from Kimball Physics' eV parts line of high voltage compatible components. The first series of plates, labeled E1 in Fig. 3.22, are 3.54" long and the second series, labeled E2, are 5.91" long. The lengths of these plates were chosen to reduce the electric fields required to deflect the ion beam and to fit within the existing vacuum hardware present on the apparatus. A photograph of the completed assembly electrode assembly is shown in Fig. 3.24.

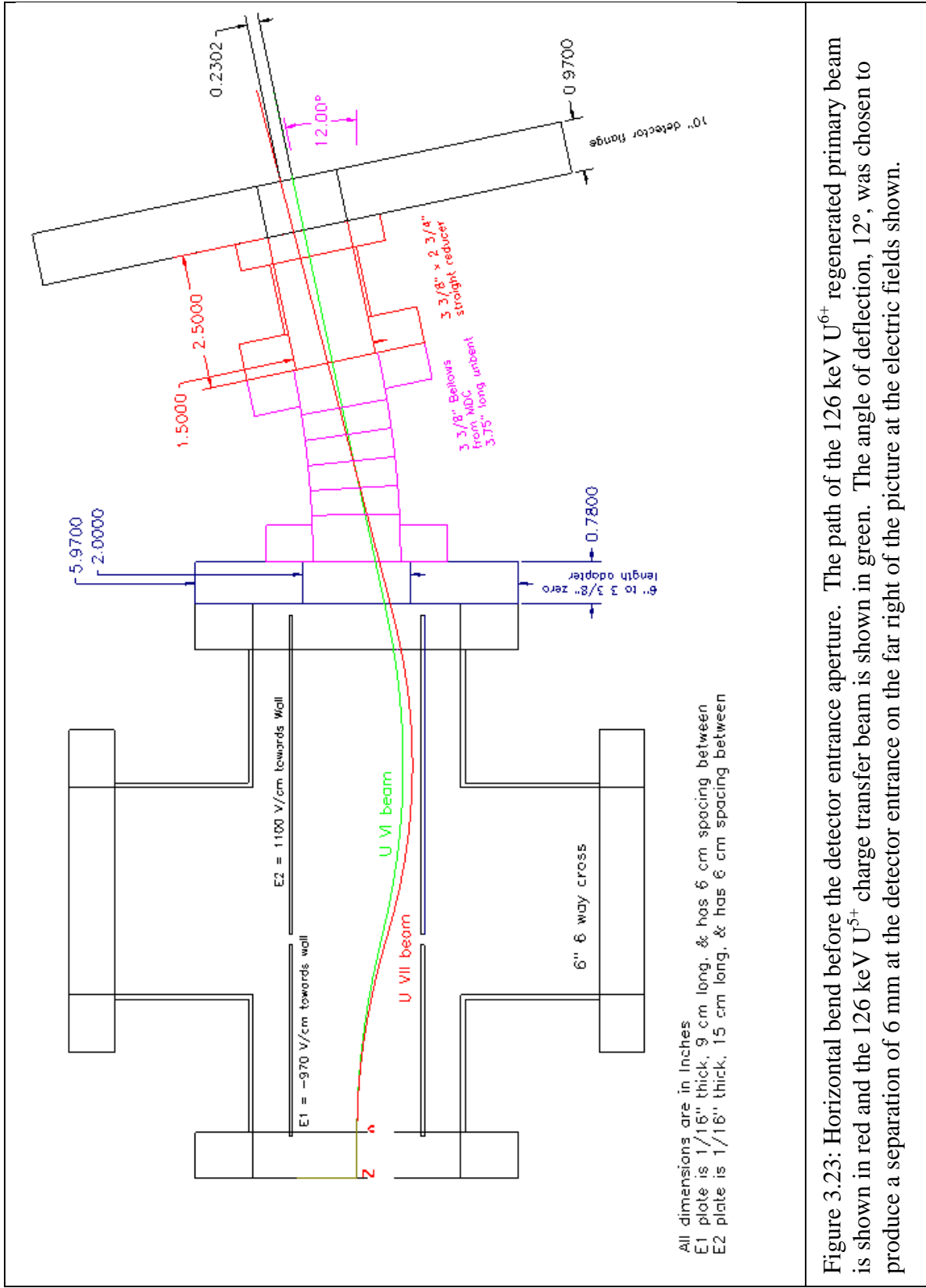


Figure 3.23: Horizontal bend before the detector entrance aperture. The path of the 126 keV U^{6+} regenerated primary beam is shown in red and the 126 keV U^{5+} charge transfer beam is shown in green. The angle of deflection, 12° , was chosen to produce a separation of 6 mm at the detector entrance on the far right of the picture at the electric fields shown.

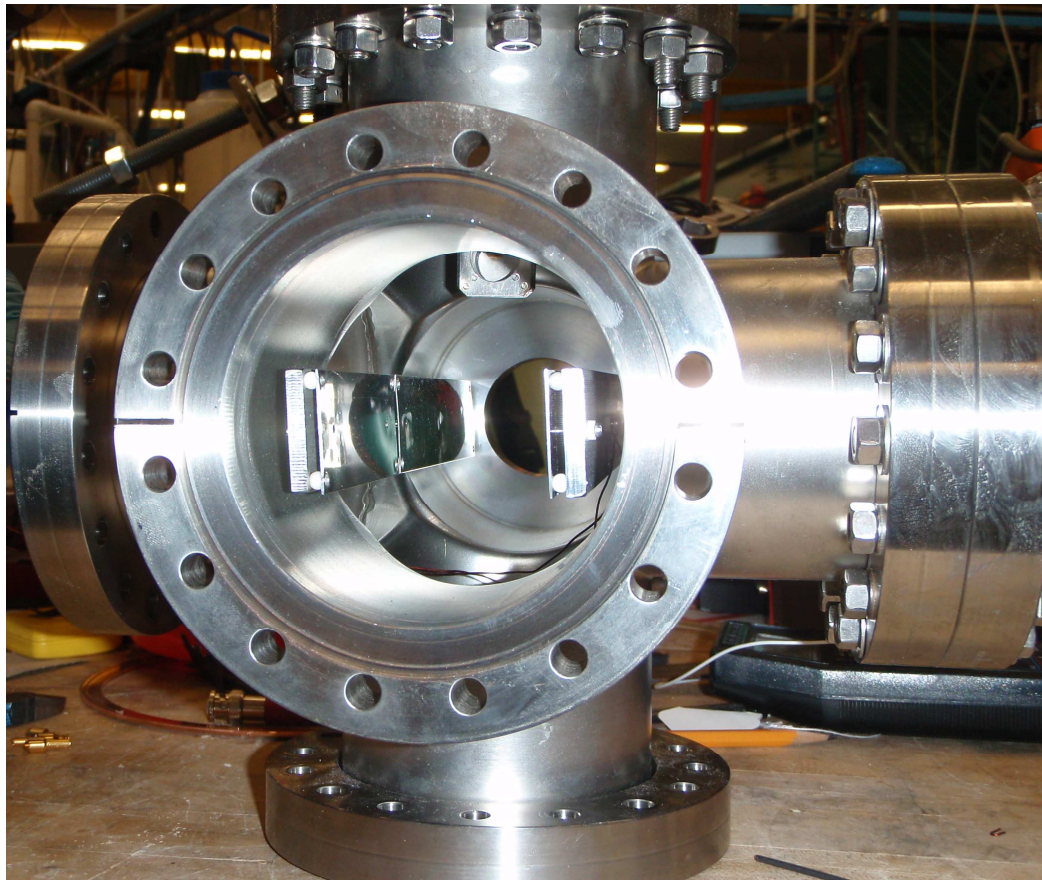
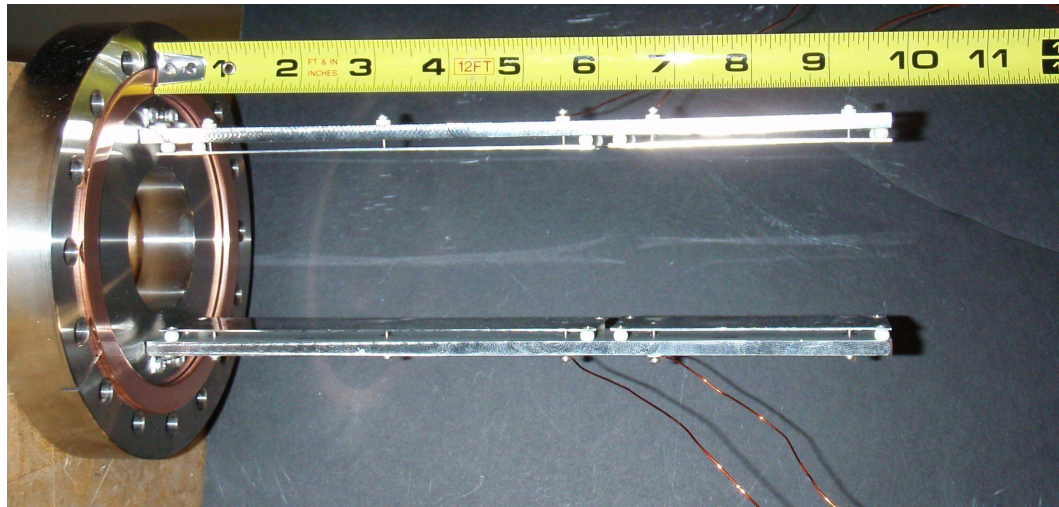


Figure 3.24: Horizontal deflector assembly. The top photograph shows the complete horizontal deflector assembly showing the high voltage plates and support structure attached to the 6" Con-Flat flange. The bottom photograph shows the assembly installed in the 6-way cross that attaches the 3.375" flexible coupling and detector region to the LIR.

The variable angle horizontal bend in the beam line just prior to the entrance to the detector was tested with a 150 keV U^{6+} beam. Using a simple square electric field approximation, assuming an infinitely small beam, and ignoring space charge effects, a model was created in SigmaPlot to numerically estimate the fields required to successfully direct the beam through the entrance aperture of the detector. To test the device first a profile was taken of the regenerated U^{6+} primary ion beam and Stark ionized U^{6+} ion beam when the CO_2 laser was tuned to the dominant $n = 53 - 93$ transition in U^{5+} . The profile is shown in Fig. 3.22 and is a reproduction of scan #MH11-103. Initially it was calculated that in order to obtain a separation of 6 mm at the detector entrance a minimum bent angle of 10° for the beam line was required. The detector was angled slightly off axis and the profile of the beams in the detector was repeated. Fig. 3.25, reproducing scan #MH11-104, is a repeat of the profile of the beams in the detector with only a 4° bend angle present. Although profiles of the beams in the detector with larger bending angles of 6° and 8° were taken, no additional gains were observed. Table 3.8 lists the calculated steering potentials and the actual potentials that were applied to the deflection plates to steer the 150 keV U^{6+} beam into the detector at the varying bend angles. The CEM channel plate had a bias of -1300 V applied in both profiles shown in Fig. 3.22 and 3.25.

Table 3.8: Comparison of estimated and actual horizontal deflection steering potentials. The estimated potentials do not match the actual potentials required to direct the 150 keV U^{6+} beam into the detector, highlighting that the simple model is not accurate enough. The actual steering potentials are from book MH11 pages 104, 105, and 106.

Angle	Estimated			Actual		
	E1 (V)	E2 (V)	E2/E1	E1 (V)	E2 (V)	E2/E1
4°	-1575	1800	-1.14	-740	1380	-1.86
6°	-2364	2700	-1.14	-1280	2095	-1.64
8°	-3150	3600	-1.14	-1720	2710	-1.58

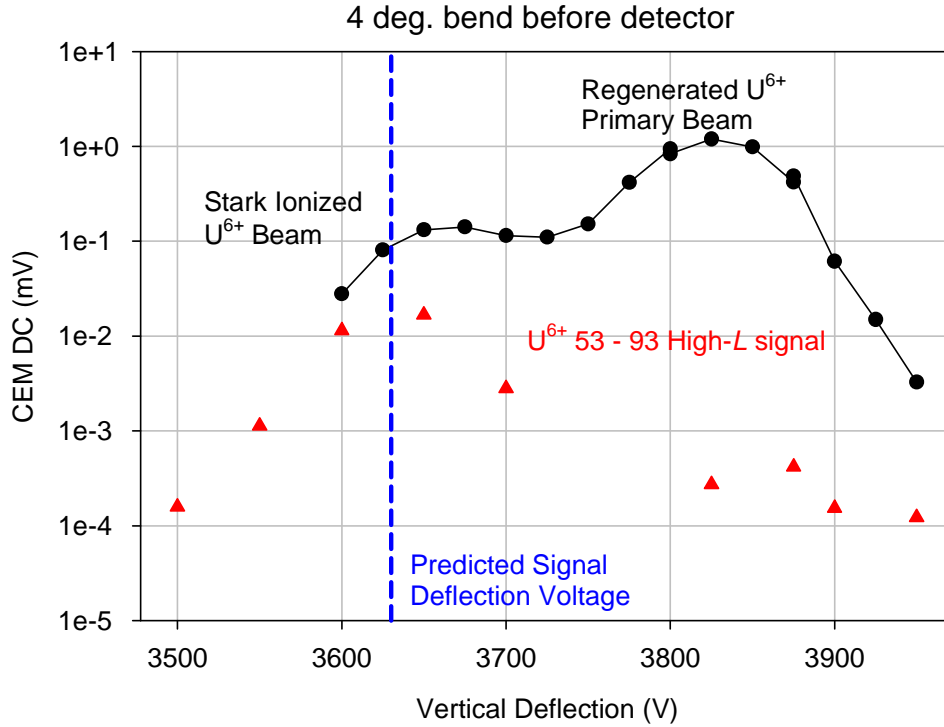


Figure 3.25: Regenerated 150 keV U^{6+} and Stark ionized U^{6+} beam profiles in the detector with a 4° bend in the beam line just before the detector. The factor of 10 reduction in the primary beam magnitude, in comparison with Fig. 3.22, in the detector corresponds almost exactly to the expected reduction proportional to the ratio of the lengths of the beam line if a constant process is responsible for the production of the U^{6+} regenerated primary beam. Unfortunately, there is no reduction in the background at the position of the RESIS signal.

The regenerated U^{6+} primary beam was significantly reduced, as can be seen by comparing Fig. 3.25 and Fig. 3.22, but the background at the position of the Stark ionized U^{6+} was not. The reduction of the regenerated primary U^{6+} beam by a factor of 10 roughly corresponds to the ratio of the distance between the Rydberg target to the detector entrance, $70''$, and the length between the end of the last electrode in the horizontal deflector to the detector entrance, $8''$. The reduction of the regenerated U^{6+} primary beam by the horizontal bend before the detector is consistent with a constant production of the U^{6+} beam throughout the length of the apparatus. The horizontal deflection just prior to the detector is able to completely deflect the primary beam even at small angles. Also note that there is no signal loss when the horizontal deflection is used

if adequate care is taken in re-tuning the beam after horizontal adjustment of the detector. Unfortunately, this modification did not affect the large DC levels in the location of the maximum signal in the detector. As a result, this device was not employed for the conclusions presented in this work.

Even with the modifications to the detector there remains a significant level of background ions collected in the detector. The possible sources of the background that are known are from:

- 1) The incomplete separation of the ions formed in the Stark ionizer from those of the same charge.
- 2) The ionization of weakly bound Rydberg states in the Stark ionizer that were not completely ionized by the pre-ionizing lens.
- 3) The collisional re-population and subsequent Stark ionization of Rydberg levels previously emptied by the pre-ionizing lens.
- 4) Collisional ionization occurring within the Stark ionizer due to collisions of the ion beam with the residual gas.
- 5) Auto-ionization of Rydberg states attached to metastable excited ion cores.

Each of these different sources of background will present unique profiles in the detector that can be used to differentiate the sources of background. Shown in Fig. 3.26 are the profiles corresponding with the five known sources of background. The light blue circle corresponds with the signal ions that are Stark ionized and energy tagged in the Stark ionizer while the orange circle corresponds with ions of the same charge formed but with the energy of the primary beam. The orange bar corresponds to ions formed by ionization throughout the varying potential in the Stark ionizer. If the dominant source of

background arises from 1) above then the profile signature in the detector is expected to resemble the profile shown in Fig. 3.26(a). If the background is dominantly from sources 2) or 3) then the profile would most likely look similar to the profile shown in Fig. 3.26(b). Finally, if the background is due to sources 4) or 5) then the profile of the beams in the detector would most likely resemble the profile shown in Fig. 3.26(c).

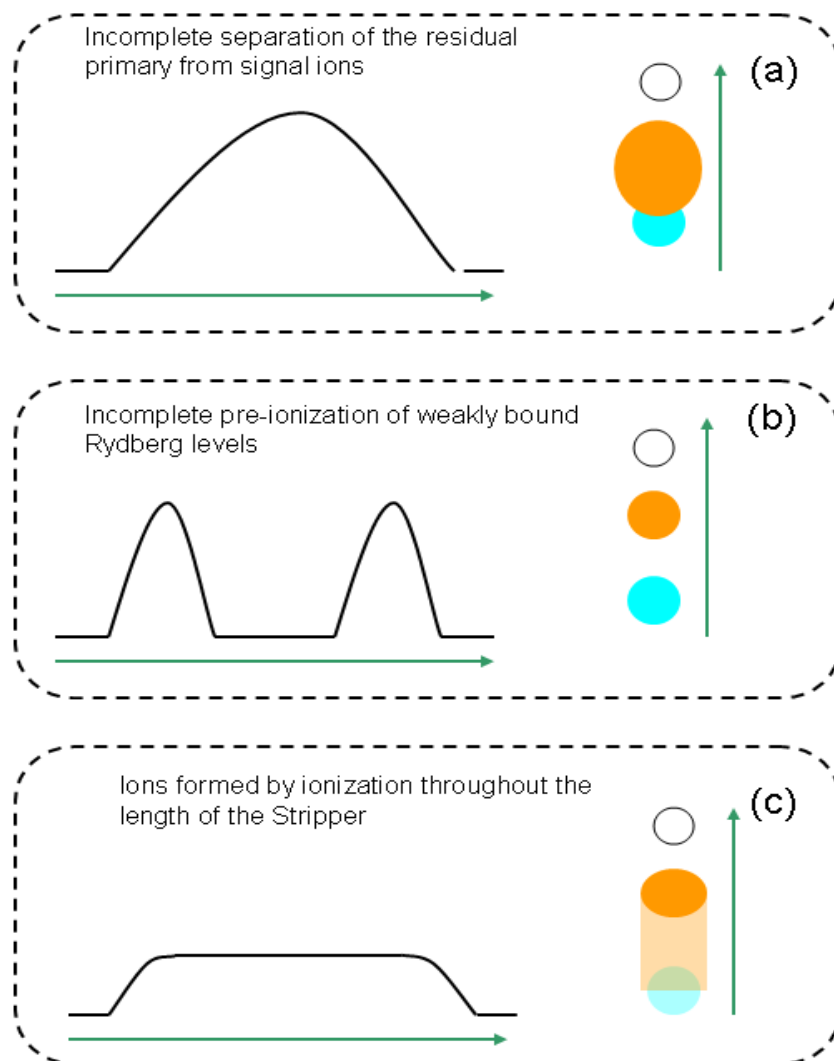


Figure 3.26: Schematic diagrams of CEM DC profiles resulting from different sources of background. In all three panels the green arrow indicates increasing vertical deflection potential required to deflect the beams into the CEM entrance aperture shown as the open circle. The left side of the panels is a CEM DC profile and the right is a rendering of what the beams might look like when viewed in the beam viewing system.

The possibility of the dominant source of the additional background arising from incomplete separation of the primary beam ions from the ions formed by Stark ionization can be evaluated by comparing the beam profiles presented in Fig. 3.22 and Fig. 3.25. A factor of 10 reduction in the amount of regenerated U^{6+} primary ions should have led to reduction in background from source 1). This indicates that the dominant source of background is not source 1).

If source 2), the incomplete pre-ionization of weakly bound Rydberg levels in the pre-ionizing lens, was the dominant source of the background then the profiles of the beams in the detector would be expected to look similar to panel (b) in Fig. 3.26. In other words, the shape of the background in the detector should be similar to the shape of the signal. The plateau shape of the background, evident in Fig. 3.25, extending between the U^{6+} regenerated primary beam and the signal indicates that the dominant source of background is not due to the Stark ionization of Rydberg levels from either source 2) or 3).

Evidence against source 3) and 4) was provided by data showing that the background was independent of system pressure. Data supporting this conclusion resulted when the repeller lens shorted, requiring that the apparatus to be vented to atmosphere for an entire day for repairs. Prior to this the detector pressure was typically 4.4×10^{-9} Torr. The day after repairs were completed data acquisition was resumed on the 84 keV U VI 55 – 104 transition. During this time the detector was at pressures around 3.2×10^{-8} Torr, a factor of 7 higher. The pressures in the LIR increased from a typical value of 4.7×10^{-8} Torr before venting by a factor of ~ 10 to 4.5×10^{-7} Torr after venting.

Table 3.9: Comparison of the DC to High-L ratio with excellent and not so excellent detector pressures.

Scan ID #	LIR Pressure (Torr)	Detector Pressure (Torr)	$S(HL)$ (mV)	CEM DC (mV)	DC/ $S(HL)$
6-037	4.7×10^{-8}	4.5×10^{-9}	0.975(14)	30.9	41.9(6)
6-038	4.7×10^{-8}	4.4×10^{-9}	1.004(12)	27.1	27.9(3)
6-039	4.7×10^{-8}	4.4×10^{-9}	0.946(19)	25.6	27.1(5)
6-051	5.1×10^{-7}	3.5×10^{-8}	0.646(14)	20.1	31.1(7)
6-052	3.9×10^{-7}	3.1×10^{-8}	1.0039(25)	36.3	34.9(8)
6-053	4.7×10^{-7}	3.1×10^{-8}	1.001(27)	37.8	37.8(1.0)
6-055	4.3×10^{-7}	3.1×10^{-8}	0.994(37)	33.2	33.4(1.2)

In the lower detector and LIR pressure cases listed in Table 3.9 the average CEM DC/ $S(HL)$ is:

$$\left(\frac{DC}{S(HL)} \right)_{LowP} = 32(5).$$

In the higher detector and LIR pressure cases listed in Table 3.9 the average CEM DC/ $S(HL)$ is:

$$\left(\frac{DC}{S(HL)} \right)_{HighP} = 34(2).$$

The value of the DC to the $S(HL)$ in the low pressure case is completely consistent with the high pressure case, even though the pressures are almost an order of magnitude higher in both the LIR and the detector. It seems implausible that if collisional processes are an important source of background these effects would not be vastly increased when the system pressures are worse by nearly an order of magnitude.

If the dominant source of background in the U^{6+} experiment is not due to sources 1) through 4) the only known remaining process is the auto-ionization of Rydberg levels attached to metastable excited core states. The first excited states of U^{6+} are shown in Fig. 3.27. The energies were calculated by D. Beck using a Dirac-Fock method [10], but

have never been determined experimentally. The first excited configuration is $6p^5(^2P_{3/2})5f$ and consists of many levels, all of which are metastable. The red lines depict Rydberg levels that are bound by ~ 0.1 eV. In the $6p^5(^2P_{3/2})5f$ excited states all of the levels, except for the $J_c = 1$ state, are capable of auto-ionization by quadrupole coupling into the continuum energy of an adjacent excited state with a different J_c . Since the ECR plasma is quite hot, it seems plausible that a thermal transition to the first excited state is possible. If auto-ionization is occurring throughout the length of the Stark ionizer then the profile of the beams would be expected to resemble what is depicted in panel (c) of Fig. 3.26, which most closely resembles the profiles observed in the detector.

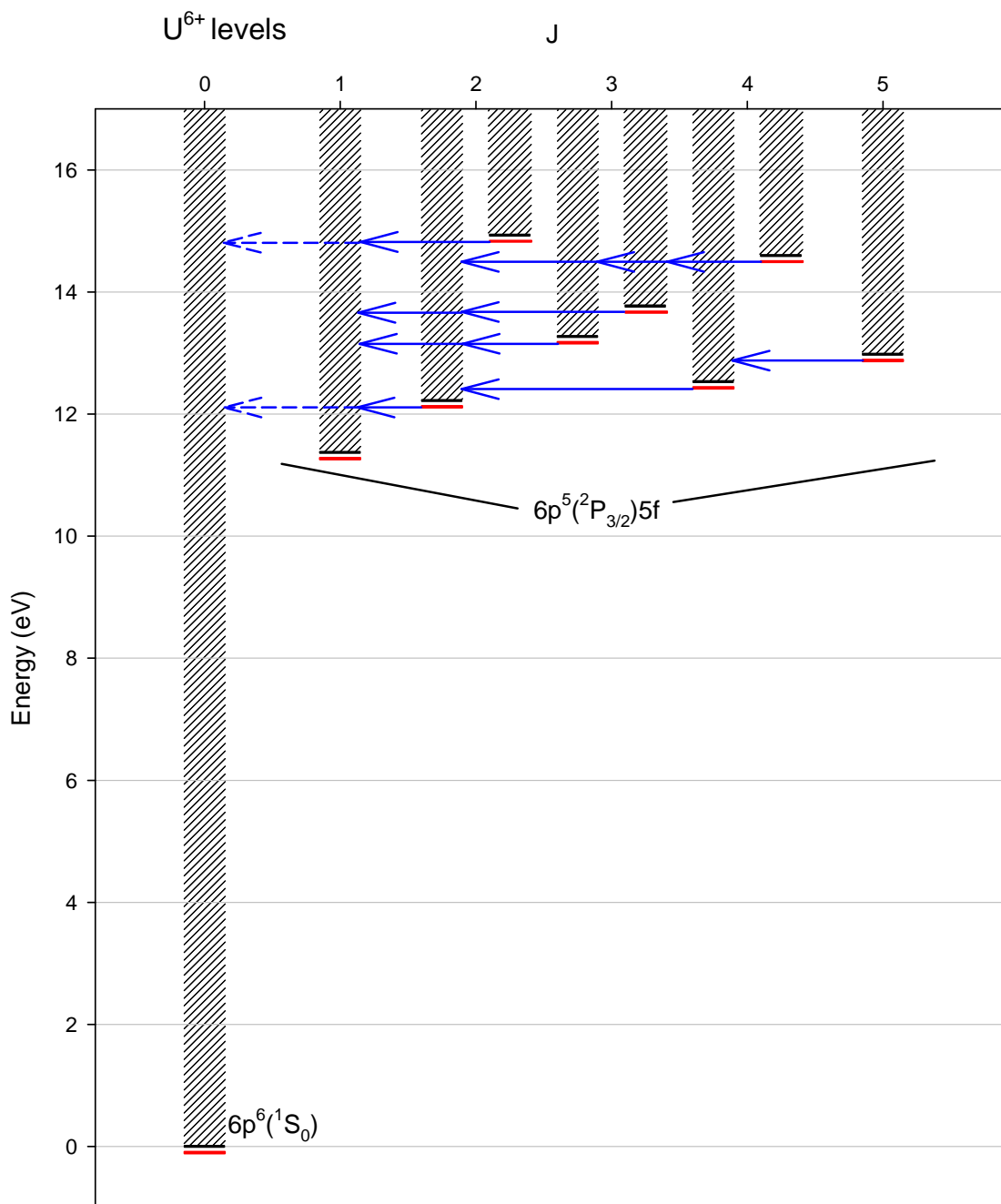


Figure 3.27: Estimated energy level diagram of U^{6+} , showing the ground and first excited states. The first excited states are metastable. Shown by the red lines are Rydberg levels that are about by ~ 0.1 eV. The blue arrows indicate the dominant auto-ionization paths possible. The dashed blue arrows correspond to auto-ionization paths that occur with a much lower rate.

The auto-ionization rates must be estimated to determine if the dominant contribution to the background in the RESIS excitation spectra can be plausibly attributed to the auto-ionization of Rydberg levels. A closer view of the levels with different J_c in the $6p^55f$ level in U^{6+} is shown in Fig. 3.28. Also shown in the figure are the various paths of auto-ionization and estimates of the corresponding auto-ionization lifetimes of Rydberg states with $n = 56$ and $L = 15$ in the core states with different values J_c . The auto-ionization rates can be estimated from Fermi's golden rule. Fermi's golden rule states that the transition rate between two states, A , is given by:

$$A = \frac{2\pi}{\hbar} |\langle \Psi | V | \Psi' \rangle|^2 \quad [31]. \quad (3.12)$$

The same result can also be derived from time dependant perturbation theory. Since only quadrupole transitions are possible between the states with different J_c , leading to auto-ionization, the quantity $|\langle \Psi | V | \Psi' \rangle|^2$ in Eq. 3.12 is obtained from the long range polarization model as

$$|\langle \Psi | V | \Psi' \rangle|^2 = \left| \langle \Psi | \vec{Q} \cdot \frac{C^{[2]}(\Omega_N)}{r_N^3} | \Psi' \rangle \right|^2. \quad (3.13)$$

Using methods similar to those in Chapter 1, the matrix element in Eq. (3.13) can be expressed using 3-J and 6-J symbols. The resulting expression is

$$\begin{aligned} |\langle \Psi | V | \Psi' \rangle|^2 = & [(2L+1)(2L'+1)] \begin{pmatrix} L & 2 & L' \\ 0 & 0 & 0 \end{pmatrix}^2 \begin{Bmatrix} K & L & J_c \\ 2 & J'_c & L' \end{Bmatrix}^2, \\ & \times \langle J'_c \| \vec{Q} \| J_c \rangle^2 \langle n, L \| r^{-3} \| \varepsilon, L' \rangle^2 \end{aligned} \quad (3.3)$$

where ε is the energy of the auto-ionized electron and $K = J_c + L$. The value of the quadrupole matrix element, $\langle J'_c \| \vec{Q} \| J_c \rangle$, in Eq. (3.14) is unknown and was assumed to be

1 a.u. for simplicity. The radial matrix element in Eq. (3.14) was calculated with a Fortran routine developed by Julie Keele [21]. The sum of the individual auto-ionization rate from a state with given J_c , n , and L to a continuum state with energy ε , $J'_c - J_c = 1$ or 2 , and $L' = L, L \pm 2$ was then computed to determine an estimate for the total auto ionization rate.

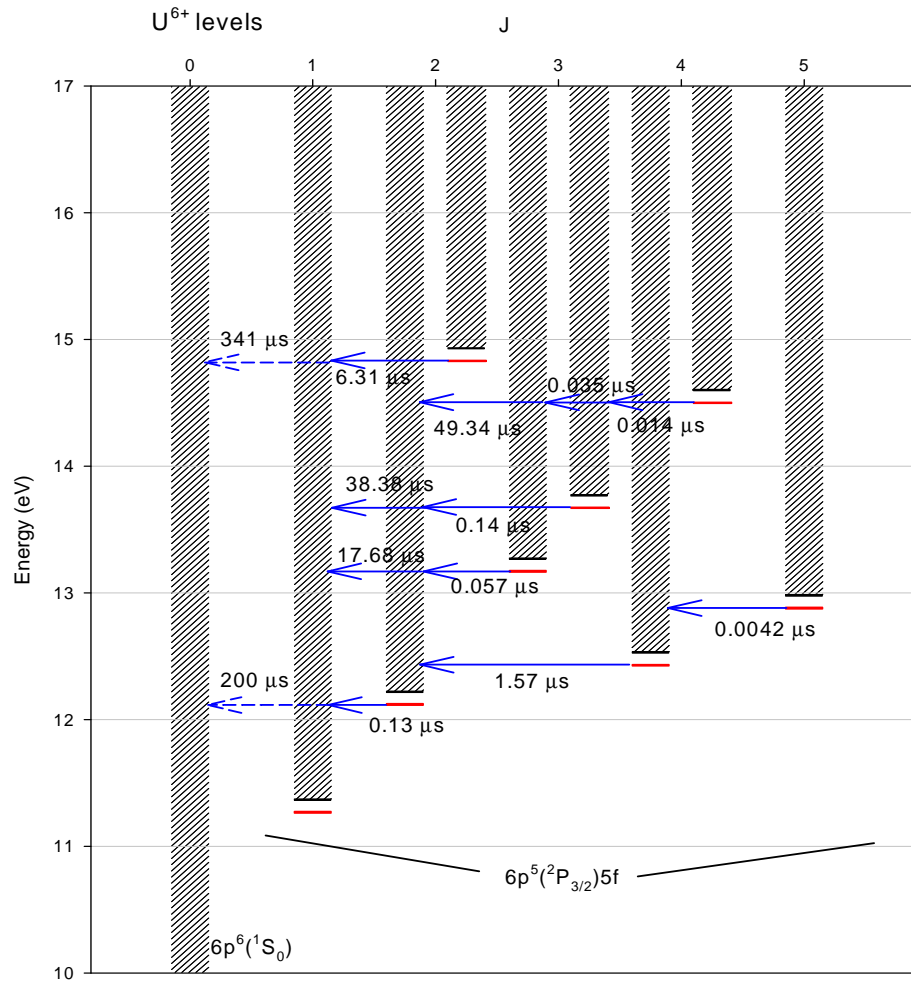


Figure 3.28: $6p^5 5f$ levels in U^{6+} and estimated auto-ionization lifetimes for Rydberg states with $n = 56$ and $L = 15$. The rates to the ground state from the $J_c = 2$ states are shown above dashed blue lines. The auto-ionization rate from the $J_c = 2$ to ground state is much lower than any of the other auto-ionization paths shown.

In order to evaluate the plausibility of the hypothesis that auto-ionizing Rydberg states are the dominant sources of background, a trend of the auto-ionization rate as a function of n and L was established. The trend was determined by calculating the rates for states with $n = 30, 39, \text{ and } 56$ and $L = 5, 10, 15, \text{ and } 20$. The n 's were chosen based on the capture cross section for a 150 keV U^{6+} beam intersecting a 10F Rydberg target. The peak of the capture distribution was at $n = 39$. The values of $n = 30$ and 56 correspond with the location of the half maximum on either side of the capture distribution. The values of n for the Th^{4+} auto-ionization rate calculations were chosen in the same manner. The value of L 's were chosen beginning with $L = 5$, where the long range polarization model is applicable, and increasing until the routine calculating the radial matrix element became unreliable. The average auto-ionization rate for a particular (n, L) state was determined by averaging the auto-ionization rates between different J_c 's. The average auto-ionization rates that were determined are shown in Table 3.10. The trend of the average rates suggest that the auto-ionization rate can be approximated by

$$A_{AI}(Q, n, L) \approx 1.122 \times 10^{11} \cdot Q^6 \cdot n^{-3} \cdot L^{-8} \mu\text{s}^{-1}, \quad (3.15)$$

the value $1.122 \times 10^{11} \mu\text{s}^{-1}$ was fixed to obtain estimated rates that correspond with those listed in Table 3.10.

Table 3.10: Average estimated auto-ionization rates for U^{6+} and Th^{4+} .

U^{6+} State (n, L)	U^{6+} Average Auto- ionization Rate (μs^{-1})	Th^{4+} State (n, L)	Th^{4+} Average Auto- ionization Rate (μs^{-1})
(30, 5)	488,847	(24, 5)	86,355
(30, 10)	5,255	(24, 10)	403
(30, 15)	77	(24, 15)	1.61
(30, 20)	0.23	(24, 20)	0.0011
(39, 5)	239,206	(27, 5)	61,491
(39, 10)	2671	(27, 10)	421
(39, 15)	66	(27, 15)	1.95
(39, 20)	0.6	(27, 20)	0.0017
(56, 5)	77,595	(31, 5)	41,200
(56, 10)	800	(31, 10)	313
(56, 15)	34	(31, 15)	2
(56, 20)	0.7	(31, 20)	0.23

With an approximate understanding of how the auto-ionization rates depend upon n and L a model of the predicted amount of background for a given amount of charge capture from the Rydberg target can be developed for comparison with observations. The model requires knowledge of the distribution of the population across n and L 's for a given beam and Rydberg target. The capture cross-section distribution in n was readily obtained from Classical Trajectory Monte Carlo (CTMC) calculations using codes developed by Ron Olson [26] and is analogous to the population distribution in n . The distribution of the population into specific L 's was assumed to be uniform. Thus the population into a given (n, L) state, $\sigma(n, L)$, was taken to be

$$\sigma(n, L) = \frac{\sigma(n)}{n}, \quad (3.16)$$

where $\sigma(n)$ is the capture cross-section into a given n predicted by CTMC.

The model also requires knowledge of the probability for an auto-ionizable Rydberg state to be detected with the signal ions, resulting in contributions to the background in the RESIS excitation spectra, and the probability of an auto-ionizable Rydberg state to

contribute to the regenerated primary beam. The probability of a metastable ion surviving to the detector, ionizing at a potential in the Stark ionizer to be detected, P_{BG} , is

$$P_{BG}(Q, n, L) = e^{-A(Q, n, L)T_{det}} \left(1 - e^{-A(Q, n, L)T_{ion}} \right), \quad (3.17)$$

where $A(n, L)$ is given by Eq. (3.15), T_{det} is the time required to transit the 175.3 cm between the Rydberg target and the detector, and T_{ion} is the time in which the ion can ionize within the Stripper at a potential to be deflected into the CEM with the signal ions. T_{ion} is estimated to be the time in which the ion travels 0.6 cm. Figure 3.29 illustrates Eq. (3.17) for the 150 keV U^{6+} beam as a function of the auto-ionization rate. For very short lived auto-ionizable states the probability of surviving to the detector is very low. If the states are too long lived then the probability of detection decreases. States with auto-ionization rates on the order of $200,000 \text{ s}^{-1}$, i.e. lifetimes of $\sim 5 \text{ } \mu\text{s}$, have the highest probability of being detected and contributing to the background.

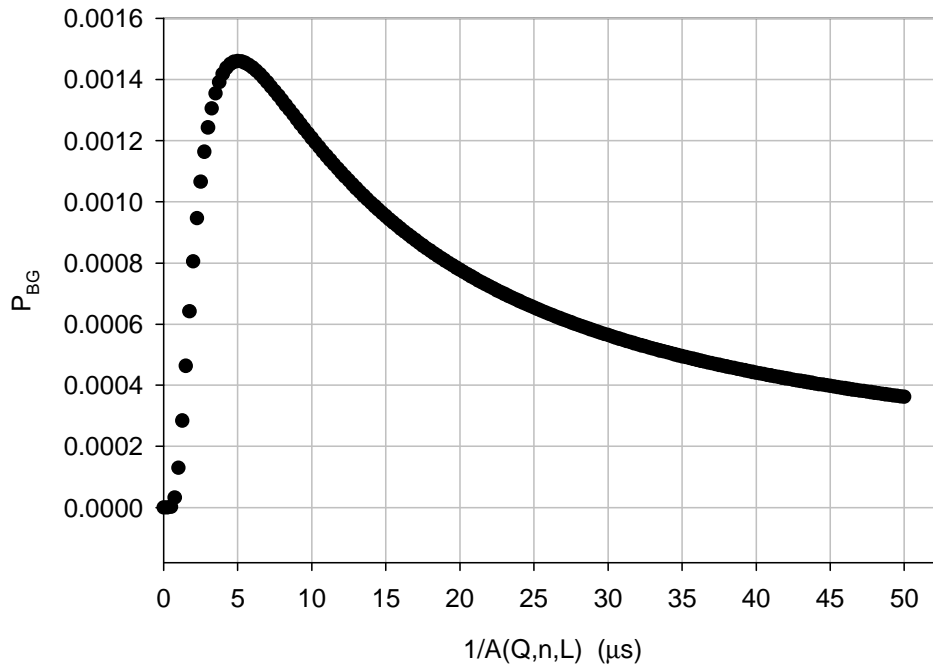


Figure 3.29: Probability of contributing to the background as a function of the auto-ionization rate.

The probability of an auto-ionizable Rydberg state contributing to the regenerated primary at the detector, P_{RP} , is given by the product of the probability of survival through the 15° charge selection magnet after the Rydberg target and the probability of auto-ionizing during the transit through the remainder of the apparatus to the deflection plates.

The probability P_{RP} is given by

$$P_{RP}(Q, n, L) = e^{-A(Q, n, L)T_{mag}} \left(1 - e^{-A(Q, n, L)T_{defl}} \right), \quad (3.18)$$

where T_{mag} is the time required to transit the 27.9 cm between the Rydberg target and the middle of the 15° magnet and T_{defl} is the time required to transit the 147.3 cm distance from the middle of the 15° magnet to the deflection plates in the detector. Figure 3.30 is a plot of Eq. (3.18) as a function of the auto-ionization rate. Again, if the states auto-ionize either too rapidly or slowly they will not contribute to the regenerated primary. Auto-ionizable states with rates on the order of $400,000 \text{ s}^{-1}$ have the highest probability of contributing to the regenerated primary.

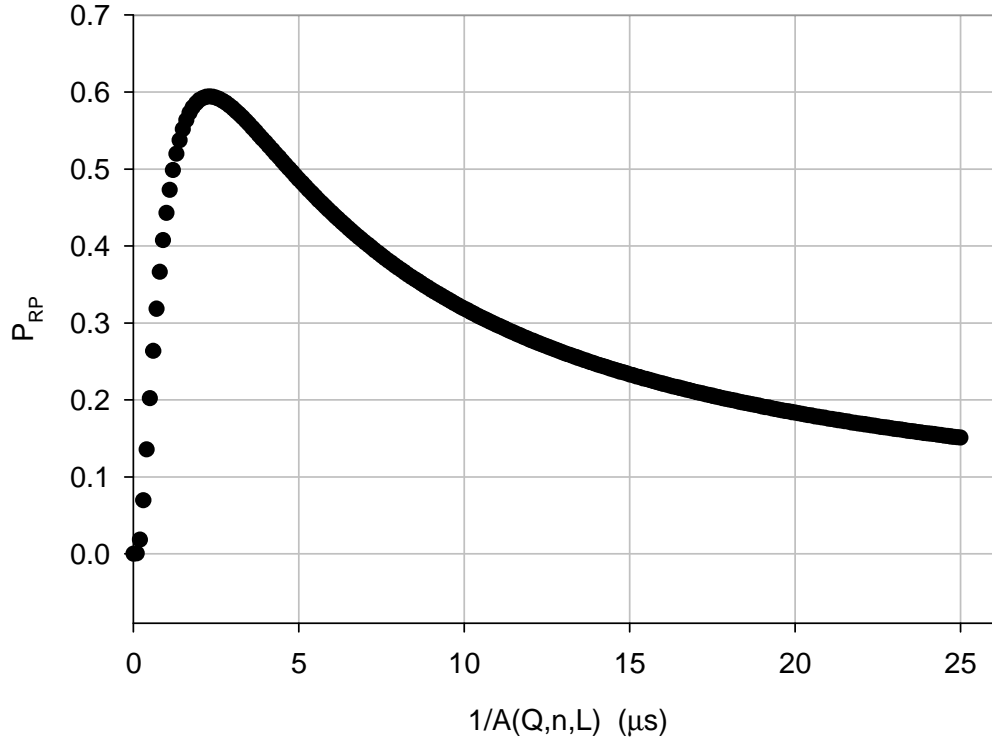


Figure 3.30: Probability curve of an auto-ionizing Rydberg state contributing to the regenerated primary beam as a function of the auto-ionization rate.

Once the probabilities for each (n, L) state in the entire capture distribution were computed the total amount of population predicted by CTMC that could be detected, M_{det} , is given by

$$M_{det} = \sum_n \sum_L \sigma(n, L) \cdot P_{det}(n, L), \quad (3.19)$$

and the population that could contribute to the size of the regenerated primary beam, M_{RP} , is given by

$$M_{RP} = \sum_n \sum_L \sigma(n, L) \cdot P_{RP}(n, L). \quad (3.20)$$

The ratio of the number of ions that contribute to the background per charge transfer from the Rydberg target can then be found by dividing Eq. (3.19) by the total capture cross section from CTMC, and is shown in column 3 of Table 3.11. This value can then be

compared with the observed ratio of the background count rate to the charge transfer from the Rydberg target count rate, shown in column 4 of Table 3.11. The predictions listed in Table 3.11 assume that the primary ion beam is entirely in metastable states. The predicted ratios of the background and regenerated primary to the total charge capture can be found from the ratio of Eq. (3.19) and Eq. (3.20) to the total capture cross-section and are listed in columns 3 and 5 of Table 3.11. This predicted ratio can be compared with the same ratios observed in the detector, which are listed in columns 4 and 6 of Table 3.11. Since the exact auto-ionization rate is unknown, the rate constant in Eq. (3.15) was adjusted up or down by a factor of 100, yielding the results shown in Table 3.12. The prediction is very insensitive to the precise value of the matrix element since there are always states available with the most detectable lifetime.

Table 3.11: Auto-ionization model comparison to observations. Column 2 lists the amount of background per charge transfer estimated using the model. Column 3 lists the observed background count rate to the charge transfer, reproduced from Table 5.8. Column 4 lists the estimated ratio of the regenerated primary to charge transfer and Column 5 lists the observed ratio of the regenerated primary to charge transfer from scan #11-103 for U^{6+} and #11-151 for Th^{4+} .

Beam	Target	Est. BG/CXRT	Obs. BG/CXRT	Est. RP/CXRT	Obs. RP/CXRT
150 keV U^{6+}	10F	2.4×10^{-4}	12.4×10^{-4}	110×10^{-3}	120×10^{-3} (#11-103)
100 keV Th^{4+}	10F	1.9×10^{-4}	3.4×10^{-4}	111×10^{-3}	0.83×10^{-3} (#11-151)

Table 3.12: Comparison of different predicted values for BG/CXRT and RP/CXRT after adjusting the Auto-ionization rate. The first two rows correspond with increasing the rate by a factor of 100 and the last two are decreasing the rate by a factor of 100. The observed values are reproduced from Table 3.11 for reference.

Rate adjustment	Beam	Est. BG/CXRT	Obs. BG/CXRT	Est. RP/CXRT	Obs. RP/CXRT
$\times 100$	150 keV U^{6+}	1.6×10^{-4}	12.4×10^{-4}	83×10^{-3}	120×10^{-3}
	100 keV Th^{4+}	0.9×10^{-4}	3.4×10^{-4}	63×10^{-3}	0.83×10^{-3}
$\div 100$	150 keV U^{6+}	1.8×10^{-4}	12.4×10^{-4}	73×10^{-3}	120×10^{-3}
	100 keV Th^{4+}	1.7×10^{-4}	3.4×10^{-4}	86×10^{-3}	0.83×10^{-3}

The model used in Table 3.11 represents the best guess as to what is occurring throughout the length of the apparatus generating the background in the detector. Comparing the predictions of the BG/CXRT and RP/CXRT to the observations in U^{6+} suggest that a very significant fraction of the U^{6+} beam is in metastable states and that the dominant source of background in the U^{6+} experiment is due to the auto-ionization of metastable Rydberg states. The observed ratio of the RP/CXRT for Th^{4+} is much less than the prediction listed in Table 3.11. This suggests that a much smaller fraction of the Th^{4+} beam is in metastable states. The observed BG/CXRT ratio for Th^{4+} is coincidentally similar to the ratio observed for U^{6+} , probably because other sources of background, e.g. collisional excitation into previously emptied levels or incomplete pre-ionization, are significant. The question that is left unanswered is why the metastable fraction appears to be so different for the two Rn-like ions, U^{6+} and Th^{4+} , in spite of the expected similarity in their excited states.

Chapter 4: Rydberg spectroscopy of Th IV

The Rn-like Th^{4+} ion is a closed shell ion that has a $6p^6 1S_0$ ground state configuration. The lowest excited state is a $6p^5 5f$ state with an excitation energy of approximately 17 eV [10]; however, no optical spectroscopy exists for this ion. The Th^{4+} ion is the most common charge state occurring in Thorium chemistry. The most important dynamic properties of this ion are the dipole and quadrupole polarizabilities, yet no direct measurements of these properties exist. These properties can be determined by careful measurement of the binding energies of very high angular momentum states of Th^{3+} using the long range polarization model, derived in Chapter 1.

4.1 Th^{3+} Rydberg Fine Structure observations

The fine structure pattern for the Th^{3+} ion is relatively simple because there is one eigenvalue for each value of L . For very high values of L the energy deviation from the hydrogenic energy of the state as a result of the long range interaction of the Rydberg electron with the ion core are small and the energy difference between adjacent Rydberg fine structure levels is small. Thus, transitions between these extremely high- L states are not resolved as transitions between individual values of angular momenta leading to a single large peak. As the angular momentum value L decreases the energy deviations of the Rydberg fine structure levels from the hydrogenic frequency of the transition

increases and the energy separation between adjacent states is increased, thus transitions between specific values of L are resolved in the spectrum.

The Th^{3+} Rydberg excitation spectra were observed by adjusting the intersection angle of the CO_2 laser with the ion beam in increments of 0.10° , resulting in incremental adjustments in the CO_2 laser Doppler-tuned frequency of approximately 45 MHz. At each step the CEM current synchronous with the chopping of the CO_2 laser was integrated and averaged by the computer over 15 seconds. Table 4.1 summarizes the Th^{3+} Rydberg transitions, CO_2 laser lines, beam velocity (relative to c), and tuned CO_2 frequency ranges used for the Th^{3+} Rydberg fine structure observations presented in this work.

Table 4.1: List of the transitions, CO_2 laser lines, and beam velocities used in the observation of the Th IV Rydberg fine structure. The first column lists the transitions used, the second column lists the hydrogenic energy of the Rydberg transition, the third column lists the CO_2 laser line used to excite the resonant transitions, and the fourth column provides the beam velocity relative to c . The last column gives the range of frequencies that the CO_2 laser was tuned over to observe the various fine structure patterns. The frequencies of the CO_2 lines are listed in Ref. [32].

Transition ($n - n'$)	E^0 (cm^{-1})	CO_2 Laser Transition	v/c	Tuned Frequency Range (cm^{-1})
(37, 7) – (76, 8)	978.5561	10R(24)	0.00096078(96)	978.7953 – 978.8710
37 – 73	953.0579	10P(10)	0.00096078(96)	953.0456 – 953.3424
38 – 79	934.5911	10P(30)	0.00096078(96)	934.5707 – 934.7519

The Th^{3+} transitions listed in Table 4.1 are shown in Figures 4.1, 4.2, and 4.3 that follow.

The single resolved transition between the (37, 7) – (76, 8) state was observed by averaging 60s per point due to the small size of the signal compared to the background.

The larger fine structure spectra shown in Figs. 3.2 and 3.3 represent 16 scans averaged together. In this way a total integration time per point of 240s was accumulated and a signal to noise on the unresolved L peak of ~ 950 for the 37 – 73 transition observations and ~ 550 for the 38 – 79 transition.

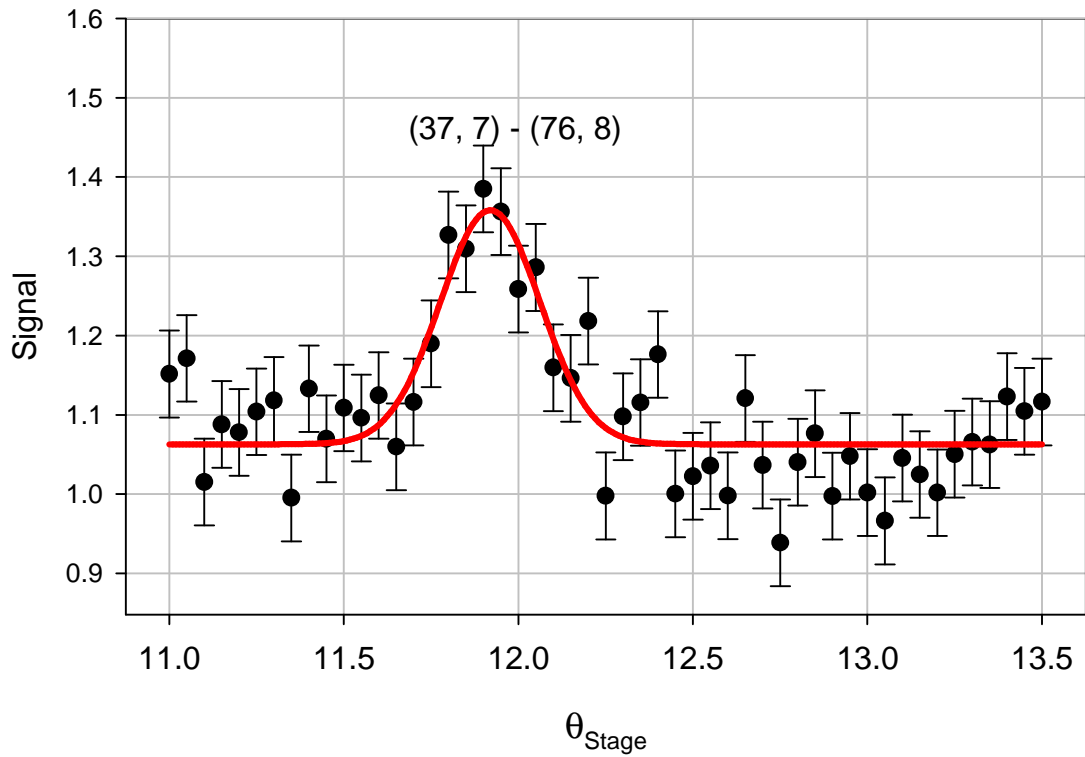


Figure 4.1: Observed $(37, 7) - (76, 8)$ transition in 100 keV Th^{3+} . The x-axis represents the angle recorded by the computer of the rotation stage that determines the angle of intersection the CO_2 laser beam with the Th^{3+} ion beam. The red line represents a 4 parameter Gaussian fit to the resolved signal used to determine angle center of the transition. The stage was incremented by 0.05° between each point.

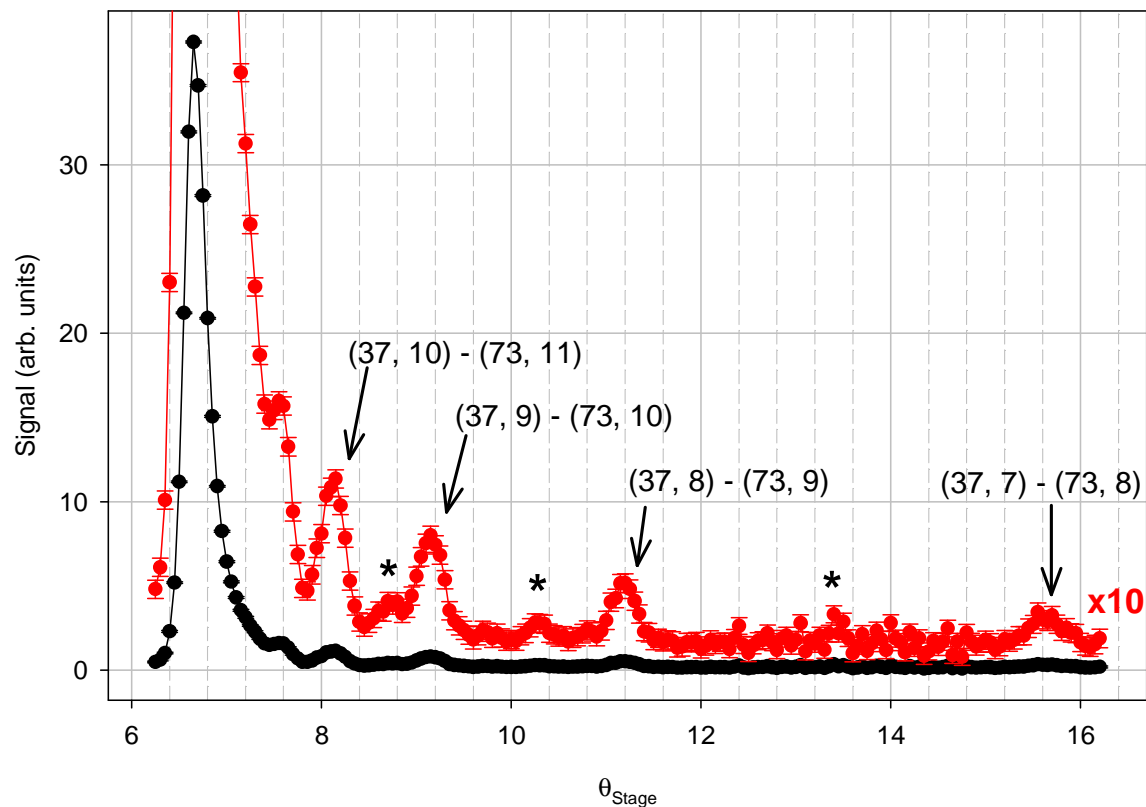


Figure 4.2: RESIS excitation spectrum of the $n = 37 - n' = 73$ transition in 100 keV Th^{3+} . The x-axis represents the stage angle recorded by the computer controlling the intersection angle of the CO_2 laser with the ion beam. The red points represent the data multiplied by a factor of 10 for clarity in viewing the resolved fine structure transitions. In 15s each transition, with the exception of the lowest L transition, was clearly visible at $\sim 2\%$ of the unresolved L amplitude. The stage was adjusted by 0.05° between each point. The spectrum shown in this figure is the average of 13 hours of integrated data. The much weaker $\Delta L = -1$ transitions are indicated with an asterisk.

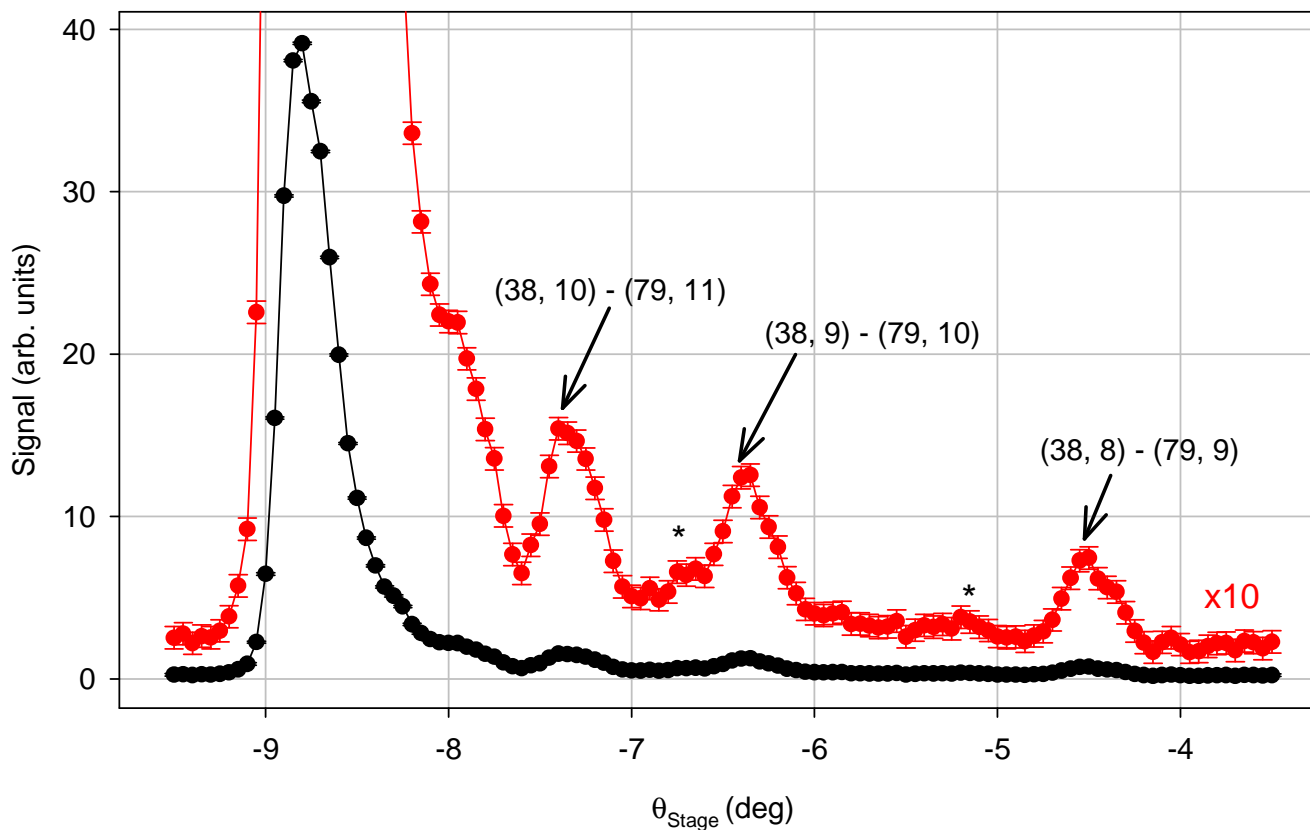


Figure 4.3: RESIS excitation spectrum of the 38 – 79 transition in 100 keV Th^{3+} . The x-axis represents the stage angle recorded by the computer controlling the intersection angle of the CO₂ laser with the ion beam. The red points represent the data multiplied by a factor of 10 for clarity in viewing the resolved fine structure transitions. The stage was adjusted by 0.05° between each point. The spectrum shown in this figure is the average of 8 hours of integrated data. The much weaker $\Delta L = -1$ transitions are indicated with asterisks in the figure.

Each of the identified resolved transitions in the preceding figures was individually fit to a four parameter Gaussian function to determine the center angle at which the resonant excitation occurred. An example of the fit is shown in Fig. 4.4 for the (37, 8) – (73, 9) transition for scan #12-134. Table 4.2 lists the fit determined center of the transition in $n = 37 - 76 \text{ Th}^{3+}$ that was studied, Table 4.3 lists the fit determined centers for the $n = 37 - 73$ transitions in Th^{3+} that were studied, and Table 4.4 lists the fit determined centers for the $n = 38 - 79$ transitions in Th^{3+} that were studied. RESIS transitions with an initial state with $L \geq 9$, where the weaker $\Delta L = -1$ transitions were not completely resolved from the dominant $\Delta L = +1$ transition, were fit to a superposition of two Gaussians. The relative strength of the $\Delta L = -1$ transition to the dominant $\Delta L = +1$ transition was fixed by a study of the more fully resolved transitions with $L = 8$. An example of the two Gaussian fit that was used to determine the relative amplitude of the $\Delta L = -1$ transition is shown for the (37, 8) – (73, 9) and (37, 8) – (73, 7) transition in Fig. 4.4. On average it was found that the $\Delta L = -1$ transition amplitude was 40% of the amplitude of the dominant $\Delta L = +1$ transition. The form of the fitting function for the two Gaussian fit for transitions with $L \geq 9$ was:

$$F(\theta_{stage}) = y_0 + 0.4Ae^{-\frac{1}{2}\left[\frac{(\theta_{stage}-\theta_0+\Delta\theta)}{b_1}\right]^2} + Ae^{-\frac{1}{2}\left[\frac{(\theta_{stage}-\theta_0)}{b_2}\right]^2}, \quad (4.1)$$

where y_0 is an arbitrary offset, A is the amplitude of the dominant $\Delta L = +1$ transition, θ_{stage} is the observed stage angle, θ_0 is the center stage angle of the transition, b_1 is the Gaussian width of the $\Delta L = -1$ transition, and b_2 is the Gaussian width of the $\Delta L = +1$ transition. The value of $\Delta\theta$ was determined by calculating the energy difference between

the $\Delta L = +1$ transition and the $\Delta L = -1$ transition using the long range polarization model, including relativistic and second order effects. Of course, in order to calculate the energy difference *a priori* knowledge of α_d , α_Q , and β_d is required. Initially these parameters were determined without fitting for the unresolved $\Delta L = -1$ transitions and initial estimates of the properties of the Th^{4+} ion core were determined. With these initial estimates the energy difference was calculated and the process of determining α_d , α_Q , and β_d was repeated. Improved values for these parameters were determined and the energy difference was refined yet again. This process was iterated until a consistent answer was achieved between iterations.

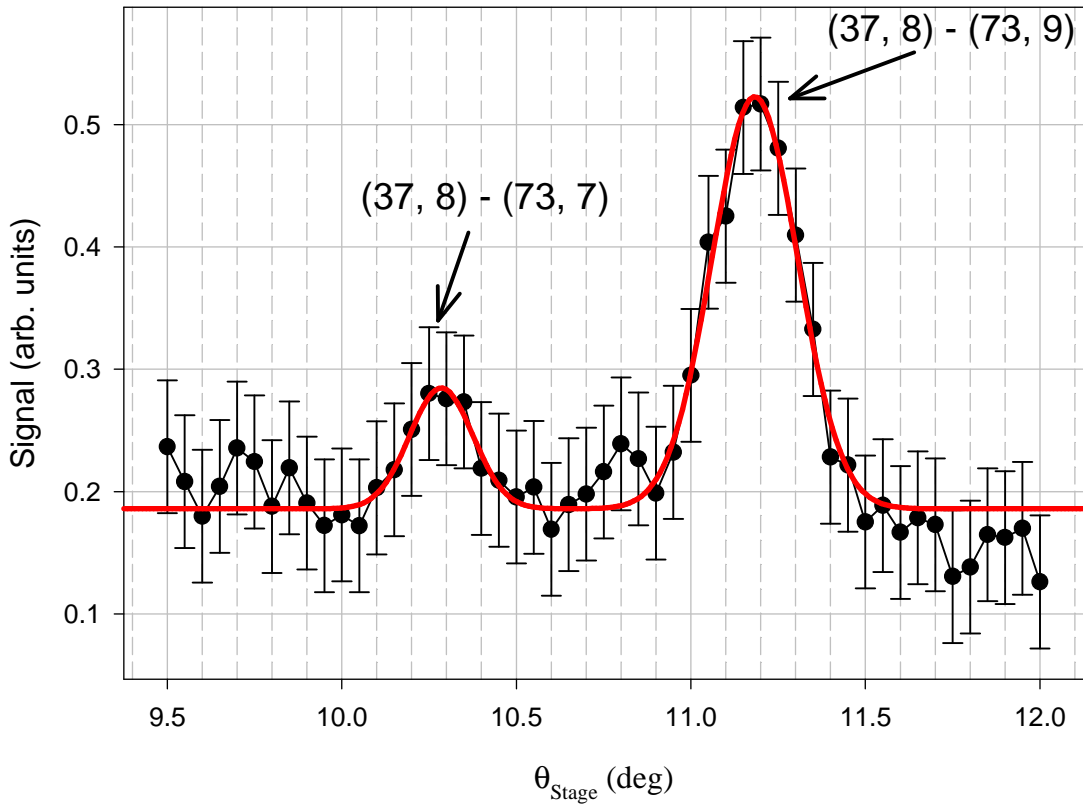


Figure 4.4: Example of the four parameter Gaussian fit to the (37, 8) – (73, 9) transition in Th^{3+} . Also shown is a similar fit of the weaker $\Delta L = -1$ transition.

Table 4.2: Individual fit results for 37 – 76 transition in Th³⁺.

Scan ID #	Fit Determined Transition center (37, 7) – (76, 8)
Average of 13-099, 099B, 099C, 099D, 099E, 100	12.048(32) ^o
Average of 13-113,114B,114C,114D	12.054(20) ^o
Average of 13-130, 130B, 130C, 130D	11.920(17) ^o

Table 4.3: Individual fit results for 37 – 73 transitions in Th³⁺.

Scan ID #	Fit Determined Transition Center			
	(37, 10) – (73, 11)*	(37, 9) – (73, 10)*	(37, 8) – (73, 9)	(37, 7) – (73, 8)
12-044	8.244(9) ^o	9.253(12) ^o	11.267(18) ^o	15.657(24) ^o
12-045	8.174(24) ^o	9.193(12) ^o	11.233(27) ^o	--
12-046	8.171(45) ^o	9.171(12) ^o	11.195(17) ^o	--
12-047	8.170(18) ^o	9.169(9) ^o	11.174(20) ^o	--
12-055	8.204(27) ^o	9.198(19) ^o	11.172(37) ^o	--
12-056	8.174(76) ^o	9.183(30) ^o	11.144(31) ^o	15.636(79) ^o
12-057	8.150(30) ^o	9.121(16) ^o	11.155(28) ^o	15.606(60) ^o
12-058	8.135(69) ^o	9.189(13) ^o	11.172(24) ^o	15.642(21) ^o
12-120	8.194(20) ^o	9.199(16) ^o	11.222(27) ^o	15.552(21) ^o
12-121	8.107(15) ^o	9.116(14) ^o	11.207(15) ^o	15.659(30) ^o
12-122	8.119(17) ^o	9.109(12) ^o	11.163(24) ^o	15.611(73) ^o
12-123	8.090(34) ^o	9.083(11) ^o	11.150(44) ^o	15.604(190) ^o
12-132	8.218(49) ^o	9.190(16) ^o	11.237(68) ^o	--
12-133	8.125(18) ^o	9.114(11) ^o	11.131(23) ^o	--
12-134	8.103(25) ^o	9.106(15) ^o	11.168(27) ^o	--
12-135	8.099(19) ^o	9.106(6) ^o	11.156(13) ^o	--

* Peak was fit as a composition of two Gaussians.

Table 4.4: Individual fit results for 38 – 79 transitions in Th³⁺.

Scan ID #	Fit Determined Transition Center		
	(38, 10) – (79, 11)*	(38, 9) – (79, 10)*	(38, 8) – (79, 9)
12-036	-7.213(26) ^o	-6.323(16) ^o	-4.419(43) ^o
12-037	-7.266(18) ^o	-6.301(25) ^o	-4.455(33) ^o
12-038	-7.215(41) ^o	-6.244(21) ^o	-4.398(40) ^o
12-039	-7.239(31) ^o	-6.261(16) ^o	-4.405(45) ^o
12-062	-7.321(20) ^o	-6.352(9) ^o	-4.484(42) ^o
12-063	-7.302(44) ^o	-6.361(12) ^o	-4.486(20) ^o
12-065	-7.329(52) ^o	-6.366(7) ^o	-4.491(49) ^o
12-066	-7.311(18) ^o	-6.370(9) ^o	-4.480(16) ^o
12-068B	-7.319(42) ^o	-6.418(18) ^o	--
12-074	-7.273(16) ^o	-6.319(10) ^o	--
12-074B	-7.272(17) ^o	-6.332(13) ^o	--
12-079	-7.317(50) ^o	-6.365(12) ^o	--
12-079B	-7.308(55) ^o	-6.357(13) ^o	--
12-113	-7.308(217) ^o	-6.353(41) ^o	-4.530(29) ^o
12-114	-7.341(145) ^o	-6.412(26) ^o	-4.583(68) ^o
12-115	-7.311(75) ^o	-6.392(32) ^o	-4.540(50) ^o
12-116	-7.324(143) ^o	-6.364(70) ^o	-4.534(73) ^o
12-127	-7.419(20) ^o	-6.484(18) ^o	-4.597(19) ^o
12-128	-7.362(57) ^o	-6.459(16) ^o	-4.590(25) ^o
12-129	-7.426(50) ^o	-6.471(15) ^o	-4.603(32) ^o
12-130	-7.332(63) ^o	-6.394(78) ^o	-4.475(64) ^o

* Peak was fit as a composition of two Gaussians.

Table 4.5: Average fitted centers of Th³⁺ resolved fine structure transitions. The internal error listed in Column 4 is the propagated random error of each fit to determine the transition peak center. The external error listed in Column 5 is the standard deviation of the mean. Column 6 lists the intersection angle of the CO2 laser with the ion beam. The error listed in column 6 is propagated from the larger of the internal or external errors, excluding the systematic error in θ_{\perp} . The systematic error arising from the error in θ_{\perp} is treated separately. The method of treatment is discussed later in this chapter with regards to the polarizability analysis of Th4+.

Transition	Number of Observations	Average center	Internal Error	External Error	θ_{Int}
(37, 7) – (76, 8)	3	12.007 ^o	0.041 ^o	0.044 ^o	67.926(88) ^o
(37, 10) – (73, 11)	16	8.155 ^o	0.009 ^o	0.012 ^o	75.850(24) ^o
(37, 9) – (73, 10)	16	9.162 ^o	0.005 ^o	0.013 ^o	73.836(26) ^o
(37, 8) – (73, 9)	16	11.187 ^o	0.008 ^o	0.009 ^o	69.786(18) ^o
(37, 7) – (73, 8)	8	15.621 ^o	0.029 ^o	0.012 ^o	60.918(58) ^o
(38, 10) – (79, 11)	18	-7.308 ^o	0.010 ^o	0.014 ^o	106.776(28) ^o
(38, 9) – (79, 10)	21	-6.369 ^o	0.008 ^o	0.012 ^o	104.898(24) ^o
(38, 8) – (79, 9)	16	-4.504 ^o	0.011 ^o	0.017 ^o	101.168(34) ^o

The determination of the average stage angle of the fitted line centers was performed this way so that any small variations in the CO₂ laser frequency or beam trajectory are averaged out in the final determination of the center frequency of the transitions. The resulting average of the fitted centers of the resolved fine structure transitions labeled in Figs. 4.1, 4.2 and 4.3 are given in Table 4.5.

Also shown in Table 4.5 are the intersection angles of the CO₂ laser with the ion beam. As described earlier the x-axis of the preceding figures is related to the intersection angle, θ_{int} , by an arbitrary offset θ_{\perp} . For a majority of the transitions in Table 4.5 $\theta_{\perp} = 1.08(1)^{\circ}$. The value of θ_{\perp} changed for the observations of the (37, 7) – (76, 7) as a result of a realignment of the LIR with the CO₂ laser. The new value of θ_{\perp} was determined by observing the shift of the high- L peak in Fig. 4.2. The average fit determined center of the unresolved L peak was $6.678(12)^{\circ}$ in Fig 4.2. Subsequent scans of this transition in the LIR after reassembling the beam line determined that the new center was at $6.565(25)^{\circ}$. This indicates that the value of θ_{\perp} has been changed from the earlier determination of by a similar amount due to the realignment of the LIR with the CO₂ laser. As a result $\theta_{\perp} = 0.97(3)^{\circ}$ was used in determining the θ_{int} for the (37,7) – (76,8) transition given in Table 4.5.

The Th³⁺ fine structure observations can be used in conjunction with the long range polarization model developed in Chapter 1 to extract the dipole and quadrupole polarizabilities of the Th⁴⁺ ion core. However, the determination of these parameters depends upon the proper identification of the transitions. The clear fine structure patterns shown in Figs 4.1, 4.2, and 4.3 are by themselves not enough to identify the transitions.

The resolved transitions can be identified in another fashion if a preliminary estimate of the dipole polarizability is known to within a factor of two. Such estimates could be obtained from the analysis of the lower- L Rydberg levels measured by other optical spectroscopy techniques. A unique challenge presented in the analysis of the Th^{3+} is that there is very little optical spectroscopy available for this highly ionized actinide ion. The highest n, L state known from the sparse spectroscopy is the 5g state [33] this state alone is not enough to determine an estimate of the polarizability to identify the lines by analysis of the lower- L Rydberg levels of the Th^{3+} ion. U. I. Safronova, *et al.* computed a polarizability of $\alpha_d = 7.75(39)$ a.u. [34] and suggest that this value is accurate to within 5% [35]. The value of the polarizability provided by Safronova was used to initially identify the lines. The energy of the 5g state and ionization energy of Th^{3+} by Klinkenberg [33] were used to confirm the identifications. The details of the identification of the L of the Rydberg states studied using the 5g state observed by Klinkenberg are described in the following section.

4.2 Dipole and Quadrupole Polarizabilities of Th^{4+}

Recall from Chapter 1 that it was asserted that the Rydberg fine structure pattern resulting from the long range interactions between the Rydberg electron and the positive ion core can be described by a model where the interaction between Rydberg electron and the positive ion core is treated as a perturbation to the non-relativistic Hamiltonian for the full system. The resulting long range polarization model can be used to extract some of the dynamic properties, *e.g.* the dipole and quadrupole polarizability, of the Th^{4+} ion core by careful measurement resulting fine structure pattern in Th^{3+} . As implied in Chapter 1,

the energy deviation from the hydrogenic energy of a Rydberg level is related to the properties of the ion core by the expectation value of an effective potential that is given by,

$$V_{eff} = -\frac{\alpha_d}{2r^4} - \frac{(\alpha_Q - 6\beta_d)}{2r^6} + \dots \quad (4.1)$$

for an ion with a 1S_0 ground state. The total energy of a Rydberg state including the small deviations due to V_{eff} , $E^{[1]}$, can be expressed as

$$E(n, L) = E^0(n) + E^{[1]}(n, L) + E^{Rel}(n, L) + E^{[2]}(n, L), \quad (4.2)$$

where the first term is the zeroth-order energy of a Rydberg level with principle quantum number n . Also included in Eq. (4.2) are two additional small contributions to the energy of a Rydberg level that are from the energy contributions arising from the relativistic correction to the kinetic energy of the electron, $E^{Rel}(n, L)$ and energy contributions arising from application of V_{eff} in second order, $E^{[2]}(n, L)$.

The correction to the Rydberg energy levels arising from the “p⁴” contributions to the kinetic energy of the electron is given in Chapter 1, Eq. (1.29). The application of V_{eff} in second order describes the mixing of different Rydberg series and the resulting contribution is denoted as $E^{[2]}$ in Eq. (4.1). The value of $E^{[2]}$ is computed using the analytical formula developed by Drake and Swainson [13]. The analytical formula including only the leading terms proportional to $(\alpha_d)^2$ is given in Chapter 1, Eq. (1.30). The evaluation of Eq. (1.30) depends upon knowledge of α_d . In the analysis of the Th³⁺ fine structure patterns an initial determination of the polarizability of Th⁴⁺ was found by fitting the resulting data patterns, described below, without any second order energy contributions. Once an initial estimate for α_d was determined the $E^{[2]}$ contributions to

each level were then computed and the analysis determining α_d was repeated. The process of computing $E^{[2]}$ and then re-determining α_d was iterated until a consistent value of α_d was determined.

The difference in energy of a transition between Rydberg levels from the hydrogenic energy of the transition, ΔE^{Obs} , can be expressed as

$$\begin{aligned}\Delta E^{\text{Obs}}(n, L - n', L') &= [E^{[1]}(n', L') + E^{[2]}(n', L') + E^{\text{Rel}}(n', L')] \\ &\quad - [E^{[1]}(n, L) + E^{[2]}(n, L) + E^{\text{Rel}}(n, L)] \quad , \\ &= \Delta E^{[1]} + \Delta E^{[2]} + \Delta E^{\text{Rel}}\end{aligned}\quad (4.3)$$

where the notation $(n, L - n', L')$ is suppressed for clarity in the last line and in the following equations. In order to simplify the analysis the dominant contribution to the energy deviation, $\Delta E^{[1]}$, is isolated by calculation and subtracting the small contributions arising from E^{rel} and $E^{[2]}$, yielding:

$$\Delta E^{[1]} = \Delta E^{\text{Obs}} - \Delta E^{[2]} - \Delta E^{\text{Rel}} \quad , \quad (4.4)$$

where

$$\Delta E^{[1]} = \frac{\alpha_d}{2} \Delta \langle r^{-4} \rangle + \frac{(\alpha_Q - 6\beta_d)}{2} \Delta \langle r^{-6} \rangle \quad , \quad (4.5)$$

The term ΔE^{Obs} in Eq. (4.4) is obtained from the observed Th^{3+} spectra by

$$\Delta E^{\text{Obs}} = \nu'_L - \Delta E^0 - \Delta E^{\text{Stark}}(n', L') \quad (4.6)$$

where ν'_L is the Doppler tuned laser frequency determined by Eq. (2.1) at the fitted center. Also shown in Eq. (4.6) is a term, ΔE^{Stark} , which is a calculated correction to the transition energy due to the Stark shift of the upper state of the transition.

The stray electric field responsible for the Stark shift of the upper state was determined by analyzing the variation in widths of the resolved Th^{3+} fine structure

transitions as a function of L . The observed widths of the transitions determined from fits of the data are listed in Table 4.6.

Table 4.6: Average width of the resolved RESIS transitions. This width can be combined with a parametric analysis of the width of the simulated RESIS line-shape as a function of stray electric field to determine an estimate for the magnitude of the stray field present in the LIR and corresponding corrections to the observed energies of the transitions, if any is needed.

Transition	Average Width (MHz)
(37, 9) – (73, 10)	267(9)
(37, 8) – (73, 9)	235(16)
(37, 7) – (73, 8)	239(60)
(38, 9) – (79, 10)	251(13)
(38, 8) – (79, 9)	216(25)

The effect of the stray electric field was then estimated by diagonalizing the Stark Hamiltonian and simulating the expected RESIS transition line shape. The line shape was simulated as a composite of Gaussian line shapes for the m states involved in a transition with a given upper state angular momentum L' . The zero electric field line width is estimated to be 213 MHz from the quadrature sum of homogeneous and inhomogeneous sources of line width. A plot of the FWHM of the simulated composite line shape of the 37 – 73 transitions listed in Table 4.6 as a function of electric field is shown in Fig. 4.5.

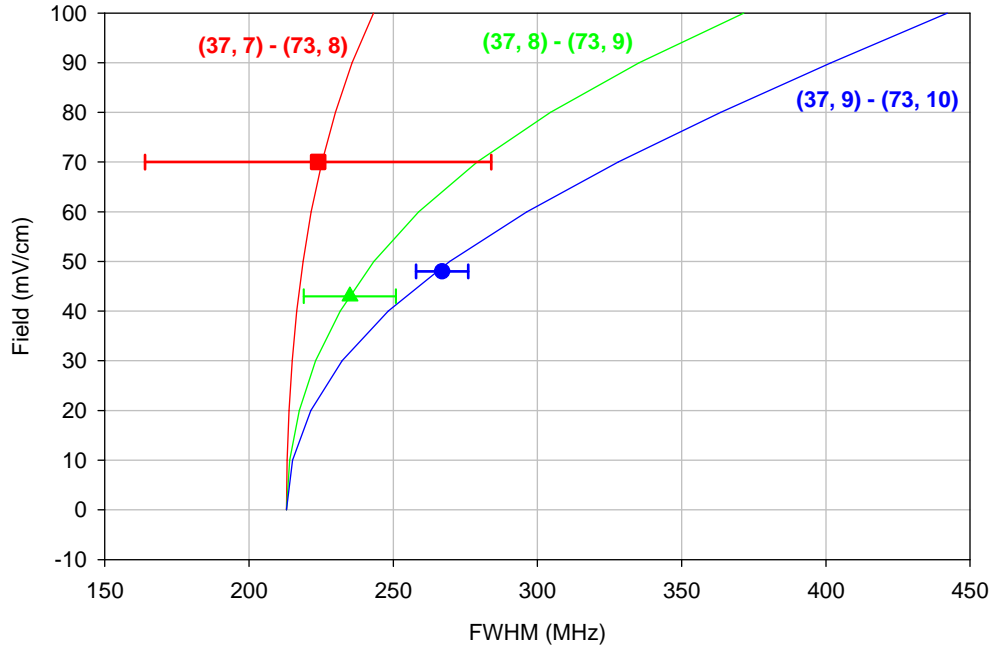


Figure 4.5: Parametric study of the simulated width of the RESIS transitions as a function of stray electric field. The red, green, and blue lines correspond with the simulated transition width as a function of stray electric field for the transitions to the $L = 8, 9,$ and 10 upper states respectively. The red square, green triangle, and blue circle are the observed widths of the transitions from Table 4.6. From the plot it was concluded that the stray electric field was $0.045(10)$ V/cm.

The stray electric field present in the LIR was determined to be $0.045(10)$ V/cm for the transitions between $n = 37 - n' = 73$. Using the same method, a stray electric field of $0.030(10)$ V/cm for the transitions between $n = 38 - n' = 79$ was determined. The stray field present in the LIR at the time of observation of the $(37, 7) - (76, 8)$ transition was assumed to be $0.060(10)$ V/cm from observed line widths of $37 - 73$ transitions observed on the same day. The value of ΔE^{Stark} was then determined by the shift in the fitted simulated line center from the assumed zero field line center and comparing the simulated position with the simulated position at the stray field indicated by the parametric study of the width of the RESIS transition. The observed transition energies along with the small correction due to Stark shifting of the upper state are shown in Table 4.7. For the Th^{3+} Rydberg states studied here the Stark shift corrections are nearly

negligible. The final column in Table 4.7 is the zero field energy of the transition between Rydberg levels that can be used to determine the dipole and quadrupole polarizabilities of the Th^{4+} ion core.

Table 4.7: Observed zero field Rydberg fine structure transition energies in Th^{3+} . The first two columns are reproduced from Table 3.2 for reference. The third column is the deviation from hydrogenic that is implied by θ_{Int} . The fourth column is the Stark shift of the upper state of the transition and the last column is the zero field energy of the transition.

Transition	θ_{Int}	$\nu'_L - \Delta E^0$ (MHz)	ΔE^{Stark} (MHz)	ΔE^{Obs} (MHz)
(37, 7) – (76, 8)	67.926(88) $^\circ$	8094(39)	-7(2)	8101(39)
(37, 10) – (73, 11)	75.850(24) $^\circ$	1415(11)	1(1)	1414(11)
(37, 9) – (73, 10)	73.836(26) $^\circ$	2341(11)	2(1)	2339(11)
(37, 8) – (73, 9)	69.786(18) $^\circ$	4189(8)	1(1)	4188(8)
(37, 7) – (73, 8)	60.918(58) $^\circ$	8046(24)	-3(2)	8049(24)
(38, 10) – (79, 11)	106.776(28) $^\circ$	1335(13)	1(1)	1334(13)
(38, 9) – (79, 10)	104.898(24) $^\circ$	2186(12)	1(1)	2185(12)
(38, 8) – (79, 9)	101.168(34) $^\circ$	3892(16)	1(1)	3891(16)

With the determination of the zero field energies of the transition between different high- L states in Th^{3+} the expectation value of V_{eff} can be isolated by subtracting off the contributions shown in Eq. (4.4). Listed in Table 4.8 are the calculated contributions to the energy of the observed transition from $E^{[2]}$ and E^{Rel} to the observed fine structure energies. The final column of Table 4.8 is then the expectation value of V_{eff} .

Table 4.8: List of the small corrections applied to determine the $E^{[1]}$.

Transition (n, L) – (n', L')	ΔE^{obs} (MHz)	$\Delta E^{[2]}$ (MHz)	ΔE^{rel} (MHz)	$\Delta E^{[1]}$ (MHz)
(37, 7) – (76, 8)	8101(39)	38.626(365)	89.1	7973(39)
(37, 10) – (73, 11)	1414(11)	0.876(14)	57.5	1356(11)
(37, 9) – (73, 10)	2339(11)	2.695(43)	65.5	2271(12)
(37, 8) – (73, 9)	4188(8)	9.403(149)	75.3	4103(8)
(37, 7) – (73, 8)	8049(24)	38.479(610)	87.7	7923(24)
(38, 10) – (79, 11)	1334(13)	0.816(13)	54.7	1278(13)
(38, 9) – (79, 10)	2185(12)	2.508(40)	62.1	2120(11)
(38, 8) – (79, 9)	3891(16)	8.739(139)	71.3	3811(16)

Once the first order energies in V_{eff} are known it is convenient to scale these energies by $\Delta\langle r^{-4} \rangle$. Scaling the energies in this manner is expected to remove most of the variation with n and L . Eq. (4.5) is then rewritten as

$$\frac{\Delta E^{(1)}}{\Delta\langle r^{-4} \rangle} = \frac{\alpha_d}{2} + \frac{\alpha_Q - 6\beta_d}{2} \frac{\Delta\langle r^{-6} \rangle}{\Delta\langle r^{-4} \rangle} + \dots = A_4 + A_6 \frac{\Delta\langle r^{-6} \rangle}{\Delta\langle r^{-4} \rangle} + \dots \quad (4.7)$$

By plotting the scaled energies as a function of $\frac{\Delta\langle r^{-6} \rangle}{\Delta\langle r^{-4} \rangle}$ values of some of the properties of the ion core can be easily determined from the intercept, A_4 , and slope, A_6 , of fit of the data pattern to Eq. (4.7). Such a plot of the scaled energies listed in Table 4.9 is shown in Figure 4.6.

Table 4.9: First order energies and matrix elements used in determining the polarizability of the Th^{4+} ion. Columns 1 and 2 are reproduced from Table 4.1 for reference. Column 5 and 6 list the scaled matrix elements and scaled first order energies. Not included in the error bars in column 6 are the errors arising from the systematic errors in β and θ_L .

Transition (n, L) – (n', L')	$\Delta E^{(1)}$ ($\times 10^{-6}$ a.u.)	$\Delta\langle r^{-4} \rangle$ ($\times 10^{-7}$ a.u.)	$\Delta\langle r^{-6} \rangle$ ($\times 10^{-10}$ a.u.)	$\frac{\Delta\langle r^{-6} \rangle}{\Delta\langle r^{-4} \rangle}$	$\frac{\Delta E^{(1)}}{\Delta\langle r^{-4} \rangle}$
(37, 7) – (76, 8)	1.2118(59)	3.02261	50.2360	0.0166	4.009(20)
(37, 10) – (73, 11)	0.2061(17)	0.53556	2.1419	0.0040	3.848(31)
(37, 9) – (73, 10)	0.3451(18)	0.89399	5.4568	0.0061	3.861(19)
(37, 8) – (73, 9)	0.6236(12)	1.57944	15.4452	0.0098	3.949(8)
(37, 7) – (73, 8)	1.2042(36)	2.99704	49.9890	0.0167	4.018(12)
(38, 10) – (79, 11)	0.1942(20)	0.50169	2.0028	0.0040	3.873(40)
(38, 9) – (79, 10)	0.3222(17)	0.83666	5.0947	0.0061	3.852(22)
(38, 8) – (79, 9)	0.5792(24)	1.47662	14.3975	0.0098	3.923(17)

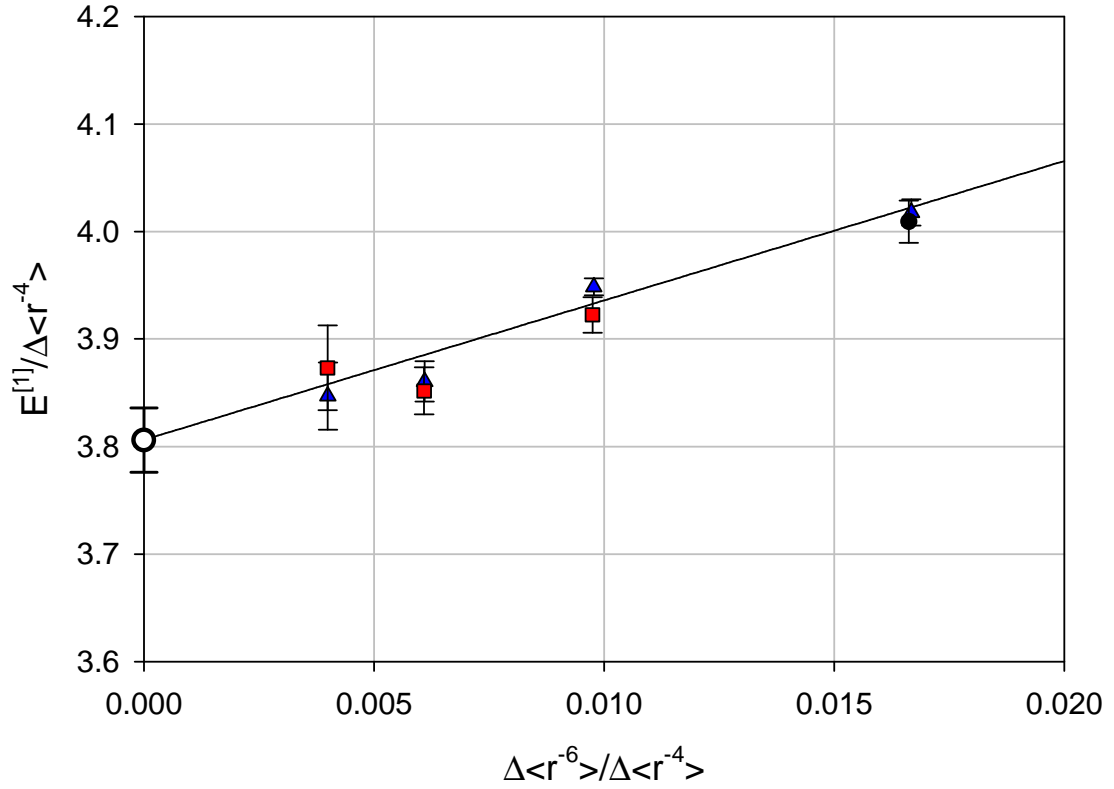


Figure 4.6: Scaled polarizability plot for Th^{4+} . The red points correspond to transitions between $n = 38 - n' = 79$ and the blue points correspond to transitions between $n = 37 - n' = 73$ in $\text{Th}3+$. The black point represents the scaled energy of the $(37, 7) - (76, 8)$ transition in $\text{Th}3+$. The black line represents the least squares fit of all the points to the long range polarization model where the intercept and slope can be used to determine some of the properties of the $\text{Th}4+$ ion. The intercept determined by the fit is shown as the open circle on the y-axis. The energies and matrix elements were converted to atomic units.

The trend of the scaled energies in Fig. 4.6 is completely consistent with the linear trend suggested by Eq. (4.7) if higher order terms in V_{eff} are negligible. A least squares linear fit of the data pattern in Table 4.2 to Eq. (4.7) determined the fit parameters

$$A_4 = 3.806(29)$$

$$A_6 = 13.0(1.9).$$

The value in the parenthesis is the error of the last two digits in the answer and is the combination of the random error in the determined energy intervals of the fine structure

determined from the Gaussian fits of the line centers and the errors representing the uncertainty in β and θ_{\perp} . This systematic error contribution is obtained by adjusting the values of β and θ_{\perp} separately by one standard deviation, recalculating the scaled first order energies, and refitting the resulting pattern. The resulting changes to the fitted parameters from the values above is a measure of the systematic error due to σ_{β} and $\sigma_{\theta_{\perp}}$. These changes were added in quadrature to the fit errors to determine the total error. The intercept and slope determined by fitting the scaled energies yields a determination of the dipole polarizability of Th^{4+} :

$$\alpha_d = 2A_4 = 7.61(6) \text{ a.u.}$$

The quadrupole polarizability can be determined if an approximate value of β_d is known. Recent theoretical estimates of β_d , listed below in Table 4.10, have been provided by M. S. Safronova [35].

Table 4.10: Theoretical estimates of β_d provided by Safronova [35]. The two values provided were computed using a Relativistic Random Phase Approximation (RRPA) model and a Dirac-Hartree-Fock (DHF) model of the ion.

Theoretical Model	β_d (a.u.)
RRPA	2.97
DHF	3.21

Taking $\beta_d = 3.1(2)$ a.u. then allows for an estimate of the quadrupole polarizability of Th^{4+} from the parameter A_6 determined from the fit:

$$\alpha_Q = 2A_6 - 6\beta_d = 26(4) - 18.6(1.2) = 45(4) \text{ a.u.}$$

Although this value of α_Q is in disagreement with the value of 29 a.u. provided by Safronova [35], both the theoretical and experimentally determined values of α_Q are large. A large value of α_Q is probably expected since the lowest lying excited states of Th^{4+} are quadrupole allowed $6p^55f$ levels.

The preceding analysis of the polarizability of the Th^{4+} ion from the Rydberg spectroscopy of the high angular momentum states of Th^{3+} has used the assumed identifications that were first presented in Figs. 4.1, 4.2, and 4.3. Should the value of L in the identified transitions change by ± 1 unit the polarization model can still be applied and the value by the dipole polarizability of Th^{4+} determined in the analysis will be changed by 40%. Figure 4.7 below shows a scaled energy plot, analogous to Fig. 4.6, with different choices for the value of L for the resolved transitions.

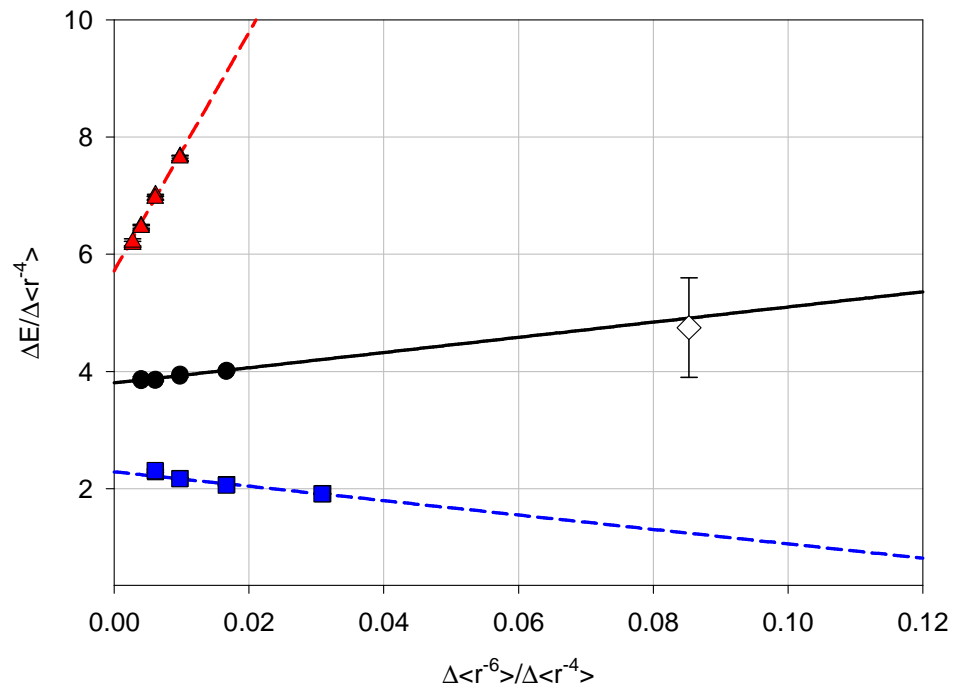


Figure 4.7: Scaled energy plot with various choices of L for the resolved transitions. The red points correspond to the value of L being increased by 1 unit in the identifications used throughout this chapter and blue correspond with L being decreased by 1 unit. The lines represent the fits of the corresponding points to the long range polarization model. The open diamond represents the scaled energy of the 5g state observed by Klinkenberg [33].

In Fig. 4.7 the red points correspond to an increase by 1 unit in the L value of the observed transitions and the blue points correspond to a decrease by 1 unit in the L value.

All three cases are consistent with the long range polarization model, but each have

widely varying slopes and intercepts. The observed energy of the 5g state, $E(5g)$, at $159,379 \text{ cm}^{-1}$ [33] and the determined ionization energy, E_I , of $231,065(242) \text{ cm}^{-1}$ [33] of Th^{3+} can provide a clue to the correct choice of identification for the transitions observed in this work. Although the long range polarization model may not apply to the 5g as accurately as the states studied in this work, the ionization energy and location of this state allow a point to be placed on the scaled energy plot according to

$$\begin{aligned} E^{[1]}(5g) &= E^{Obs}(5g) - E_I + \frac{Ryd_M}{5^2} - E^{[2]}(5g) \\ &= 159379 \text{ cm}^{-1} - 231065(242) \text{ cm}^{-1} + 70232 \text{ cm}^{-1} + 96 \text{ cm}^{-1} \cdot \\ &= -1358(242) \text{ cm}^{-1} \end{aligned} \quad (4.8)$$

As can be seen in Fig. 4.7 the location of the scaled first order energy from Eq. (4.8) of the 5g state is completely consistent with the initial identifications of the transitions; the other L identifications of the transitions, those with $L \pm 1$ unit, are vastly discrepant with the scaled energy of the 5g level. Thus, the location of the 5g state on the scaled plot in Fig. 4.7 confirms the initial identifications used throughout this chapter as being the correct identifications for the transitions.

4.3 Th^{3+} Conclusions

The dipole polarizability of the Fr-like Th^{4+} ion determined by this work is $7.61(6)$ a.u. A non-relativistic Hartree-Fock calculation determined a value of 10.26 a.u. [36]. A relativistic Dirac-Hartree-Fock model determined a value of 8.96 a.u. [37]. The value of 7.75 a.u. determined by U. I. Safronova, *et al.* using the Relativistic Random Phase Approximation (RRPA) method [34] is estimated to be good to within 5% [35]. Another relativistic estimation method, the Relativistic Coupled Cluster method including Single, Double, and partial Triple excitations (RCCSD(T)), carried out by Borschevsky

and Schwerdtfeger [38] estimates a value of 7.699 a.u. All but the Fraga et. al. [36] result are fully relativistic calculations. The theoretical values and corresponding comparison with the value for the dipole polarizability determined by this research are summarized in Table 4.11.

Also summarized in the table are the estimates for the quadrupole polarizability and first non-adiabatic contribution to the dipole polarizability that were obtained in Chapter 3. Safronova [35] has recently provided estimates for the value of β_d of 2.97 a.u. using the RRPA model and 3.21 a.u. using a Dirac-Hartree-Fock model. Taking $\beta_d \approx 3.1(2)$ a.u. and the simple interpretation of the slope the quadrupole polarizability of Th^{4+} is estimated to be 45(4) a.u. This value is inconsistent with the value of 29 a.u. computed by Safronova [35]. A possible cause for this is that the higher order non-adiabatic or adiabatic terms in the expansion of the long range effective potential proportional to r^{-8} could be contributing significantly and altering the apparent slope in Fig. 4.5. Such effects were seen in the microwave spectroscopy of the fine structure energies of ions with Si^{2+} [39] and Ba^{2+} [40] ion cores. The resolution of the fine structure energies determined in this work is too low to show these higher order effects. Future work investigating the fine structure energies of Th^{3+} using microwave spectroscopy could clarify this matter.

Table 4.11: Summary of the dynamic properties of the Th^{4+} ion determined by Rydberg spectroscopy of high-L Rydberg states of Th^{3+} . Also provided are a summary of the existing theoretical estimates where they exist and comparison of the theoretical value to the experimentally determined value.

Th^{4+} Core Property	Experimentally determined value (a.u.)	Theoretically Determined value (a.u.)	Comparison of Theory to Experiment
		10.26 ^a	1.348(11)
α_d	7.61(6)	8.96 ^b	1.177(9)
		7.75 ^c	1.018(8)
		7.699 ^d	1.012(8)
$\alpha_Q - 6\beta_d$	26(4)	--	--
β_d	--	3.1(2) ^e	--
α_Q	45(4)	29 ^e	0.64(6)

^a SCHF: Fraga, Karwowski, and Saxena [36]

^b DHF: Derevianko [37]

^c RRP: Safronova, Johnson, Safronova [34]

^d RCCSD(T): Borschevsky and Schwerdtfeger [38]

^e RRP and DHF: Safronova [35]

Chapter 5: Rydberg Spectroscopy of U VI

5.1 Spectroscopy of High- L Rydberg states of U VI

The high- L Rydberg fine structure of U^{5+} was observed using the same method used for Th^{3+} . Table 5.1 summarizes the U^{5+} Rydberg transitions, the final nF state of the Rydberg target that was used, the CO_2 laser line, beam velocity (relative to c), and tuned CO_2 frequency ranges used for the U^{5+} Rydberg fine structure observations presented in this chapter. Unfortunately, these observations have not yet yielded a conclusive result for the polarizability of U^{6+} .

Table 5.1: Summary of the various U^{5+} transitions studied in this work. The first column lists the U^{5+} transition observed, the second column lists the final state of the Rydberg target, and the third column lists the hydrogenic energy of the transition listed in the first column. The fourth column lists the CO_2 laser line used to observe the transition, the frequencies of the CO_2 lines are listed in Ref. [32]. The fifth column provides the beam velocity relative to c . The last column gives the range of frequencies that the CO_2 laser was tuned over to observe the various fine structure patterns.

U^{5+} Transition	Rydberg Target (nF)	E^0 (cm^{-1})	CO_2 laser transition	v/c	Tuned Laser Frequency Range (cm^{-1})
53 – 93	10F	949.6226	10P(14)	0.0011615(12)	949.6091 – 949.7453
53 – 93	8F	949.6226	10P(14)	0.0011615(12)	949.5963 – 949.6915
55 – 109	10F	973.4532	10R(16)	0.0009159(9)	973.4139 – 973.5653

The following figures, Figs. 5.1, 5.2, and 5.3, show the spectra observed when the CO_2 laser is tuned through the frequency ranges listed in Table 5.1. They represent the normalized weighted averages of many individual scans over the frequency ranges listed in Table 5.1 in order to achieve the best possible signal to noise. The noise is measured as the scatter of the y-channel recorded by the lock-in amplifier from a straight line in a

region with no or little signal. The weight of the individual runs in the weighted average was taken to be the inverse square of this noise measurement. The signals were normalized so that the amplitude of the high- L signal would be one in all cases, the normalization factor was determined by a 3 parameter Gaussian fit to the high- L signal.

Figure 5.1 is the weighted normalized average of 22 individual scans of the U VI 53 – 93 transition with a 10F Rydberg target final state, the beam energy was 150 keV during the acquisition of this data. The scans that were averaged together are in Book 12 pages 117 through 144. In each run the signal at a given stage angle was collected and averaged by the computer for 30 seconds. The combined average then represents a total collection time of 660 seconds per point (11 minutes). The signal to noise of the high- L peak ~ 1100 in this combined average. The blue lines indicate the calculated positions of individual excitations of $L = 11, 10,$ and 9 levels if $\alpha_d = 5.05$ a.u. The green line indicates 1% of the high- L signal. There is a suggestion of a signal corresponding to the excitation of the (53,11) – (93, 12) transition of approximately 0.2% of the high- L signal, but no consistent pattern suggesting lower L signals.

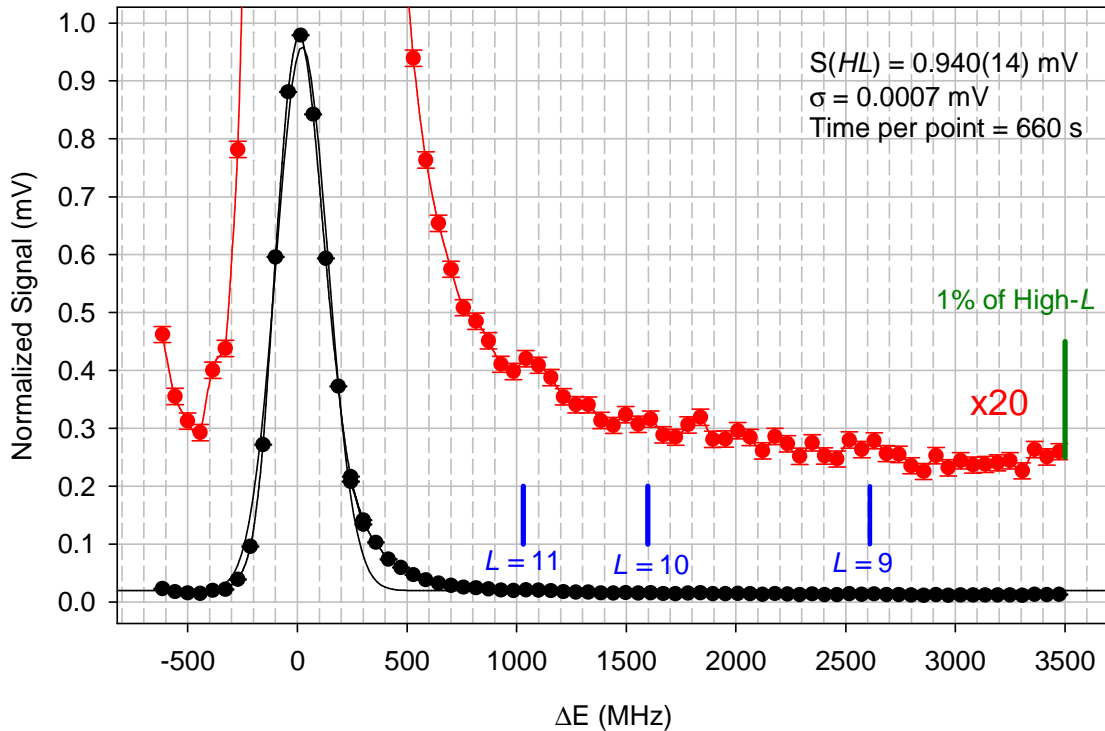


Figure 5.1: RESIS excitation spectrum of U^{5+} 53 – 93 Rydberg fine structure using the 10F Rydberg target. The x-axis represents the difference between the Doppler tuned CO_2 laser frequency and the hydrogenic frequency of the U^{5+} 53 – 93 transition. The red points represent the data multiplied by a factor of 20 for clarity in viewing the resolved fine structure transitions. In a total integration time of 660s any significantly resolved RESIS transitions are not visible even at the 0.5% level. The green line at 3500 MHz represents 1% of the high- L signal size in the 20x magnified data. The blue lines super imposed on the graph represent the calculated positions of the dominant (53, L) – (93, $L+1$) transitions assuming $\alpha_l = 5.05$ a.u.

Figure 5.2 is the weighted normalized average of 12 individual runs, from Book 14 pages 61 through 72, of the 53 – 93 transition in U VI with an 8F Rydberg target state, the beam energy during this series of scans was 150 keV. In each run the signal at a given stage angle was collected and averaged by the computer over a 15 second time period. The combined average then represents a total collection time of 180 seconds per point (3 minutes). The signal to noise of the high- L peak ~ 190 in this combined average. Again the blue lines indicate the calculated positions of excitations and the length of the green line shows 1% of the high- L signal. Again, there is a suggestion of a signal near

the expected position of the (53, 11) – (93, 12) transition. In this case, due to the lower signal to noise this signal could be as large as several percent of the high- L . However, there is no sign of lower L signals that could confirm a pattern.

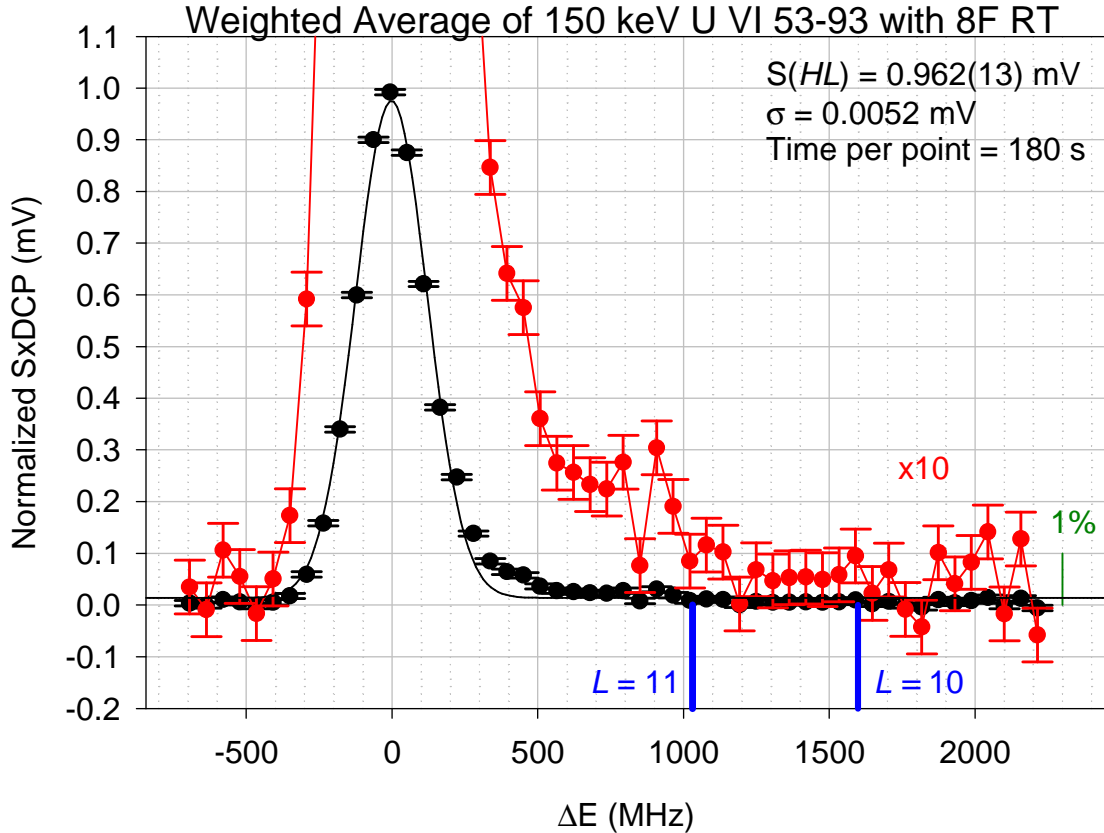


Figure 5.2: RESIS excitation spectrum of 150 keV U^{5+} 53 – 93 Rydberg fine structure using the 8F Rydberg target. The x-axis represents the difference between the Doppler tuned CO_2 laser frequency and the hydrogenic frequency of the U^{5+} 53 – 93 transition.. The red points represent the data multiplied by a factor of 10 for clarity in viewing the small resolved fine structure transitions. The green line at 2300 MHz represents 1% of the high- L signal size in the 10x magnified data. The blue lines super imposed on the graph represent the calculated positions of the dominant (53, L) – (93, $L+1$) transitions assuming $\alpha_d = 5.05$ a.u.

Figure 5.3 is the weighted normalized average of 28 individual runs, from pages 78 through 113 in Book 14, of the 55 – 109 transition in U VI with an 10F Rydberg target state between -700 MHz and 3500 MHz with an additional 55 scans, from page 130 to 132 in Book 14, between 2200 MHz and 2700 MHz. During this particular series of

scans through the transition the beam energy was 93 keV. In each run the signal at a given stage angle was collected and averaged by the computer over a 15 second time period. The combined average then represents a total collection time of 420 seconds per point (7 minutes) between -700 and 3500 MHz. The region between 2200 MHz and 2700 MHz had a total collection time of 1245 seconds per point (~21 minutes). The signal to noise of the high- L peak ~460 in the region -700 to 3500 MHz, the 2200 MHz to 2700 MHz region has an estimated high- L signal to noise of ~1370. The blue and green lines have the same meaning as in Figs. 5.1 and 5.2. Again, there is a suggestion of a (55, 11) – (109, 12) excitation which could be as large as 1% of the high- L signal but no consistent pattern including lower L excitations is observed.

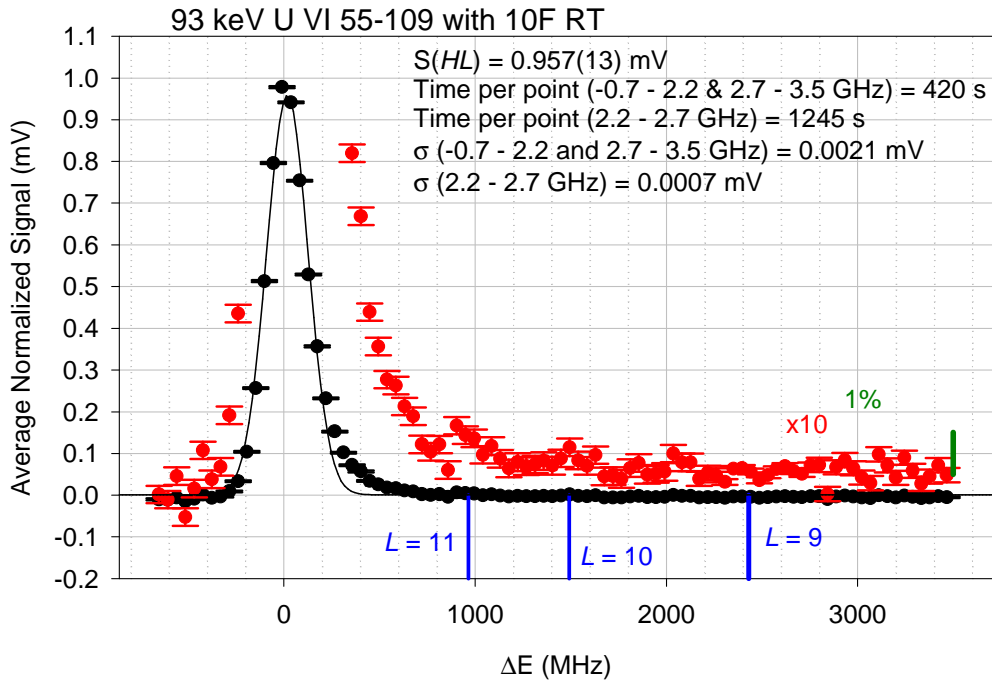


Figure 5.3: RESIS excitation spectrum of 93 keV U^{5+} 55 – 109 Rydberg fine structure using the 8F Rydberg target. The x-axis represents the difference between the Doppler tuned CO_2 laser frequency and the hydrogenic frequency of the U^{5+} 55 – 109 transition. The red points represent the data multiplied by a factor of 10 and a slight DC upward shift was applied for clarity in viewing the resolved fine structure transitions, if any are present. The green line at 3500 MHz represents 1% of the high- L signal size in the 10x magnified data. The blue lines super imposed on the graph represent the calculated positions of the dominant (55, L) – (109, $L+1$) transitions assuming $\alpha_l = 5.05$ a.u.

The lack of resolved fine structure transitions presents a series of puzzles. The dipole polarizability computed by U. I. Safronova, *et al.* for Th^{4+} was in close agreement with the experimentally measured value. Using the same method, U. I. Safronova, *et al.* computed a dipole polarizability of 5.05 a.u. for U^{6+} [34]. Using that value estimates for the energies for the dominant $\Delta L = +1$ transition between different Rydberg states in the transitions studied were computed. These energies are graphically depicted in Figs. 5.1, 5.2, and 5.3 by the blue bars.

Any resolved U^{5+} fine structure transitions present in Fig. 5.1 are not clear outside of the noise levels. If there are transitions present they might be present at the 0.2% of the high- L level. Figures 5.2 and 5.3 potentially show hints of signals at locations predicted for the $(53, 10) - (93, 11)$ and $(55, 10) - (109, 11)$ transitions respectively; however the signals are not significantly outside the background levels. When the blue bars are removed, it is difficult to identify any bumps as true signals; only with the visual aid of the predicted locations do the “signals” seem to be present.

In all three figures there are hints of something resembling a transition at the predicted location for the $L = 11$ transition very close to the high- L transition, suggesting that the theoretically calculated value of 5.05 a.u. [34] is not very far from the actual value. However, there do not appear to be signs of a consistent pattern of resolved transitions further away from the high- L transition. Without a consistent pattern of transitions it is impossible to determine the dipole polarizability of the U^{6+} ion from the observation of the U^{5+} Rydberg fine structure.

5.2 Comparison of different beam configurations

As a result of the lack of clearly resolved signals in U^{5+} , even with the time invested, to integrate individual runs and obtain high signal to noise, effort was applied towards comparing various characteristics of the U^{6+} beams to the Th^{4+} beam. The key parameters of note in analyzing the differences between the two beams are the beam velocity, target final nF state, and the initial n state of the Rydberg transition to be studied. Understanding the characteristics of how these three experimentally controllable parameters affect the background rates and signal rates is key to developing an understanding of the difficulty of the U^{5+} observations compared to the Th^{3+} observations and providing guidance for a more successful U^{6+} experiment.

Table 5.2 lists some of the important parameters that can be compared between the three different U^{6+} beam configurations and the Th^{4+} configuration studied, the first column in Table 5.2 lists identifications given to the configurations for reference throughout the remainder of this chapter, U-A, U-B, U-C, and Th-A. In addition to the ion beam, RESIS transition and Rydberg target n , the table gives the amplitude of the high- L signal, the amplitude of the observed RESIS transition with $L = 11$, the experimentally measured noise in 20 seconds (denoted $\sigma(20s)$) and the CEM DC level. All are converted to a CEM potential of -1100. The value reported for the shot noise estimated from the CEM DC level, σ_{DC} , at a CEM potential of -1100 V with a collection time of 20 seconds is given by:

$$\sigma_{DC}(20 s) = \sqrt{CEMDC(V) \cdot 1.602 \times 10^{-8}}, \quad (5.1)$$

as discussed in Chapter 3. Also listed in Table 5.2 is the charge exchange beam current from the Rydberg target, CXRT, and the average primary beam intensity. These two

measurements were made using the faraday cup at the end of the beam line. The CXRT is the increase in the charge exchange beam current that occurs when the Rydberg target is turned on compared to when it is turned off. The primary beam is the beam in the various configurations that does not capture a highly excited electron from the Rydberg target. The value reported in column 6 of Table 5.2 gives the ratio of the $(n, 11) - (n', 12)$ peak to the high- L peak for the different beam configurations. The ratios reported in column 6 of Table 5.2 for the U-A,B, and C configurations are, at best, upper limits on a supposed $L = 11$ signal; whereas the ratio listed for the Th-A configuration is an actual number since the signal was clearly observed.

Table 5.2: Measured characteristics of the different U^{5+} and Th^{4+} transitions studied. The 1st column provides an abbreviated identification for each configuration studied. The 2nd lists the transition and ion, the 3rd column gives the beam energy and the 4th column lists the final nF state of the target used during the observation of the transition. The 5th column lists the high- L signal amplitude in mV, the 6th column is the ratio of amplitudes of the bump near the calculated location of $L = 11$ to the high- L , the 7th column reports the error in the measurement taken from the scatter of the Y-channel signals from a straight line and the 8th column lists the CEM DC recorded off of the high- L signal. The 9th column reports the error in the measurement estimated from Eq. (5.1). The 10th and 11th columns list the amount of charge transfer beam from the Rydberg target and the average primary beam measured on the Faraday cup at the end of the beam line. The values reported in the columns labeled: high- L signal, CEM DC, σ , and σ_{JK} are all taken to be when the CEM has a voltage of -1100 V applied.

Configuration	Transition	Beam energy (keV)	Rydberg Target (nF)	$S(HL)$ (mV)	$S(L=11)/S(HL)$	$\sigma(20s)$ (mV)	CEM DC (mV)	σ_{DC} (mV)	CXRT (nA)	Average Primary (nA)
U-A	U VI 53 – 93	150	10F	14.30(1)	$\leq 0.002(1)$	0.040	46.0	0.027	0.37	29
U-B	U VI 53 – 93	150	8F	0.46(3)	$\leq 0.029(8)$	0.007	2.2	0.006	0.06	4
U-C	U VI 55 – 109	93	10F	1.30(1)	$\leq 0.007(2)$	0.011	7.1	0.011	0.18	5
Th-A	Th IV 37 – 73	100	10F	12.35(13)	0.037(4)	0.031	14.21	0.015	0.25	16

A measure worth investigating for the different transitions presented in Table 5.2 is the maximum signal to noise ratio of the resolved $L = 11$ signal estimated from Eq. (5.1). This corresponds to the signal to noise of the first resolved or nearly resolved signal, which should be the largest and easiest to see. The analysis is slightly complicated by the fact that the size of the primary ion beam generated by the ECR varied widely during the course of these studies, as can be seen from the last column in Table 5.3. This can be corrected since both the high- L signal and CEM DC are roughly proportional to the size of the primary beam current. Thus the high- L signal to the noise estimated from Eq. (5.1) is proportional to the square-root of the primary beam current. This ratio can then be corrected to a constant beam current for direct comparison of all the different studies by:

$$\left[\frac{S(HL)}{\sigma_{DC}} \right]_{P=10\text{nA}} = \left(\frac{S(HL)}{\sigma_{DC}} \right) \cdot \sqrt{\frac{10 \text{ nA}}{P}}. \quad (5.2)$$

A standard primary beam current was taken to be 10 nA for comparison and P is the primary beam current listed in Table 5.2. The uncorrected and corrected ratios of $S(HL)$ to σ_{DC} are given in column four and five of Table 5.3. Using the ratio of $S(L = 11)/S(HL)$ listed in Table 5.2, the ratio of $S(L = 11)/\sigma_{DC}$ can be computed and is listed in the last column of Table 5.3 for the different beams studied. From this comparison it becomes clear that the Th-A configuration has the largest signal to noise over any of the U configurations studied by an order of magnitude.

Table 5.3: Predictions of the n_l , $L = 11$ signal to noise by Eq. (5.1), correcting for a constant beam current of 10 nA and assuming a 20s collection time.

Configuration	$S(HL)/\sigma_{DC}$	Corrected $S(HL)/\sigma_{DC}$	$S(L=11)/\sigma_{DC}$
U-A	530(1)	311(1)	$\leq 0.6(3)$
U-B	77(5)	130(8)	$\leq 3.8(1.1)$
U-C	118(1)	176(2)	$\leq 1.2(3)$
Th-A	823(9)	661(7)	25(3)

The natural question that follows from the last column of Table 5.3 is: how long would it take to achieve signal to noise on the semi-resolved $L = 11$ peak in the U^{6+} studies as was achieved in the Th^{4+} study in 20 seconds of data acquisition per point? The time required per point, provided the primary beam current is at a constant 10 nA, is listed in the last column of Table 5.4. The minimum time of only 14.3 minutes per point is for U-B configuration. Of course, in practice the time may be much longer if the primary ion beam is weaker than 10 nA or the $L = 11$ signal is smaller than the upper limit given in Table 5.2. In any case it appears that the U^{6+} study is much more difficult than the Th^{4+} study based on the observed signal to noise ratios. The experiments all show that of the three U configurations studied, configuration U-A was the most difficult. Configuration U-B is favored for future studies.

Table 5.4: Estimation of the time required, per point, to achieve similar signal to noise on the $n_l, L = 11$ signal that was achieved in the study of Th IV.

Configuration	Required Time multiplier	Time Required per point
U-A	1736×	9.6 hr
U-B	43×	14.3 min
U-C	434×	2.4 hr
Th-A	1×	20 s

5.3 Comparison of observations with CTMC predictions

In order to explore the reasons for the observed differences between the three Uranium configurations and the Th-A configuration, Classical Trajectory Monte Carlo (CTMC) methods are used to model the population of Rydberg states after charge exchange from the Rydberg target. CTMC is a classical three-body approach to modeling the charge exchange process that occurs between the Rydberg target and a positively charged ion. The highly excited electron is singled out from the target atom

and projectile ion. The projectile and target atom are treated as point particles and hydrogenic wavefunctions are assumed for the electron [26]. Classical orbits are associated with the electron based on the initial conditions and the phase and orientation of these orbits are chosen randomly for each trajectory [26]. The classical Hamiltonian equations of motion are then solved numerically as the projectile ion approaches the target atom at various impact parameters and if capture occurs the energy and angular momentum of the final electron orbit are related to the quantum numbers n and L [26]. The CTMC approach is well suited for modeling collisions between ions, e.g. the U^{6+} and Th^{4+} ions studied, and excited atoms, e.g. the highly excited Rb atoms in the Rydberg target, because the interaction between the particles is strong and long range and the classical treatment of the Coulomb scattering agrees with the exact quantum mechanical approach [26]. Many of the predictions made by CTMC have been tested against experiment [15,41]

Comparisons between the different configurations studied and CTMC predictions can be made more directly if the signal and beam current intensities are converted to ion count rates. Since the signals are measured with a lock-in amplifier the voltages recorded are RMS voltages, not peak to peak. The peak voltage is related to the RMS voltage reported by the lock-in amplifier by:

$$V_{PP} = \frac{\pi}{\sqrt{2}} V_{RMS} \cdot \quad (5.3)$$

The signals recorded by the lock-in amplifier can be converted to a count rate of ions per second by:

$$R_{Signal} = \frac{S(V) \cdot \frac{\pi}{\sqrt{2}}}{g \cdot e \cdot 10^8 \Omega} = S(mV) \cdot 27733 \frac{(ions/s)}{mV}, \quad (5.4)$$

where S is the recorded signal size in volts, $g = 5000$ with the CEM at -1100 V, e is the charge of the electron in Coulombs, and 10^8 Ohms is the resistance of the electrometer used. Similarly, the charge transfer beam currents measured using the end Faraday cup can also be converted to a count rate relatively simply by:

$$R_{CXRT} = \frac{CXRT(A)}{(Q-1) \cdot e} = CXRT(nA) \cdot \frac{6.2422 \times 10^9 \text{ (ions/s)}}{(Q-1) \text{ nA}}, \quad (5.5)$$

where $CXRT$ is the measured charge transfer beam current on the end Faraday cup and Q is the charge of the primary ion beam.

The $L = 11$ signal ion count rate can then be computed by:

$$R_{S(L=11)} = R_{S(HL)} \cdot \left(\frac{"L = 11"}{High - L} \right), \quad (5.6)$$

where $R_{S(L=11)}$ is the signal rate for the high- L signal given by Eq. (5.4) and the quantity in the parenthesis in Eq. (5.6) is the ratio of the $L = 11$ peak amplitude to the high- L peak amplitude listed in Table 5.2. Table 5.7 lists the ion count rates for the measured primary, R_P , the charge transfer beam, R_{CXRT} , the CEM DC, R_{BG} , the high- L signal, $R_{S(HL)}$, and the $L = 11$ signal, $R_{S(L=11)}$ and Table 5.8 lists the ratios of the count rates listed in Table 5.7.

Table 5.7: Measured count rates for the charge transfer beam and n_I , $L = 11$ signal.

Configuration	R_P	R_{CXRT}	R_{BG}	$R_{S(HL)}$	$R_{S(L=11)}$
U-A	3.6×10^{10}	4.6×10^8	5.7×10^5	4.0×10^5	$\leq 800(400)$
U-B	7.5×10^7	0.75×10^8	2.7×10^4	1.3×10^4	$\leq 370(100)$
U-C	5.2×10^9	2.3×10^8	8.9×10^4	3.6×10^4	$\leq 250(70)$
Th-A	2.5×10^{10}	5.2×10^8	1.8×10^5	3.4×10^5	12,600(1400)

Table 5.8: Ratios of the observed count rates.

Configuration	R_{BG}/R_{CXRT}	$R_{S(HL)}/R_{CXRT}$	$R_{S(L=11)}/R_{CXRT}$	$R_{S(L=11)}/R_{S(HL)}$
U-A	1.2×10^{-3}	8.7×10^{-4}	$\leq 2(1)$ ppm	$\leq 0.23(5)\%$
U-B	3.6×10^{-4}	1.7×10^{-4}	$\leq 5(1)$ ppm	$\leq 2.8(8)\%$
U-C	3.9×10^{-4}	1.6×10^{-4}	$\leq 1.1(3)$ ppm	$\leq 0.69(19)\%$
Th-A	3.5×10^{-4}	6.5×10^{-4}	24(3) ppm	3.7(4) %

5.4 CTMC predictions of Signal size compared to observations

The distribution of the population final state n 's after charge exchange from the Rydberg target varies based on the projectile's mass, charge, and velocity. Figure 5.4(a) – Fig. 5.4(d) show the different capture distributions into a final state with principle quantum number n_p for the four different beam configurations. Also shown in Fig. 5.4(a) – (d) is a dashed line indicating the lower n of the transition studied, n_l .

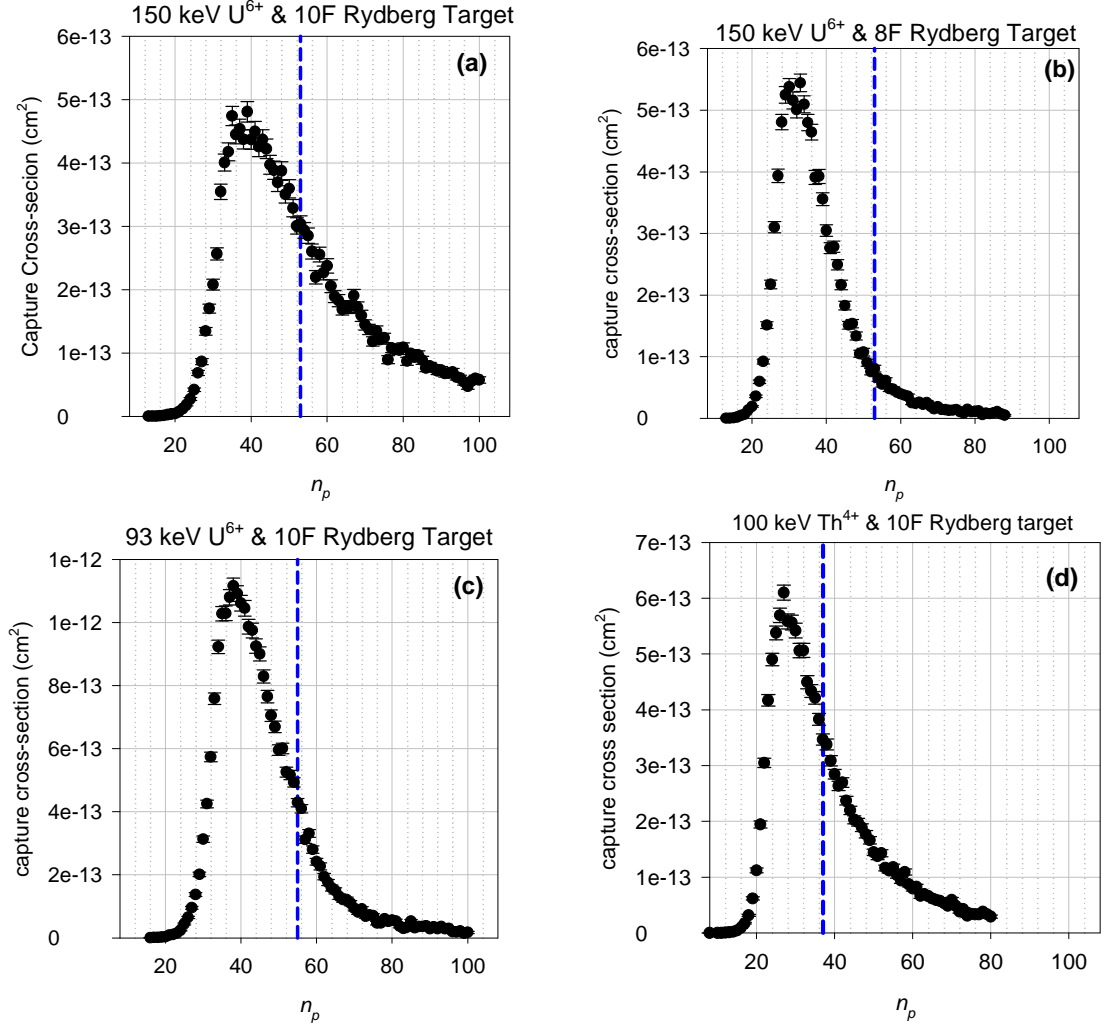


Figure 5.4: CTMC predicted n_l distributions for the (a) U-A, (b) U-B, (c) U-C, and (d) Th-A configurations. The blue dashed line in each of the figures corresponds with n_l of the transitions studied.

The distributions in n_p can be used to compare predictions made by CTMC with the observations for the four different configurations. Important characteristics of the CTMC predictions are the total capture cross section for all n_p 's, and the capture cross section into n_l , these values determined from an average of 10 different runs of the CTMC codes are shown in Table 5.9. The fractional capture into n_l , f_n , corresponds to the high-L signal per charge exchange from the Rydberg target. The value of f_n is determined from the CTMC predicted distributions shown in Fig. 5.4 and is listed in column 4 of Table

5.9. Comparison between f_n in Table 5.9 and $R_{S(HL)}/R_{CXRT}$, reproduced in the last column of Table 5.9 from Table 5.8 for reference, can be made. On average the predicted high- L signal per charge exchange is 50 times greater than the observed high- L signal per charge exchange. This suggests that the simple idea that the entire population contributes to the high- L signal is too simplistic. Taking the model a step further requires modeling the high- L signal and weighting the contribution to the signal from each L by

$\langle n, L | Z | n', L' \rangle^2$. Modeling the high- L signal in this fashion suggests that f_n should be reduced by 2 for the U-A, U-B, U-C, and Th-A configurations. Also, at best only 50% of the population would be excited into the detection state, so another factor of 2 can be taken out of f_n . The f_n adjusted by a factor of 4 to account for the excitation probability and efficiency, f'_n , is listed in column 5 of Table 5.9. The ratio of observed high- L signals to CXRT are smaller than f'_n by factors between 4 and 20. This suggests that the high- L signal amplitude is affected significantly by other factors.

Table 5.9: CTMC predicted capture cross sections for the different beam configurations studied.

Configuration	Total Capture cross-section (cm ²)	Average capture cross-section into n_I (cm ²)	f_n (%)	f'_n (%)	$R_{S(HL)}/R_{CXRT}$ (%)
U-A	$1.829(4) \times 10^{-11}$	$2.96(4) \times 10^{-13}$	1.62(2)	0.41(1)	0.087
U-B	$1.055(2) \times 10^{-11}$	$0.694(11) \times 10^{-13}$	0.66(1)	0.17(1)	0.017
U-C	$2.595(3) \times 10^{-11}$	$4.35(6) \times 10^{-13}$	1.68(2)	0.42(1)	0.016
Th-A	$1.425(2) \times 10^{-11}$	$3.56(5) \times 10^{-13}$	2.50(4)	0.63(1)	0.065

Another way to compare the predictions made by CTMC to the observations in Table 5.8 is to compare the ratio $R_{S(L=11)}/R_{CXRT}$ to the ratio of the average capture cross-section into n_I , $L = 9, 10$, and 11, correcting for radiative decay, to the total capture cross section. One half of this ratio represents the maximum predicted signal per charge transfer from

the Rydberg target. The average capture cross section into n_l , $L = 9, 10$, and 11 is obtained from CTMC and is listed in the 2nd column of Table 5.10. The decay factor listed in the 3rd column of Table 5.10 is given by

$$Decay = e^{-A(Q,n,L)T} \quad (5.5)$$

where $A(Q,n,L)$ is the decay rate of a Rydberg state with a given Q , n , and $L = 11$ and is estimated from the formula given by E. S. Chang [30]. The value of T is the time required to transit the 83.4 cm between the target and the LIR given the different beam velocities in the four configurations. The quantity in the 4th column of Table 5.10 represents the fraction of the capture cross section into the n_l , $L = 9, 10$, or 11 state out of the entire capture cross-section. The quantity listed in the 5th column in Table 5.10 corresponds to the maximum predicted signal to charge transfer and is half the product of the quantities listed in the 3rd and 4th columns.

Table 5.10: CTMC predicted capture into n_l , $L = 9, 10$, or 11 , corrected for radiative decay.

Configuration	Average capture cross-section into $n_l, L = 9, 10$, and 11 (cm ²)	Decay	$f_{L=9,10,11}$	Predicted $R_{S(L=11)}/R_{CXRT}$
U-A	$0.13(2) \times 10^{-15}$	0.182	$7.1(11) \times 10^{-6}$	0.65(10) ppm
U-B	$0.74(9) \times 10^{-15}$	0.182	$7.0(9) \times 10^{-5}$	6.4(8) ppm
U-C	$1.48(15) \times 10^{-15}$	0.145	$5.7(6) \times 10^{-5}$	4.1(4) ppm
Th-A	$2.1(2) \times 10^{-15}$	0.303	$1.47(10) \times 10^{-4}$	22.3(15) ppm

The comparisons for the different configurations are summarized in Table 5.11. The conclusions supported by the values listed in Table 5.11 are:

- 1) The Th⁴⁺ signals are about as large as could be expected if the entire Th⁴⁺ beam consists of ground state ions. This is consistent with the conclusion in Chapter 3 that the metastable fraction in Th⁴⁺ is small.

- 2) It is impossible to say how large the resolved signals in U^{6+} are, since there are no definitive observations to date. Configuration U-C in Table 5.11 suggests that the resolved signals are a smaller fraction of the predictions in U^{6+} than in Th^{4+} , perhaps by a factor of 4. This is consistent with the conclusion in Chapter 3 that the U^{6+} beam contains a large metastable fraction and suggests that the metastable fraction could be $\sim 75\%$.

Table 5.11: Comparison of the observed ratio of $R_{S(L=11)}$ to R_{CXRT} to the same ratio predicted by CTMC.

Configuration	Observed $R_{S(L=11)}/R_{CXRT}$	Predicted $R_{S(L=11)}/R_{CXRT}$	Ratio of Observed to Predicted
U-A	$\leq 2(1)$ ppm	0.65(10) ppm	$\leq 3(2)$
U-B	$\leq 5(1)$ ppm	6.4(8) ppm	$\leq 0.78(18)$
U-C	$\leq 1.1(3)$ ppm	4.1(4) ppm	$\leq 0.24(8)$
Th-A	24(3) ppm	22.3(15) ppm	1.08(15)

Aside from the issue of metastable contamination, the predictions for $R_{S(L=11)}/R_{CXRT}$, listed in Table 5.11, vary over a wide range and are consistently worse for the Uranium configurations than the Th-A configuration. Most notably the U-A configuration predicts that the population that could contribute to the resolved RESIS excitation signals is ten times worse than the U-B configuration. This is in spite of the fact that the fractional capture into n_l is much larger in the U-A configuration than the U-B configuration, as illustrated in Fig. 5.4 and Table 5.9. The difference between the two configurations is a result of the different L population distributions created by the different Rydberg targets. The differences in the population distributions in L were explored in experimental studies of the L distributions resulting from charge capture by Si^{3+} . Experimental studies showed that CTMC predictions of capture distribution in L will be either “high- L rich” or “high- L poor”, where high- L refers to the population in L states that contribute to the high- L

signal, depending upon the target state for a given beam of ions with charge Q and velocity [41] and the choice of n_l to be studied. It was demonstrated in the same study that the size of the resolved RESIS excitation signals can differ by a factor of two or greater [41], depending upon the choice of target final state. The exact reasons for the varying distribution of population in L for different target states remains unexplained by any simple model [41]. However, the CTMC predictions of the signal sizes in Table 5.11 show that even without the issue of metastable ions all the Uranium configurations studied to date would be much more difficult than the Th-A configuration.

5.5 Future directions

The inability to clearly observe any transitions between high- L Rydberg states in U^{5+} in a practical amount of time, despite the clear success in Kr^{5+} is disappointing. The large background and relatively nonexistent signal size in the U^{5+} can be reasonably attributed to a significant fraction of the primary U^{6+} beam being in metastable states, as was discussed in Chapter 3. If it is really true that a large portion of the U^{6+} beam is in metastable states, then a determination of the dipole polarizability of U^{6+} using the RESIS technique may be impossible.

On the other hand, the optical RESIS studies of Th^{3+} were very successful and there are good reasons to hope for future improvements. To enhance the Th^{3+} excitation signals the 15° charge selection magnet after the Rydberg target could be removed. This would result in the RESIS beam line being shortened by approximately 12". With a 100 keV Th^{4+} beam this equates to a reduction in the transit time between the target and the LIR by 1.06 μs . Assuming that the amplitude of the resolved signals decay exponentially

in time, then a gain of approximately 2 in the resolved $(37, 10) - (73, 11)$ transition would be expected. As shown in Fig. 5.4(d) the Th^{3+} observations were not carried out at the peak of the n distribution resulting from charge exchange from the Rydberg target. This was done because there is a deficiency in the population of L 's that are potentially resolvable with the optical RESIS technique at the peak of the n distribution. More effective scrambling of the L population distribution could be achieved with microwave mixing as suggested by Ref. [42]. By scrambling the L population more effectively it might be possible to conduct the experiment at the peak of the n distribution leading to dramatic increases in the signal to noise. Also, if it is true that the dominant source of background in the Th^{3+} observations is not due to auto-ionizing Rydberg states then future studies of the background could determine the source. Once the dominant source of the background is known then it might be possible to eliminate, or significantly reduce, the background completely from the Th^{3+} excitation spectra. If all these improvements work favorably for the Th^{4+} experiment, it might become possible to successfully observe the U^{5+} fine structure.

Even without these enhancements there is good reason to believe that it is possible to conduct a study of the transitions between different L states using the microwave RESIS technique. The microwave technique is attractive because the observations are not affected by uncertainties in the calibration of θ_{\perp} and velocity. Also, it has been shown in previous studies that the microwave RESIS is capable of an order of magnitude or more increased precision in the determination of the dipole polarizability compared with the optical RESIS technique.

References

- [1] U.S.Department of Energy Basic Energy Sciences. (2009). *Chemical Sciences Research Programs*. [Online]. Available: <http://www.sc.doe.gov/production/bes/chm/Programs/programs.html> [2010, June].
- [2] *The Chemistry of the Actinide and Transactinide Elements*, edited by L. R. Morss, N. M. Edlestein, and J. Fuger (Springer Netherlands, Dordrecht, Netherlands, 2006).
- [3] J. Blaise and J.-F. Wyart. (2009). *Energy Levels and Atomic Spectra of Actinides*. [Online]. Available: <http://www.lac.u-psud.fr/Database/Contents.html> [2010, June].
- [4] Los Alamos National Laboratory Chemistry Division. (12-15-2003). *Thorium Atomic data*. [Online]. Available: <http://periodic.lanl.gov/elements/90.html> [2010, Oct.].
- [5] Los Alamos National Laboratory Chemistry Division. (1-5-2004). *Uranium Atomic data*. [Online]. Available: <http://periodic.lanl.gov/elements/92.html> [2010, Oct.].
- [6] B. Edlén, *Handbuch der Physik XXVII*, edited by S. Flügge (Springer-Verlag, Berlin, 1964), p. 80.
- [7] R. J. Drachman, *Phys. Rev. A* **26**, 1228 (1982).
- [8] S. R. Lundeen and C. W. Fehrenbach, *Phys. Rev. A* **75**, 032523 (2007).
- [9] A. R. Edmonds, *Angular Momentum in Quantum Mechanics*, (Princeton University Press, Princeton, New Jersey, 1974).
- [10] D. R. Beck (private communication).
- [11] E. L. Snow, Ph.D. thesis, Colorado State University, 2006.
- [12] K. Bockasten, *Phys. Rev. A* **9**, 1087 (1974).
- [13] G. W. F. Drake and R. A. Swainson, *Phys. Rev. A* **44**, 5448 (1991).

- [14] R. A. Komara, M. A. Gearba, C. W. Fehrenbach, and S. R. Lundeen, *J. Phys. B: At. Mol. Opt. Phys.* **38**, S87-S95 (2005).
- [15] D. S. Fisher, Ph.D. thesis, Colorado State University, 2000.
- [16] S. L. Palfrey, Ph.D. thesis, Harvard University, 1983.
- [17] F. J. Deck, Ph.D. thesis, University of Notre Dame, 1993.
- [18] J. S. Coursey, D. J. Schwab, J. J. Tsai, and R. A. Dragoset. (2010). *Atomic Weights and Isotopic Compositions (version 3.0)*. [Online]. Available: http://physics.nist.gov/cgi-bin/Compositions/stand_alone.pl?ele=Th [2010, Sept.].
- [19] M. E. Hanni, J. A. Keele, S. R. Lundeen, and W. G. Sturru, *Phys. Rev. A* **78**, 062510 (2008).
- [20] J. A. Keele, S. L. Woods, M. E. Hanni, and S. R. Lundeen, *Phys. Rev. A* **81**, 022506 (2010).
- [21] J. A. Keele (private communication).
- [22] R. Pardo, *Nucl. Instrum. & Methods in Physics Research* **B40/41**, 1014 (1989).
- [23] M. E. Hanni *et al.*, *Phys. Rev. A* **81**, 042512 (2010).
- [24] C. W. Fehrenbach, S. R. Lundeen, and O. L. Weaver, *Phys. Rev. A* **51**, R910 (1995).
- [25] M.-T. Huang *et al.*, *J. Phys. B: At. Mol. Opt. Phys.* **30**, 2425 (1997).
- [26] A. P. Hickman, R. E. Olson, and J. Pascale, in *Rydberg states of atoms and molecules*, Edited by R. F. Stebbings and F. B. Dunning (Cambridge University Press, New York, 1983), Chap. 6, p. 187.
- [27] C. R. Quick and H. C. Bryant, *J. Opt. Soc. Am. B* **7**, 708 (1990).
- [28] H. A. Bethe and E. E. Salpeter, *Quantum Mechanics of One- and Two-Electron Atoms*, (Dover Publications, Inc., Mineola, New York, 2008).
- [29] R. D. Cowan, *The Theory of Atomic Structure and Spectra*, (University of California Press, Berkeley, California, 1981).
- [30] E. S. Chang, *Phys. Rev. A* **31**, 495 (1985).
- [31] J. J. Sakurai, *Modern Quantum Mechanics*, edited by S. F. Tuan (Addison-Wesley Publishing Company, Inc., Menlo Park, CA, 1994).

[32] CO₂ laser frequencies used in this work.

CO ₂ Line	CO ₂ Frequency (cm ⁻¹)
10P(30)	934.8945
10P(14)	949.4793
10P(10)	952.8809
10R(16)	973.2885
10R(24)	978.4723

[33] P. F. A. Klinkenberg, *Physica C* **151**, 552 (1988).

[34] U. I. Safronova, W. R. Johnson, and M. S. Safronova, *Phys. Rev. A* **76**, 042504 (2007).

[35] M. S. Safronova (private communication).

[36] S. Fraga, J. Karwowski, and K. M. S. Saxena, *Handbook of Atomic Data*, (Elsevier Scientific Pub., Amsterdam, 1976).

[37] A. Derevianko (private communication).

[38] A. Borschevsky and P. Schwerdtfeger (private communication).

[39] E. L. Snow and S. R. Lundeen, *Phys. Rev. A* **75**, 062512 (2007).

[40] E. L. Snow and S. R. Lundeen, *Phys. Rev. A* **76**, 052505 (2007).

[41] S. R. Lundeen, R. A. Komara, C. W. Fehrenbach, and B. D. DePaola, *Phys. Rev. A* **64**, 052714 (2001).

[42] P. Pillet *et al.*, *Phys. Rev. A* **30**, 280 (1984).